Title

Magnetic behavior of multi-principal element alloys and ultrafast domain dynamics in CoFe/Ni ferromagnetic multilayers

Author

Jangid, Rahul

Publication Date

2023

Peer reviewed|Thesis/dissertation

Magnetic Behavior of Multi-principal Element Alloys and Ultrafast Domain Dynamics in CoFe/Ni Ferromagnetic Multilayers

By

RAHUL JANGID
DISSERTATION

Submitted in partial satisfaction of the requirements for the degree of

DOCTOR OF PHILOSOPHY

in

Materials Science and Engineering

in the

OFFICE OF GRADUATE STUDIES

of the

UNIVERSITY OF CALIFORNIA

DAVIS

Approved:

Roopali Kukreja, Chair

Sabyasachi Sen

Jeffery C. Gibeling

Committee in Charge

2023

To my mother, Ratni Devi,
and father, Sheshnarayan Jangid,
who believed in me when no one did.

Abstract

Permanent magnets composed primarily of rare earth elements are critical components in electric vehicle motors. With the recent surge in electric vehicle sales, demand for rare earth elements has dramatically increased, elevating costs. Thus, there is strong interest in identifying rare-earth-free alternatives for permanent magnet applications. The multi-principal element alloy (MPEA) family has emerged as a promising candidate. MPEAs contain three or more principal constituent elements, some of which may be magnetic such as Fe, Co, Cr, Mn, and Ni. In this thesis, I will first discuss our investigation of the magnetic properties of FeCoCrMnSi-based MPEAs. Multiple magnetic phase transitions were observed via zero-field-cooled/field-cooled magnetization measurements, indicating a rich magnetic phase diagram. Spectroscopic measurements revealed ferromagnetic ordering of Fe, Co and Cr, while Mn exhibited no long-range magnetization. Our results illustrate the rich and complex magnetic properties of MPEAs.

In addition to permanent magnet applications, controlling mesoscopic magnetic textures may enable next-generation energy-efficient magnetic memory and data storage. The second portion of my talk will focus on ultrafast manipulation of magnetic textures. Domain wall motion in ferromagnets driven by magnetic fields, electrical currents, or spin waves is typically quite slow, below 100 m/s. Furthermore, the Walker breakdown phenomenon limits domain wall velocities at higher driving fields or currents as precession of spins approaches the ferromagnetic resonance frequency. However, far-from-equilibrium dynamics induced through ultrafast optical excitation may allow overcoming these limitations and accessing nonequilibrium material behavior. In fact, recent theoretical work predicted superdiffusive spin current-driven domain wall velocities up to 14 km/s in optically pumped ferromagnets. We experimentally tested this prediction in a magnetically textured CoFe/Ni multilayer film using time-resolved extreme ultraviolet magnetic scattering with 50 fs resolution. For the highest optical pump fluences, we observed domain wall velocities up to 66 km/s, approaching the theoretical limit set by magnon group velocity. These findings demonstrate that far-from-equilibrium optical excitation can dramatically accelerate mesoscale magnetic textures. Our studies open the possibility of manipulating the ground state to achieve far-from-equilibrium effects at mesoscopic length scales. The implications of such nonequilibrium spin kinetics likely extend to understanding and harnessing ultrafast phenomena in quantum materials.

Acknowledgments

Hailing from a rural part of India, I could never have imagined having the opportunity to pursue my dream of becoming a researcher. My heart overflows with gratitude for all those who have supported me on this remarkable journey. Foremost, I am deeply indebted to my family members whose unwavering encouragement and sacrifice have been the bedrock of my pursuit. My brother, Dinesh Kumar Jangid, deserves a special mention for his immense sacrifices in providing financial support for our family while I chased my dreams. He shielded me from the challenges within our family and remains an enduring source of inspiration in my life. Words cannot express the depth of my gratitude for everything he has done for me.

Although India is developing at a rapid pace, it has been concentrated primarily in urban areas, further exacerbating the inequality between rural and urban regions. I consider myself fortunate to have had parents who could afford to send me to urban centers in search of better education. Though my journey in the city was marked by countless stumbles and failures, I owe my gratitude to exceptional teachers like Dr. Om Prakash Mahela, whose support helped me regain my footing and secure a place at the prestigious Indian Institute of Technology, Roorkee (IITR).

I extend my heartfelt thanks to Prof. B.V. Manoj Kumar and Prof. G.P. Chaudhary for nurturing my interest in research at IITR and providing opportunities at the University of Seoul, South Korea. Prof. Deepankar Banerjee from the Indian Institute of Science (IISc) played a pivotal role in persuading me to pursue graduate school in United States. Special appreciation goes to Prof. Jeremy Mason for his outstanding course on materials simulations, which significantly contributed to my work on ultrafast domain dynamics. Prof. Mason's dedication to excellence in teaching is extremely inspiring and I hope one day I would be able to explain complex topics in as simple yet detailed fashion as him. I am grateful to Prof. Sabyasachi Sen and Prof. Jeffery C. Gibeling for their invaluable guidance as members of my thesis committee. Both Prof. Sen and Prof. Gibeling stood by and supported me as year after year I brought something from the left field to our yearly discussions.

I express my profound gratitude to my collaborators from domain dynamics project, Dr. Thomas J. Silva, Prof. Ezio Iacocca, Prof. Eric E. Fullerton, Prof. Stefano Bonetti, Dr. Nanna Zhou Hagström, Kyle Rockwell, Dr. Justin M. Shaw, Dr. Jeffrey A. Brock, Dr. Hans T. Nembach and Dr. Mark W. Keller for their consistent support and enlightening biweekly and monthly meetings that kept me motivated and enriched my understanding of ultrafast science. My appreciation also goes to the staff members Dr. Matteo Pancaldi Dr. Dario De Angelis, Dr. Flavio Capotondi and Dr. Emanuele Pedersoli at FERMI Free Electron Laser in Trieste, Italy, for allowing us to utilize the Diffraction and Projection Imaging (DiProI) beamline and for their continuous support. I am thankful to Dr. Alpha T. N'Diaye, Dr. Padraic Shafer, and Dr. Christoph Klewe for their assistance with spectroscopy measurements at the Advanced Light Source. I would like to also thank Willie Beeson for helping me with AC susceptibility measurements and for his helpful discussions about MPEAs.

I express my deepest gratitude to all my colleagues in the lab, including Kenneth, Jugal,

Scott, Pooja, Nushrat, Emma, Spencer, Yu-Hsing, Ian, Don, Nadia, Joyce, Josh, Louie, Dr. Jianheng, Li, Dr. Kristoffer Haldrup, Dr. Saeed Yousefi Sarraf and many others, for their valuable insights into various aspects of research and personal life. I can't deny the fact that I loved distracting everyone with discussions about the most random topics in the lab. I hope the Kukreja Lab coffee tower grows at an ever exceeding pace thanks to Pooja, Emma and Jugal. I would also like to thank my sister, Pallavi D. Sambre, and her fiancé, Rishab Panyam, for all the parties and fun trips all to countless places around US.

I extend my heartfelt gratitude to my dedicated and inspiring Principal Investigator, Prof. Roopali Kukreja. Her unwavering support, expert guidance, and exceptional mentorship have been instrumental throughout my doctoral journey. Her deep knowledge of various fields, tireless commitment to research excellence, and boundless patience have profoundly shaped my academic growth. Her willingness to engage in rigorous discussions, and keen insights into experimental design and data analysis have been invaluable source of learning for me. I am deeply appreciative of the opportunities she provided for collaboration, her encouragement during challenging times, and her belief in my potential. She has taught me how to drive a scientific inquiry, thinking critically and looking at the broader picture of a project. I owe a significant portion of my academic accomplishments to her excellent mentorship and leadership. I am truly fortunate to have had Roopali as my mentor, and I will carry the lessons learned during this journey with me into the next phase of my career.

Finally, I would like to express my deepest gratitude to someone who has been my unwavering source of support, encouragement, and love throughout this challenging journey - my girlfriend Meera. Your presence in my life during my Ph.D. has been a beacon of strength and inspiration. You stood by me during the long nights in lab, patiently listened to my ideas and frustrations, and celebrated even the smallest victories with unwavering enthusiasm. Your sacrifices, understanding, and the countless great meals you cooked for us while I was hunched over my laptop will forever be etched in my heart. Your calming presence during stressful times provided me with the clarity and focus I needed to make progress. This dissertation represents not only my academic journey but also our shared journey of growth, love, and support. I am profoundly grateful for your presence in my life and for being my center of gravity during this challenging endeavor. As I move forward into the next chapter of my life, I do so with you by my side, and I look forward to the many more adventures and accomplishments we will share together. You are the cutest passenger princess ever and I hope to go on countless more road trips (maybe more hikes too!) with you. Thank you, from the depths of my heart, for being the most incredible partner and for making this journey not only possible but also deeply meaningful.

Contents

List of Figures

List of Tables

List of code snippets

Acronyms

AI	Artificial Intelligence
BEV	Battery electric vehicle
DMI	Dzyaloshinskii–Moriya interaction
DRAM	Dynamic random-access memory
EDS	Energy Dispersive Spectroscopy
EMF	Electromotive Force
EUV	Extreme Ultraviolet
EV	Electric vehicle
EXAFS	extended X-ray absorption fine structure
f.c.c	face-centered cubic
FC	Field Cooling
FFT	Fast Fourier Transform
GMR	Giant Magnetoresistance
GPU	Graphics processing unit
h.c.p	hexagonal close-packed
HAADF	High-Angle Annular Dark-Field
HEA	High entropy alloy
HHG	High Harmonic Generation
LINAC	linear accelerator
MFM	Magnetic Force Microscopy
MPEA	Multi-principal-element alloy
PDF	pair distribution function
PHEV	Plug-in hybrid electric vehicle
PMA	Perpendicular Magnetic Anisotropy
PVD	physical vapor deposition
REE	Rare earth element
REXS	Resonant Elastic X-ray Scattering
RIXS	Resonant Inelastic X-ray Scattering
SASE	Self Amplification of Spontaneous Emission
SAXS	Small-angle x-ray scattering
SEM	Scanning Electron Microscope

SSD	Solid State Drive
TEM	Transmission Electron Microscope
VSM	Vibrating Sample Magnetometer
X-PEEM	X-ray Photoemission Electron Microscopy
XAS	X-ray Absorption Spectroscopy
XFEL	x-ray free-electron laser
XFTH	X-ray fourier transform holography
XMCD	X-ray Magnetic Circular Dichroism
XMLD	X-ray Magnetic Linear Dichroism
XPCI	X-ray phase contrast imaging
XPCS	X-ray photon correlation spectroscopy
XRD	X-ray diffraction
ZFC	Zero Field Cooling

Chapter 1

Introduction and motivation

Alloying has been a key contributor to advancements in material properties. Human beings have been modifying the properties of metals by incorporating small amounts of alloying elements since ancient times. For instance, during the Neolithic period or the Bronze Age, alloys of copper-zinc (brass) and copper-tin (bronze), were extensively utilized. Although copper-based alloys were commonly used in decorative arts, their use in structural applications was limited due to their inadequate mechanical properties. The discovery of iron alloying techniques during the Iron Age brought about a paradigm shift in structural applications such as sword and armor making. Craftsmen in Japan, India, and Mesopotamia had already mastered the art of tempering and hardening iron before their European counterparts; however, these techniques were entirely empirical [1].

The current understanding of iron and steel production was established in the nineteenth century when chemical analysis techniques matured, and the role of carbon alloying was firmly established in regulating the structural properties of iron alloys. In the 21st century, iron and its alloys are widely used as building materials (carbon steel), electromagnet cores (grain-oriented silicon steel), permanent magnets (NdFeB), and in numerous other applications.

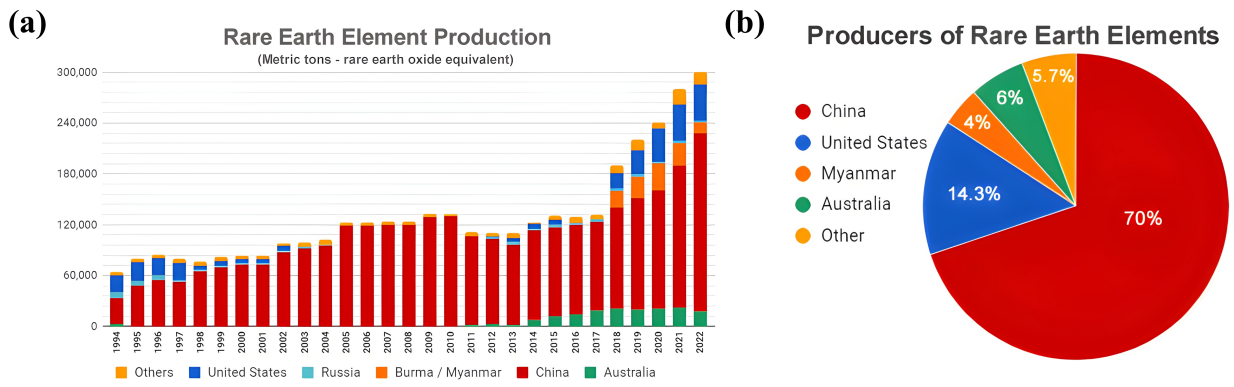

Figure 1.1: Figure **(a)** shows worldwide rare earth elements (REEs) production from 1994 to 2022. A dramatic increase of 170 % in the production was seen in the last decade. **(b)** show a pie chart with the leading producers of REEs [4].

Even though the *d-Block* elements like *Fe*, *Co*, *Cr*, *Ni* and their classic alloys play a huge role in our current economy, the push towards sustainable technologies is primarily driven by rare earth (*Lanthanides*) elements. REEs are elements with atomic number ranging from 57 (*lanthanum*) to 71 (*lutetium*) and even though they are fairly abundant in earths crust, concentrated deposits are hard to come by earning them the rare earth moniker. Their special nuclear, metallurgical, chemical, catalytic, electrical, magnetic, and optical properties make them extremely valuable in applications ranging from magnets, catalysis, batteries, lasers, high-temperature superconductivity, data storage etc.

Recent report by U.S. Geological Survey [2] show that the global production of REEs have increased by 170 % (see Fig. 1.1(a)) in the last few decades. This dramatic increase in production and demand is in part fueled by the mass adoption of EVs as production of each vehicle consumes $\approx$ 15 kg of REEs [3]. But the REEs supply chain is heavily controlled by China which accounts for 70 % of the worldwide production in 2022 as shown in figure Fig. 1.1(b). This supply consolidation along with increased demand for REEs have led to exponential increase in their price in the last decade.

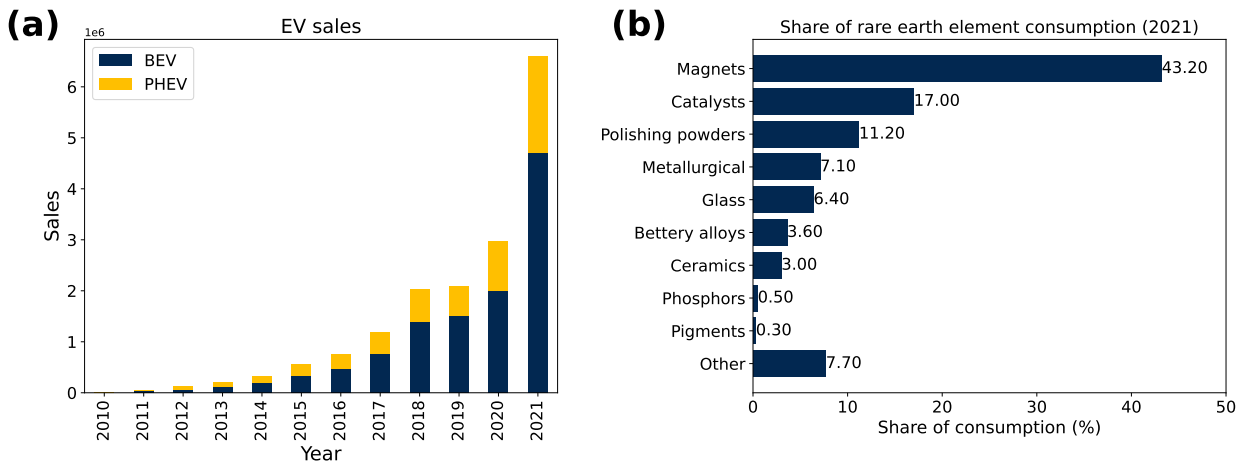

Figure 1.2: Figure **(a)** shows worldwide electric vehicle sales from 2010 to 2021. A huge increase in adoption of battery electric vehicles (BEV) and plug-in hybrid electric vehicles (PHEV) [5] can be seen starting $\approx$ 2015. **(b)** shows share of REEs used in different applications [6].

Fig. 1.2(a) shows sales of Battery electric vehicles (BEVs) and Plug-in hybrid electric vehicles (PHEVs) for years ranging from 2010 to 2021. The exponential growth in EVs adoption is clearly evident from these sales figures. However mass adoption might plateau in the near future and be limited to developed economies due to the high cost and reliance on REEs like neodymium in electric motors. So, in order to facilitate mass adoption of EVs, new rare earth free magnets need to be developed. Furthermore, to reduce the consumption of REEs, rare earth free catalysts need to be developed too as catalysis is the second-largest consumer of REEs as shown in Fig. 1.2(b). So, currently there is a huge push towards developing materials with properties on demand and High entropy alloys (HEAs) or Multi-principal-element alloys (MPEAs) are a promising candidates due to the infinitely large compositional space.

1.1 Introduction to MPEAs

In 2004, Cantor et al. [7] and Yeh et al. [8] introduced a novel alloying philosophy involving the use of four or more major elements often with equiatomic concentration. These alloys are referred to as high-entropy alloys (HEAs) or multi-principal element alloys (MPEAs). The development of MPEAs was motivated by the potential entropy-driven suppression of phase separation. For example, let us look at a binary alloy with element A and B. The Gibbs free energy of formation for a solid solution is given by Eq. (1.1) where G_{mix} is the Gibbs free energy, H_{mix} is the enthalpy, S_{mix} is the entropy of mixing and T is the absolute temperature [9].

$$\Delta G_{\text{mix}} = \Delta H_{\text{mix}} - T\Delta S_{\text{mix}} \tag{1.1}$$

$$\Delta G_{\text{f}} = \Delta H_{\text{f}} - T\Delta S_{\text{f}} \tag{1.2}$$

Similarly, one can also define the Gibbs free energy of intermetallic compound formation with a stoichiometry AB as shown in Eq. (1.2). The formation of intermetallic vs random solid solution is controlled by the balance between the Eq. (1.1) and Eq. (1.2). If G_{mix} is more negative than G_{f}, solid solution is formed. Whereas if G_{f} is more negative, intermetallic compound AB is formed. One important thing to note is that the aforementioned example is very simplified as there can be other intermetallics with different stoichiometries (A_iB_j where i and j are integers ranging from 1 to n). In which case one would have to write Eq. (1.2) for all the possible intermetallics. Thinking about HEAs/MPEAs with five or more elements, Eqs. (1.1) and (1.2) become extremely complicated because of the increased number of possible intermetallic compounds. However, Yeh et al. [8] proposed that if an alloy contains five or more elements the configurational entropy, dominates and results in

stabilization of a single solid solution phase. Since the publication of this seminal paper, HEAs or MPEAs have attracted a great deal of attention due to their novel properties such as excellent low temperature strength and fracture toughness [9–11].

While the structural and compositional aspects of bulk MPEA have been widely explored, magnetic properties of these alloys in thin film geometry are still in a nebulous phase. When examining the most common MPEAs, it becomes evident that at least one constituent element is either ferromagnetic (Fe, Co, and Ni) or antiferromagnetic (Mn and Cr) in nature. This characteristic, coupled with the vast compositional space offered by MPEAs, opens up possibilities for the discovery of new magnetic alloys. These alloys have the potential to serve as alternatives to rare earth-based permanent magnets, which have witnessed a surge in demand over the past two decades, largely driven by the rise of electric vehicles as discussed in the previous section.

In the recent reviews on electrical and magnetic properties of MPEA [12, 13], alloys containing more than 50 at.% of the magnetic elements (Fe, Co, and Ni) were found to be paramagnetic or soft ferromagnetic (FM) with relatively low saturation magnetization and coercivity in comparison with pure iron. On the other hand, in equiatomic MPEA, recent temperature dependent studies done by Schneeweiss et al. [14] reported that equiatomic CrMnFeCoNi undergoes two magnetic transformations: paramagnetic to spin glass at 93 K and spin glass to FM at 38 K. In a different MPEA system, CrCoNiFeZr, where Cr, Co, Ni, and Fe are equiatomic and Zr is varied from 0.4 to 0.5 at.%, coexistence of two FM phases was observed at lower temperatures and the transition temperature was found to be dependent on the composition [15]. These recent studies highlight complex magnetic properties of MPEA; however, a systematic understanding of magnetism is still lacking in a wide variety of MPEA systems. Furthermore, most of the studies have focused on the bulk samples, and the magnetic behavior of MPEA in thin film form still remains unexplored.

Thin film confinement can enhance saturation magnetization and enable tuning of magnetic phases and transition temperature [16–18].

1.2 FeCoCrMnSi system

One of the MPEAs that has piqued the interest of researchers who study structural behaviour of materials is $Fe_{80-x}Mn_xCo_{10}Cr_{10}$ (at%) system. For most materials increase in strength comes at the cost of ductility which is referred to as strength-ductility trade-off [19, 20]. However, Li et al. [21] recently reported that $Fe_{80-x}Mn_xCo_{10}Cr_{10}$ is able to overcome this strength-ductility trade-off due to its metastable dual phase nature. This alloy has coexisting face-centered cubic (f.c.c) and hexagonal close-packed (h.c.p) phases and mechanical loading causes a martensitic f.c.c to h.c.p transformation. This martensitic phase transformation leads to higher ductility for dual phase alloy compared to single phase alloys. Fig. 1.3 plots the stress strain curve for the aforementioned system and shows that in the dual phase case (red curves), when the grain size is decreased, both strength and ductility increased. Whereas, for single phase case (lower black curve) refining the grain size also decreased the ductility of the sample.

While the mechanical properties of this system has been explored, a fundamental microscopic understanding of magnetic properties of MPEAs is still lacking. Miracle and Senkov [10] have proposed that the enhanced mechanical properties of these MPEAs could in part be due to their magnetic entropy and magnetic properties. In first half of this thesis in Chapters 3 and 4 I am going to primarily explore the magnetic properties of $Fe_{80-x}Mn_xCo_{10}Cr_{10}$ like system $Fe_{39.8}Co_{19.9}Mn_{20.5}Cr_{14.8}Si_5$.

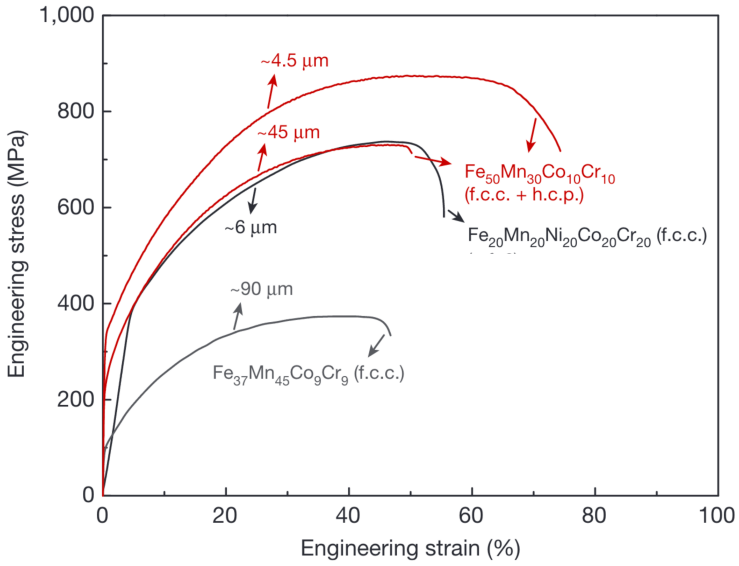

Figure 1.3: Figure shows engineering stress and strain curve for $Fe_{80-x}Mn_xCo_{10}Cr_{10}$ system for different values of x and compares it to FeMnNiCoCr system [21].

1.3 Introduction to ultrafast magnetization dynamics

In the current era, information technology has revolutionized our life and have had huge impact on both our day to day lifestyle and have aided in discovery of new physics. Recently released Artificial Intelligence (AI) tools like DeepMind's AlphaFold has been described as "astounding" and "transformational" due to its ability to accurately predict protein structures and aiding in discovery of new drugs [22]. At the heart of all these AI advances is Dynamic random-access memory (DRAM) which enables training of these large scale AI models on Graphics processing units (GPUs). However, the parameter size for the current generation AI models has already ballooned to 100s of billions. In order to scale to larger models, there is a need for more energy efficient and higher density DRAM technologies. As the current DRAM is volatile in nature which means it requires a constant bias to store information leading to huge energy consumption as joule heating and the switching speed is

limited to nanosecond timescales. So, there is coordinated push towards new technologies for data storage which are potentially faster and have lower energy footprint.

One such promising technology is spin based electronics or *spintronics*. This field started with the discovery of Giant Magnetoresistance (GMR) which is used in the read and write heads of hard disk drives enabling high density data storage [23]. In classical spintronics magnetic field or spin currents were utilized to manipulate the state of system which limited the speeds to sub-nanosecond regime [24] making it undesirable. Optical control of spintronics was the next breakthrough where ultrafast control of magnetization with ultrashort laser pulses was demonstrated by Beaurepaire et al. [25] for a Ni thin film. An ultrafast decrease of 40 % in magnetization was observed within a picosecond of laser excitation for a Ni thin film system as shown in Fig. 1.4(a). This ushered in a new pathway to manipulate spintronics at ps timescales which was six order of magnitude faster than the conventional spin current or magnetic field based routes.

Though this 40 % quench in magnetization within few pecosecond is very interesting in terms of exploring fundamental physics, it is not suitable for making storage devices which require switching from up (1) to down (0) state. Most of digital data in the world is stored on spinning hard disk drives, which store information in a thin film of ferromagnetic material made out of CoPtCr based alloy [26]. Even though the use of spinning hard disk drives in commercial electronics have wained due to the advent of Solid State Drives (SSDs), which are two orders of magnitude faster than spinning hard disk drives and based on charge traps [27], hard disk drives are more economical which lends them the upper hand in cloud storage applications. So, there is a concerted push towards optical control of spin state of magnetic thin films which would be able to supersede hard disk drives.

The first successful deterministic switching was reported by Stanciu et al. [28] when they demonstrated that ferrimagnetic GdFeCo system can be switched from up to down state

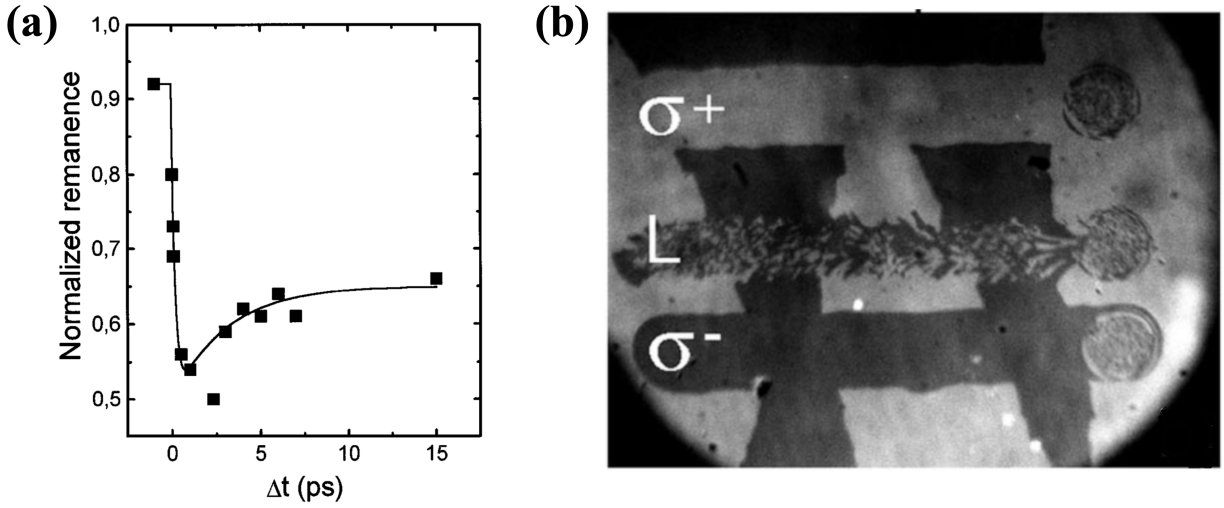

Figure 1.4: **(a)** Ultrafast demagnetization in Ni thin film pumped with an 800 nm optical laser [25]. **(b)** Helicity dependent all optical switching in $Gd_{22}Fe_{74.6}Co_{3.4}$ sample [28]. σ^+ and σ^- denote the positive and negative helicity of 800 nm pump laser and L is linearly polarized pump.

using circularly polarized light as shown in Fig. 1.4(b). Subsequent studies over the years have confirmed similar ultrafast switching in various alloy systems, marking this as an active area of research [29–36]. But all the aforementioned studies primarily focused on uniformly magnetized systems which are unstable on macroscopic lengthscales due to *magnetostatic energy* [37]. Most systems will have multiple domains and understanding the effects of optical excitation on the various domain morphologies present in magnetic texture is crucial for commercial viability of spintronics.

Before diving into the ultrafast response of textured magnetic system, a short introduction on the mechanisms of ultrafast demagnetization are in order. Magnetism is intimately linked to angular momentum of electrons, so in order to switch magnetization, angular momentum transfer is required. Multiple mechanisms have been proposed to explain ultrafast quench in magnetization all of which fall into two main categories:

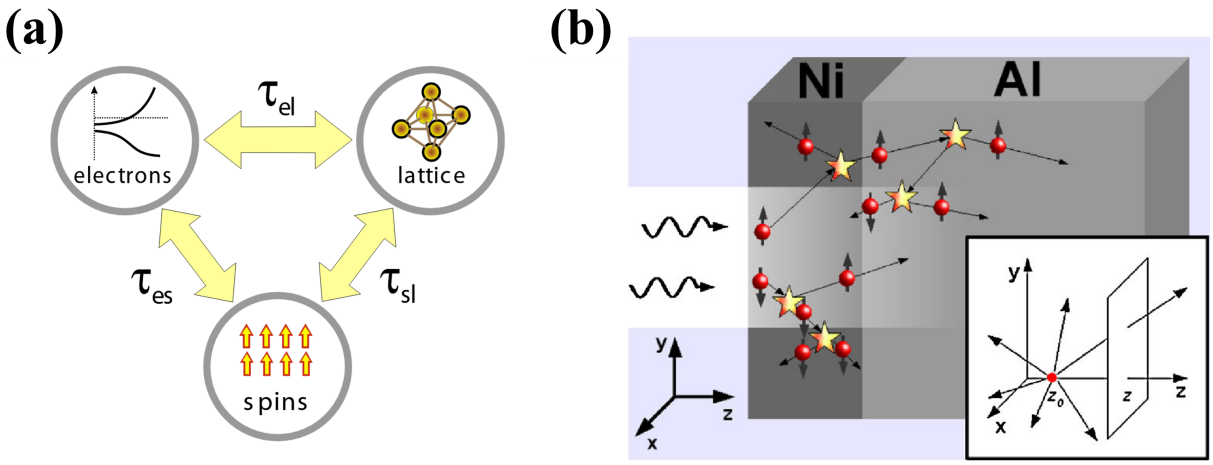

Figure 1.5: Two primary mechanisms proposed for ultrafast demagnetization: **(a)** spin-flip scattering models involving electron, spin, and lattice interactions that transfer angular momentum to the lattice [38], and **(b)** superdiffusive spin current models where angular momentum is transferred by spin-polarized currents [39]. The former considers spin reversals prompted by electron-phonon and electron-magnon collisions that reduce the net magnetization rapidly. The latter involves spin transport driven by majority spin electron flow in response to laser heating.

1. *Spin-flip scattering model*: The spin-flip scattering model proposes that ultrafast demagnetization occurs due to the transfer of angular momentum from the electron spin system to the lattice through electron-phonon and electron-magnon spin-flip scattering events [40, 41]. In this model, the initial laser excitation causes hot electron distributions which can then interact and scatter off phonons or magnons, flipping the electron's spin in the process and thus transferring spin angular momentum to the lattice vibrations and magnon modes [40]. The model combines the three temperature framework for electrons, spins, and lattice with electron-phonon spin-flip probabilities (see Fig. 1.5(a)) to quantitatively explain demagnetization dynamics [42]. It predicts demagnetization time is directly proportional to the spin-flip probability, and inversely proportional to the Curie temperature and spinless electronic density of states near

Fermi level [43]. This explains differences in demagnetization timescales between transition metals and rare earth metals based on their differing spin-flip probabilities and densities of states. Some experimental observations like wavelength-dependence of demagnetization rates support the model [44]. However, challenges remain, like the short lifetime of hot electrons compared to the demagnetization time. Overall, the spin-flip scattering model provides a microscopic mechanism for ultrafast angular momentum transfer from the spin system to the lattice through electron-phonon [45] and electron-magnon spin flip events that lead to demagnetization on femtosecond timescales.

2. *Superdiffusive spin current model*: The superdiffusive spin current model proposes that ultrafast demagnetization is driven by transport of spin-polarized electrons, rather than spin-flip scattering events [39]. In this model, the laser excitation generates hot electrons that can propagate rapidly through the material as a spin current, carrying away their spin angular momentum. The lifetime difference between majority and minority spin electrons leads to a spin-asymmetry in the superdiffusive current (see Fig. 1.5(b)), resulting in a net loss of spin angular momentum and demagnetization. Since this mechanism does not rely on electron-phonon interactions, it can explain the ultrafast demagnetization times faster than the electron-phonon thermalization timescale. The model has been applied to explain demagnetization dynamics in metallic ferromagnets, multilayers, and differences between metals and insulators [46]. Experimental observations such as fluence-dependent demagnetization magnitudes and timescales, and effects related to spin transport like influence on demagnetization in an adjacent layer, provide support for superdiffusive spin currents playing a role [47–49]. However, the model has been challenged by Schellekens et al. [50] who reported superdiffusive spin transport appears to make minimal contributions to demagnetization in Ni thin films.

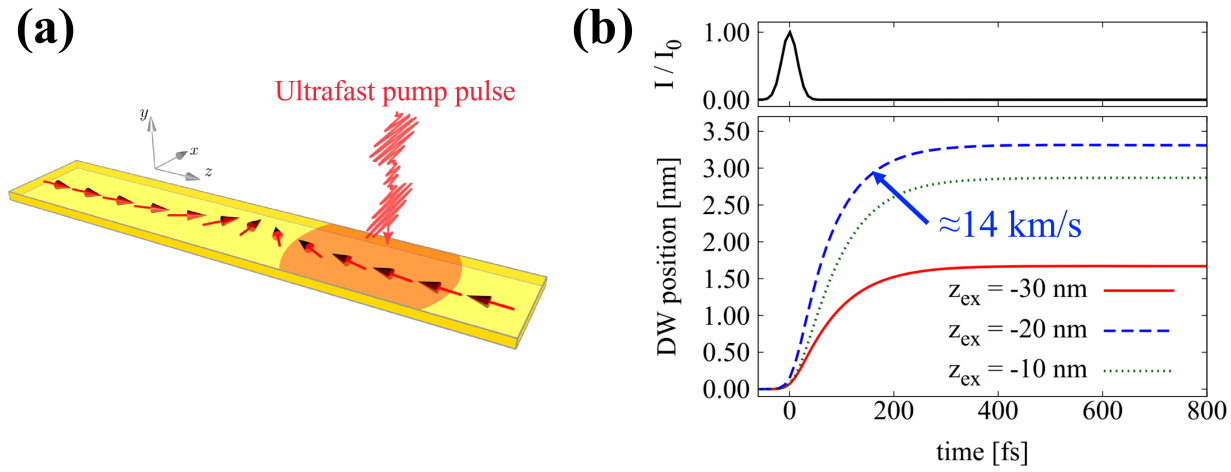

Figure 1.6: **(a)** shows a schematic of head-to-head domain wall and asymmetrically positioned laser pump. **(b)** top shows the Gaussian laser pulse profile with FWHM 35 fs while bottom sub-figure shows the time dependent domain wall position as a function of laser spot distance (z_{ex}) from the domain wall [51].

To summarize, the relative contributions of spin-flip scattering and superdiffusive spin transport to ultrafast demagnetization remain an open question. Both models have theoretical and experimental support, but the dominant mechanism is unclear. This thesis does not focus on validating one model over the other. However, superdiffusive spin currents are invoked as a potential explanation for some experimental results presented in Chapter 5. While further work is needed to fully delineate the roles of local and nonlocal processes, considering possible superdiffusive effects provides useful insight into the complex ultrafast demagnetization dynamics in the materials studied here.

1.4 Ultrafast domain dynamics

The ability to manipulate mesoscopic-scale magnetization [52] has potential applications in ultra-low power magnetic memory and logic [53–55]. For example, current-driven domain

wall speeds greater than 5 km/s have been demonstrated with bilayers composed of a compensated ferrimagnet and Pt [54]. Exceeding these current-driven domain wall speeds is dependent either on future material breakthroughs or developing novel routes for controlling magnetic behavior. Far-from-equilibrium physics [56, 57] in ultrafast conditions [58–60] offer a unique possibility due to the introduction of novel dissipative pathways that are not accessible under equilibrium. In fact, a recent theoretical study by Baláž et al. [51] predicts that extremely fast domain wall speeds of $\approx$ 14 km/s in ferromagnets (see Fig. 1.6) can be achieved via optical pumping due to superdiffusive spin currents [39]. This is a remarkable prediction as it exceeds the generally accepted maximum speed for ferromagnets of $\approx$100 m/s for domain walls. Domain walls, which can be considered as bound magnetic solitons (localized nonlinear excitations with finite energy) [61], undergo Walker-breakdown above these speeds and the soliton-like structure of a domain wall becomes unstable [62, 63]. At low velocities, the internal spins of the domain wall precess coherently as it moves, enabling stable domain wall motion. However, above a critical velocity known as the Walker breakdown speed, the internal spins cannot precess fast enough to keep up with the moving domain wall. This results in non-uniform precession, with some spins falling out of synchrony with the overall domain wall motion. Consequently, the domain wall structure becomes periodically distorted, forming transient vortex-like defects, inhibiting further acceleration [62, 63]. This optically driven domain wall velocities higher than Walker-breakdown speeds would imply that ultrafast spin dynamics not only result in an overall demagnetization but can also affect the long-range spatial structure of magnetic domains over several tens of nanometers.

While ultrafast demagnetization, as discussed in the previous section, is well established for a wide variety of ferromagnetic materials [24, 38], only a few studies have hinted towards the ultrafast modification of nanoscale domain pattern [64–66]. The first reports of optical excitation of textured systems were by Vodungbo et al. [67] and Pfau et al. [64] for stripe

and labyrinth domain symmetries respectively. Vodungbo et al. [67] studied the [Co(0.4 nm)/Pd(0.6 nm)]$_{30}$ using infrared (815 nm) pump and tabletop High Harmonic Generation (HHG) Extreme Ultraviolet (EUV) (20.66 nm) probe with <100 nm spatial and 40 fs temporal resolution. The stripe magnetic domain structure acts as a diffraction grating for the soft x-rays, producing a resonant magnetic scattering pattern. Tracking the intensity of the diffraction spots as a function of pump-probe delay reveals the magnetization dynamics. Whereas tracking the position of the diffraction spots reveals the domain structure dynamics. Locally, the magnetization within each domain exhibits an ultrafast demagnetization within $\approx$ 100 fs, consistent with prior work. Fig. 1.7(a) shows the azimuthally integrated scattering from the stripe magnetic domain pattern as a function of time delay reported by Vodungbo et al. [67] where no shift in the scattered peak position was observed. This indicates that no rearrangement of domains occurred at ultrafast timescales for stripe domain symmetry. Surprisingly, the demagnetization time is shorter compared to previous optical experiments and shows minimal fluence dependence. The overall magnetic domain structure remains unchanged through the demagnetization process. The presence of alternating magnetic domains with opposite spin polarization is proposed to accelerate demagnetization through direct transfer of angular momentum between neighboring domains.

Fig. 1.7(b) shows the results reported by Pfau et al. [64] for Pt(50)/[Co(8)/Pt(14)]$_1$6/Pt(6) (Å) multilayer sample that support labyrinth domains (see MFM image in Fig. 1.7(b)). Similar to Vodungbo et al. [67] the magnetization within each domain shows an ultrafast drop, similar to previous work on uniform ferromagnetic films. However, x-ray scattering pattern shifts on a sub-picosecond timescale, indicating changes in the domain pattern. This shift was explained by broadening of domain walls due to superdiffusive spin currents moving across the wall. This leads to a change in the magnetic form factor, resulting in a shift of peak position.

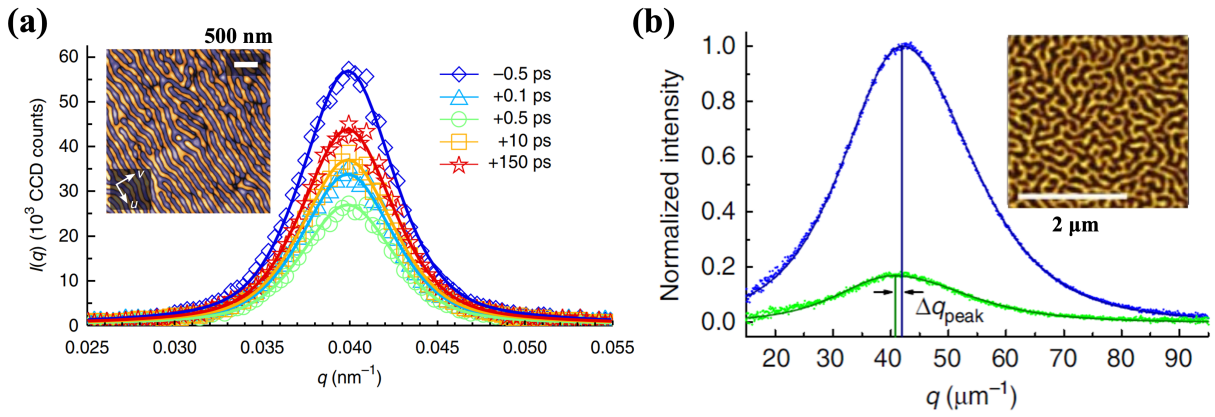

Figure 1.7: **(a)** shows ultrafast response of stripe domains shown in inset for [Co(0.4 nm)/Pd(0.6 nm)]$_3$0 system as a function of delay time [67]. **(b)** shows response for labyrinthine domains shown in MFM image in inset for [Co(0.8 nm)/Pt(1.4 nm)]$_{16}$ system before laser pump (blue curve) and at 1.3 ps delay (green curve) after pump at maximum demagnetization [64].

However, subsequent investigations into these textured systems by Zusin et al. [65] and Zhou Hagström et al. [66] have contradicted the notion of domain wall broadening as the mechanism for the observed ultrafast shift. These studies, while disproving this explanation, have not definitively elucidated the precise mechanisms underlying the ultrafast distortions of diffraction patterns, leaving the possibility of domain rearrangement still viable. Consequently, the mechanism behind the shift observed initially by Pfau et al. [64] and subsequently by Zusin et al. [65] remains enigmatic. In Chapter 5 of this thesis, I concentrate on comprehending the ultrafast modification of domain patterns following laser excitation in CoFe/Ni multilayers, which support a mixed labyrinthine and stripe domains, investigating its dependence on fluence and timescales. Employing small angle x-ray scattering with femtosecond temporal and nanometer spatial resolutions, I address the following unresolved questions: the morphology dependence of ultrafast domain modification, the fluence dependence of this process, the timescales involved in domain morphology changes, and the

potential mechanism underlying the morphology-dependent ultrafast domain modification.

1.5 Summary

This chapter serves as an introduction, outlining the motivation behind investigating the magnetic properties of MPEAs and the ultrafast magnetization dynamics of textured magnetic systems. Additionally, open questions in both areas which will be explored in detail throughout my thesis are introduced. The primary focus of this work revolves around two key aspects: first, the macroscopic and element-specific magnetization of MPEAs, and second, the ultrafast domain dynamics of textured magnetic multilayers. In Chapter 2 essential methods and techniques utilized to study these magnetic systems are introduced and elaborated upon. Chapter 3 delves into the growth and characterization of MPEA thin films, employing sputtering techniques and analyzing results through X-ray diffraction (XRD), Scanning Electron Microscope (SEM), and Transmission Electron Microscope (TEM). Chapter 4 presents the magnetic property findings of MPEAs, delving into the results and discussions surrounding these intriguing materials. Subsequently, Chapter 5 delves into the ultrafast magnetization dynamics of CoFe/Ni multilayer systems, showcasing the obtained results. Finally, in Chapter 6, the thesis concludes with an outlook for future avenues that can be explored in the domains of both MPEAs and ultrafast magnetization dynamics. This section opens up exciting possibilities for further research and investigations in these fascinating fields.

Chapter 2

Experimental Methods

In this chapter I discuss the various experimental methods used in my thesis. First I discuss thin film growth including sputtering, and magnetic characterization including hysteresis loop measurements, zero field cooling and field cooling measurements etc. The key aspects of work performed in this thesis utilizes X-ray based techniques. So in the second section in this chapter, I introduce X-ray sources and then discuss the other characterization techniques such as X-ray Absorption Spectroscopy (XAS), X-ray Magnetic Circular Dichroism (XMCD), Small-angle x-ray scattering (SAXS).

2.1 Sputtering

Sputtering is a thin film deposition technique belonging to the physical vapor deposition (PVD) class where material is removed from a target and deposited on a substrate. Sputtering, among the various techniques for thin film deposition, stands out as a cost-effective and convenient method that ensures compositional fidelity between the film and the target material. In the sputtering process, a bias potential is applied between the substrate and the target within a chamber filled with a noble gas such as Argon (Ar), as depicted in Fig. 2.1.

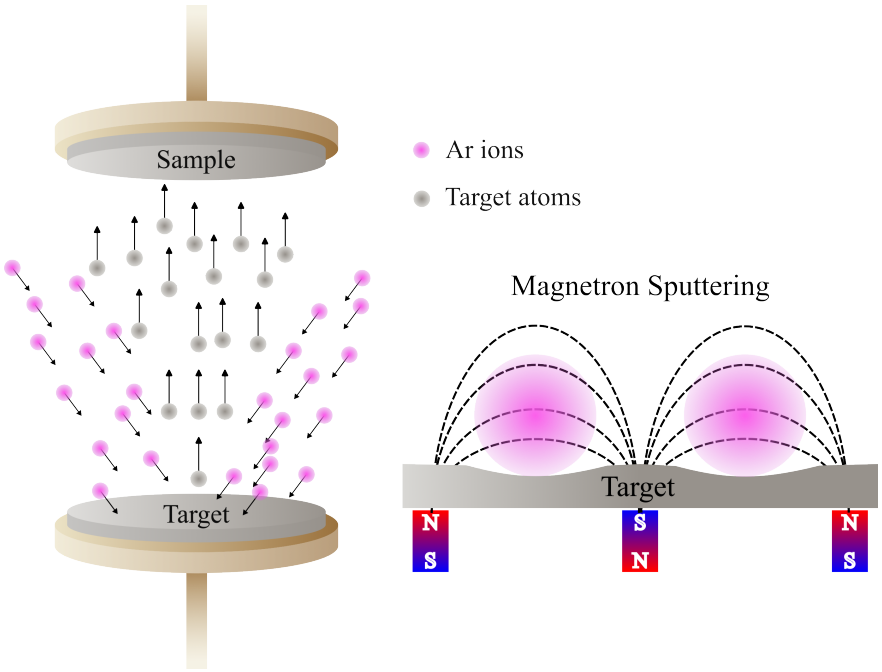

Figure 2.1: Figure on left shows schematic of sputtering where Ar plasma impinges on the target due to a applied potential difference. On the right is a schematic of magnetron sputtering where permanent magnets are used to confine the Ar plasma right next to the target, improving the sputter yield.

This environment facilitates the ionization of Ar gas atoms (magenta atoms in Fig. 2.1), attracting and bombarding these ions onto the negatively biased target. As a result, atoms are dislodged from the target (gray atoms in Fig. 2.1) and precisely deposited onto the substrate, creating the desired thin film structure.

One of the major advantages of sputtering is its ability to maintain the same composition as the target material. Although the sputter yield for each element may vary by an order of magnitude, the sputtering process quickly reaches an equilibrium composition at the target surface, which may differ from the bulk target composition. Interestingly, once this equilibrium stage is reached, the sputtered film attains the same composition as the target. Furthermore, in conventional sputtering systems, the deposition rate is typically

low; however, this limitation can be significantly overcome by employing strong permanent magnets to confine the plasma above the target, as illustrated in the right side of Fig. 2.1.

2.2 Energy Dispersive Spectroscopy

Energy Dispersive Spectroscopy (EDS) is a electron in X-ray out technique where, electron beam from the SEM or TEM knocks a core shell electron out of the atoms in the sample. Electrons from the outer shell drop down to the core shell to fill the hole created and release a photon with the energy equal to the difference in binding energies of the outer and inner shell. EDS measurements can be performed with an SEM or TEM. For further information on EDS please refer to chapter 4 of Goldstein et al. [68].

SEM microscopy and EDS spectra measurements for thin film samples should be performed at very low acceleration voltage so as to maximize the interaction of the thin film with the electron beam. At higher acceleration voltages, very small signal is seen from the thin film as electron beam penetrates through the film and primarily interacts with the substrate. However, one can not go below 5 keV of acceleration voltage as below that the intensity of the characteristic X-ray emitted drops precipitously. So, the EDS results measured using SEM presented in Chapter 4 were all measured at 5 keV acceleration voltage.

2.3 Bulk Magnetic Measurements

Bulk magnetic ordering was measured using *Vibrating Sample Magnetometer (VSM)*, which is based on the principle of *Faraday's Law of Induction*. It measures the induced Electromotive Force (EMF) produced by vibrating the sample between a set of pickup coils. Furthermore, an electromagnet or a superconducting magnet can be used to apply a DC or AC magnetic field to study the magnetization out of remanence. This allows us to mea-

sure the magnetization of sample as a function of applied external field (hysteresis loops) and ascertain the coercivity, remanence magnetization and saturation magnetization. It can also be used for comprehensive characterization of various magnetic materials, including ferromagnetic, paramagnetic, and antiferromagnetic substances.

2.3.1 DC susceptibility

The bulk magnetic properties like coercivity, remanence, and absolute magnetization are all extrinsic in nature and depend on the history of sample. These quantities can not be used to compare and contrast two magnetic systems. However DC susceptibility (χ) is a fundamental intrinsic property that characterizes the response of a material to an applied magnetic field in the direct current (DC) regime. It is a measure of how easily a material can be magnetized in response to an external magnetic field and is expressed as follows:

$$\chi = \lim_{H \to 0} \frac{M}{H} \tag{2.1}$$

where M is the magnetization of sample and H is the applied field. In general χ measurements are done in the paramagnetic regime and can be used to characterize the nature of a magnetic sample. It follows Curie-Weiss law in paramagnetic regime which is given by:

$$\chi = \frac{C}{T - \theta_p} \tag{2.2}$$

where C is the Curie constant, θ_p is the paramagnetic Curie temperature and T is the absolute temperature in kelvin. θ_p is zero, positive and negative for paramagnets, ferromagnets and antiferromagnets respectively.

Magnetic materials undergo transitions as a function of temperature where the long range ordering in the material changes due to the thermal energy being high enough to overcome

the exchange [69]. These transitions can be studied by measuring magnetization as a function of temperature using VSM following a specific measurement protocol outlined below:

1. Zero Field Cooling (ZFC): In zero field cooling the sample is cooled in zero applied external field down to a desired temperature. After reaching this desired temperature the magnetization of the sample is measured during heating with a small applied field (10s of Oe).

2. Field Cooling (FC): In field cooling the sample is cooled in applied external field (5-100,000 Oe or more) down to a desired temperature. After which the magnetization of the sample is measured during heating with the same applied external field.

If a ferromagnetic transition is present in a material, ZFC and FC would overlap as on top of each other as the system reaches the same magnetization state for both protocols. If however the system undergoes a non-equilibrium transition like spin glass, ZFC and FC would not overlap. This ZFC and FC protocol was used in to study the bulk magnetic transitions for MPEA presented in Chapter 4.

2.3.2 Aging measurements

There are many magnetic system like spin glasses and superparamagnets where magnetization changes as a function of time i.e. the system shows *Aging*. If the magnetic system exhibits aging on a timescale of tens of seconds, which is significantly slower than the measurement timescales for magnetization using VSM, one can employ time-dependent magnetization measurements to study the aging process within the system using VSM. The rate of change of magnetization can be used to study the dynamics in these magnetic systems. A schematic for aging measurement protocol is shown in Fig. 2.2. The sample is first cooled in zero applied field below the spin glass transition temperature (T_S) followed unpreturbed

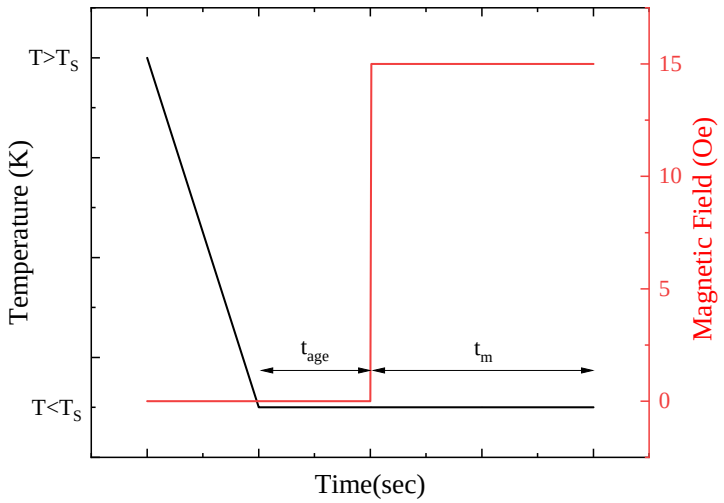

Figure 2.2: Figure shows the measurement setup for aging measurements done to study spin glass behavior.

aging of the system for aging time (t_{age}). Magnetization of the system is than recorded as as a small external field is applied as shown in Fig. 2.2. This method will be utilized to ascertain the presence of spin glasses in MPEA discussed in Chapter 4

2.4 X-Ray sources

One of the most paradigm shifting discoveries of the 19th century was arguably the discovery of x-rays by Wilhelm Conrad Röntgen [70]. Since their discovery, x-rays have made seminal impact on numerous fields of research ranging from physics, chemistry, biology, materials science, medicine and many more. X-rays are photons with wavelength ranging from 10^{-8} to 10^{-12} m. They are primarily generated using two methods. First is using X-ray tubes which works on the principle of fluorescence where a core electron from an atom is knocked out using accelerated electrons which leaves a core hole in the atom. This core hole is unstable and is filled by an outer electron falling into the core shell and giving out an x-ray photon in

the process. The second method of x-ray production involves accelerating charged particles usually done in synchrotrons and x-ray free-electron lasers (XFELs).

2.4.1 X-ray tube

During the early 20th century, most X-ray-based diffractometers employed vacuum discharge tubes for the production of x-rays via Bremsstrahlung radiation and X-ray fluorescence. Bremsstrahlung radiation, derived from the German term for "breaking radiation", refers to the production of radiation through the braking of electrons by a target material. A schematic of an X-ray tube is presented in Fig. 2.3(a). The device comprises of a filament that is heated to a high temperature, which results in the emission of electrons via thermionic emission. The electrons are then accelerated due to the potential difference (typically ranging from $\approx$ 15 to 50 kV) between the filament and the target. The high-energy electron beam then impinges upon the target, leading to the production of x-rays through both the Bremsstrahlung radiation and X-ray fluorescence mechanisms (see Fig. 2.3(b)). Bremsstrahlung can be explained by combining relativistic physics with Maxwell's equations and is the consequence of finite velocity of light [71]. A charge particle in vacuum has electric field lines emanating from it and propagating till infinity. If this charge particle is at rest or moving at a constant velocity with respect to the reference frame of the observer, the field lines also appear to move uniformly as shown in Fig. 2.4(a). Now if the charge particle is accelerated, the field lines near it respond to the updated position of the charge particle, but the field lines far away still point to the old location of the particle because the information about the updated position of the particle travels at the speed of light which is finite. Between these two regimes of field lines are distorted (see Fig. 2.4(b)) and that is the electromagnetic wave propagating outwards [71].

Most lab based X-ray diffractometers use X-ray tubes with copper or molybdenum as a

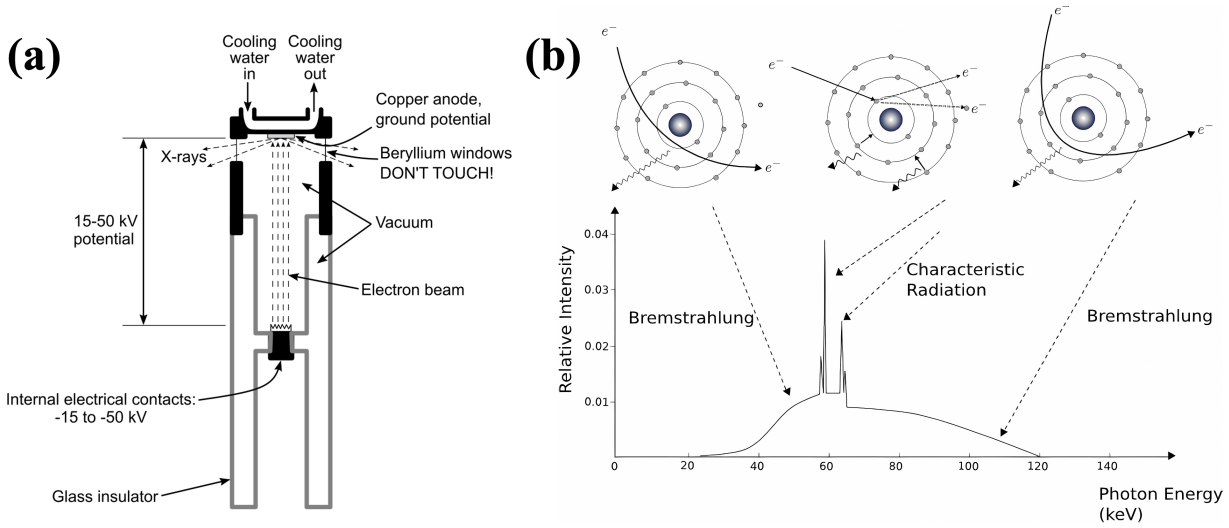

Figure 2.3: Figure **(a)** shows a schematic of X-ray tube and **(b)** shows X-ray spectrum for copper target [72, 73].

target element. The primary reason for using copper as target material is its high thermal conductivity and relatively high melting point, which enables it to withstand high temperatures caused by electron bombardment. A chiller with constant water flow is used to cool the copper target. The generated x-rays escape the tube through Beryllium windows with minimal attenuation due to the low atomic mass of Beryllium. Fig. 2.3(b) shows the Bremsstrahlung effect at atomic scale where the incoming electrons are deflected (transverse acceleration) by the nucleus of the target atom giving out a photon in the process. This manifests as a broad background in X-ray spectrum as seen in Fig. 2.3(b), although most diffraction experiments do not utilize this radiation. The primary beam used for diffraction experiments is the characteristic X-rays generated by the target via fluorescence mechanism because of its narrow width in energy. Copper primarily generates three characteristic emission lines, $K_{\alpha 1}$ ($L_3 \rightarrow K_1$ transition, $\lambda = 1.5405$ Å), $K_{\alpha 2}$ ($L_2 \rightarrow K_1$ transition, $\lambda = 1.5443$ Å) and K_β ($M_3 \rightarrow K_1$ transition,$\lambda = 1.3922$ Å). $K_{\alpha 1}$ and $K_{\alpha 2}$ are very close in energy are

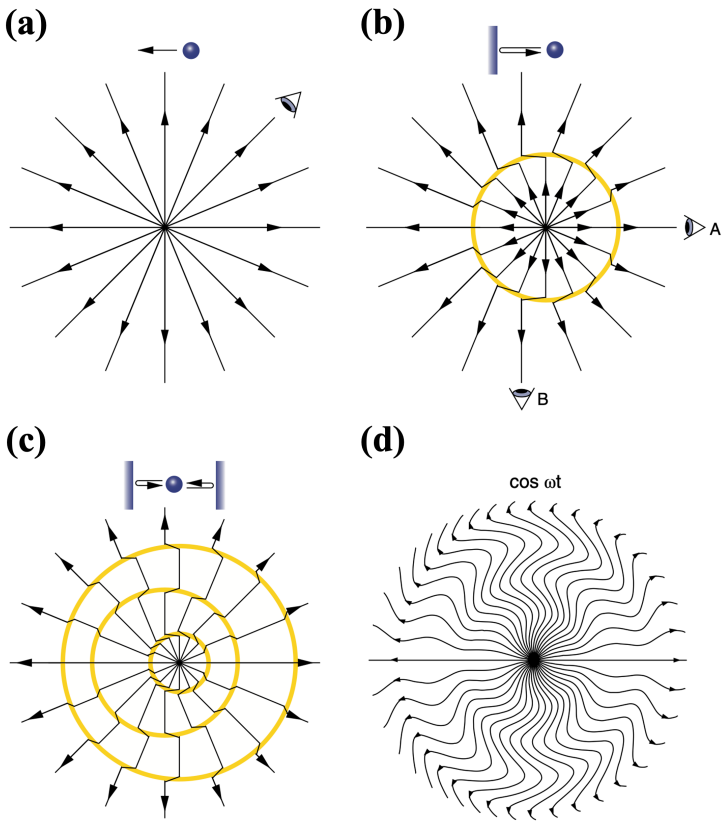

Figure 2.4: Figure shows how accelerating a charge particle produces radiation. **(a)** shows a charge particle moving at a constant velocity which does not generate any radiation. **(b)** shows a charge particle reflecting of an infinite potential which produces a pulse of EM wave which can be observed everywhere other than along the axis of acceleration or point A. The yellow circle denotes the event horizon traveling at the speed of light. **(c)** shows a charge particle oscillating back and forth between two potentials which produces temporally equidistant radiation pulses. **(d)** shows the case where a particle oscillates in a simple harmonic motion radiating at the oscillating frequency of the driving force. [74]

generally used for diffraction experiments in most setups whereas K_β has a higher energy but does not give additional information during diffraction experiment so it is filtered out using a nickel foil filters.

2.4.2 Synchrotrons

Synchrotorns were originally built to study electron-electron or positron-positron collisions but were converted to x-ray sources starting 50 years ago [75, 76]. Since 1997 they have enabled six discoveries (1997:P. D. Boyer and J. E. Walker, 2003:R. MacKinnon and P. Agre, 2006:R. D. Kornberg, 2009:V. Ramakrishnan, T. A. Steitz, and A. E. Yonath, 2012:R. J. Lefkowitz and B. K. Kobilka, 2018:F. H. Arnold) that have been awarded the Nobel Prize [74]. In synchrotrons electrons traveling almost at the speed of light are subjected to large accelerations using *insertion devices*, perpendicular to their direction of motion resulting in radiation. A schematic of a typical synchrotron is shown in Fig. 2.5. Electrons are produced using a gun via thermionic emission, which are accelerated to relativistic velocities using the linear accelerator (LINAC) and booster ring. They are then injected into the storage ring where *insertion devices* like wigglers or undulators are used to generate x-rays which are used by the beamlines. Bend magnets are used to keep electron bunches in the booster ring and also provide additional x-rays for measurements. RF sources are used to accelerate electron bunches again as they lose energy via radiation in the synchrotron. The spectrum for synchrotron radiation ranges from infrared to hard x-rays and the radiation is highly collimated, coherent, polarized with very high intensity. Furthermore, recent advances have resulted in faster than Moore's law increase in the brightness of x-ray sources. These qualities make them an indispensable and versatile tool for studying any kind of material system. Synchrotrons have made a significant impact in the field of protein crystallography, enabling the solving of over 70,000 structures that have been deposited in the protein data bank until 2016 [77].

Brilliance for photon sources is defined as photons flux per second normalized by the beam area, beam solid angle and the bandwidth. It is customary to use 0.1% bandwidth around the central frequency of x-rays. This has been formalized in the Eq. (2.3) and has

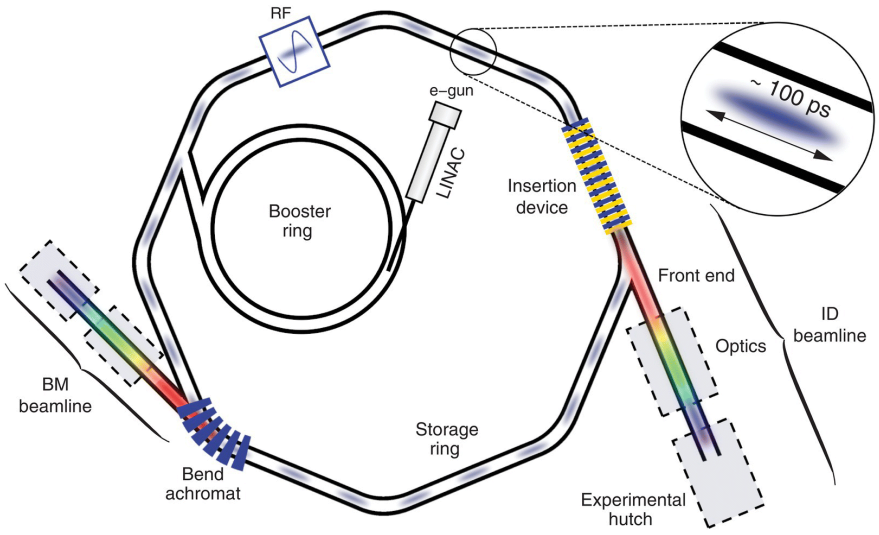

Figure 2.5: Figure shows a schematic of a typical synchrotron where an electron bunch in the storage ring is accelerated using *insertion devices*. This acceleration leads to generation of x-rays, the mechanism of which is discussed in the text [74].

the units of photon/s/mm^2/mrad^2/0.1% bandwidth [74].

$$B = \frac{\dot{N}_{ph}}{4\pi^2 \sigma_x \sigma_y \sigma_{x'} \sigma_{y'} \frac{d\omega}{\omega}} \tag{2.3}$$

where $\dot{N}_{ph}$ is the photon flux, σ_x and σ_y are the root mean square size of the beam in x and y direction, $\sigma_{x'}$ and $\sigma_{y'}$ are the solid angles in x and y, and $\frac{d\omega}{\omega}$ is the bandwidth around central frequency.

The key advantage of synchrotron over conventional vacuum tube based sources it the high photon flux, high coherence, polarization control and tunable energy. High photon flux enables diffraction measurements from small amount of sample, samples with low scattering cross section like from ferroelectric and magnetic ordering peaks and materials lacking long range order like glasses. High temporal and spatial coherence enables measurements like X-ray photon correlation spectroscopy (XPCS), X-ray phase contrast imaging (XPCI), X-

ray fourier transform holography (XFTH), Small-Angle X-ray Scattering (SAXS) etc. The ability to control the x-ray energy enables element specificity where measurements are done at absorption edge of an element present in the sample. Some examples of resonant measurements are X-ray Magnetic Circular Dichroism (XMCD), X-ray Magnetic Linear Dichroism (XMLD), Resonant Elastic X-ray Scattering (REXS), Resonant Inelastic X-ray Scattering (RIXS) etc. all of which require precise control of x-ray energy with sub eV resolution and X-ray polarization in some cases. Resonant absorption will be further discussed in Section 2.6.1

Let's delve into the physics of photon generation in synchrotrons (or x-ray free electron lasers which will be discussed in next subsection). Dispersion relationship for electron and photon, which describes the energy-momentum relationship can be written as follows:

$$\gamma = \sqrt{1 + (\beta\gamma)^2} \tag{2.4}$$

where γ here is the energy, β is velocity and $\beta\gamma$ is the momentum. Fig. 2.6(a) shows the plot for this dispersion relationship for a particle and a photon. Energy of the photon plotted is normalized ($\gamma_p = \epsilon_p/mc^2$ ϵ_p is the energy of photon) by the rest mass of the electron for comparison. Let us now think of a photon being emitted by the particle with an energy equal to $\Delta\gamma_p$. This process is shown on the dispersion curve in Fig. 2.6(b). Due to energy-momentum conservation laws, the particle has to lose same amount of energy and momentum but this not possible because energy momentum of the particle need to be located on the dispersion line. This means that absorption or emission of a photon is not permitted for a particle in vacuum because that would violate energy-momentum conservation laws. On the other hand a particle in a medium with refractive index large than one (not in vacuum) does not violate the conservation laws and can radiate, this is called Cherenkov Radiation.

To explain the why accelerating a charge particle perpendicular to its direction of motion produces photons, let's consider the energy-momentum conservation for a three body system

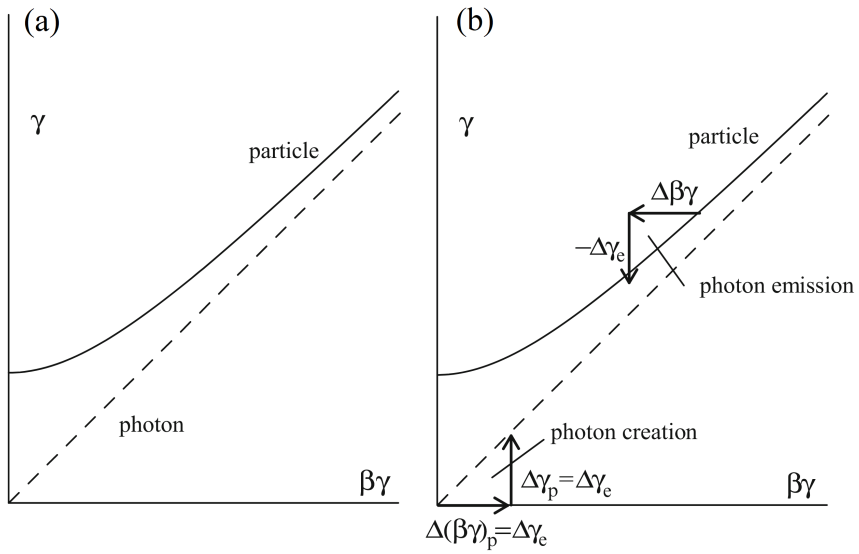

Figure 2.6: Figure shows the dispersion relationship for both a particle and photon [71].

with two photons and a particle which is shown in Fig. 2.7. The electron collides with an incoming low energy photon, absorbing it which increase the energy of the electron but it losses momentum in the process to reach an intermediate stage after which it radiates a photon of different higher energy. This process does not violate any conservation laws. Although it raises the question of where the incoming photon comes from in a synchrotron or free electron laser? Considering the electrons frame of reference, static magnetic fields from a *insertion device* or bend magnet, appear as virtual electromagnetic radiation which it collides with. This process is called *Compton* effect and is the key mechanism at play in all synchrotron and free electron sources. In summary, *Compton* effect is a three body process where electrons in the storage ring traveling at relativistic velocities interact with the magnetic fields of *insertion devices*, leading to production of radiation.

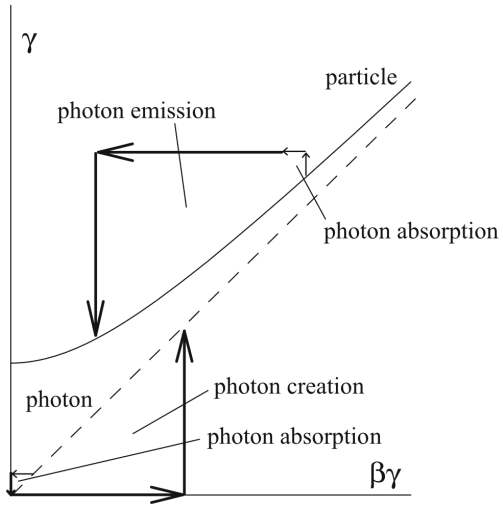

Figure 2.7: Energy momentum conservation for Compton scattering process [71].

2.4.2.1 Insertion devices

As discussed above, in order to accelerate the electrons to produce x-rays, *insertion devices* are used. There are four primary kinds of devices being used at synchrotron which are as follows:-

1. Bend magnet:- The incoming electron beam is bent in the plane of synchrotron using an electromagnet or super conducting magnet. The number of radiated photons (N_f) is proportional to the number of electrons (N_e) in the electron beam bunch.

2. Wiggler:- The incoming electron beam is wiggled in a sinusoidal path in the plane of synchrotron using an array of permanent magnets. The number of radiated photons (N_f) is proportional to the number of electrons (N_e) in the electron beam bunch and the number of wiggler periods (N).

3. Undulator:- The incoming electron beam is wiggled in a sinusoidal path in the plane of synchrotron using an array of permanent magnets with very short period. The number

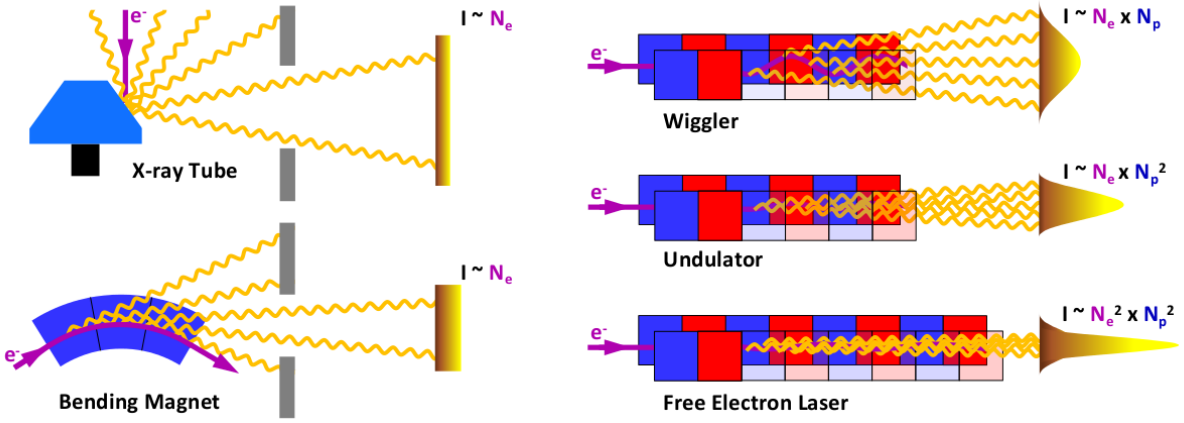

Figure 2.8: X-ray sources and insertion devices. The figure also shows the dependence of intensity as a function of number of electrons (N_e) in the beam and number of magnetic poles (N_p) in the insertion device [78].

of radiated photons (N_f) is proportional to the number of electrons (N_e) in the electron beam bunch and the square of number of wiggler periods (N).

A schematic of these three aforementioned *insertion devices* is shown in Figs. 2.5 and 2.8.

2.4.3 XFELs

Although synchrotron radiation offers high tunability, its relative lack of spatial coherence (transverse to the x-ray propagation direction), limited picosecond temporal resolution, and low peak brightness impose limitations on its application for studying molecular or spin dynamics. The degree of spatial coherence for a synchrotron, represented by the fractional coherence (f_{coh}), is proportional to the square of the wavelength (λ) divided by the bandwidth ($\Delta\lambda$).

$$f_{coh} = \frac{1}{2}\frac{\lambda^2}{\Delta\lambda} \tag{2.5}$$

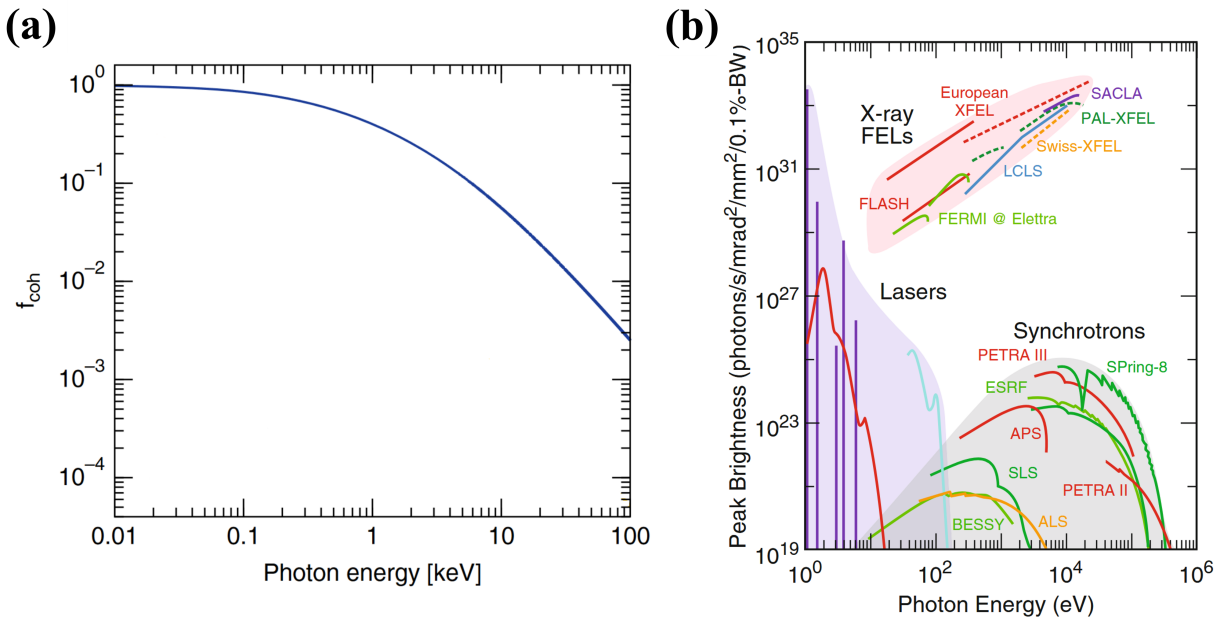

Figure 2.9: **(a)** Coherence fraction of synchrotron. [74]. **(b)** Peak brightness as a function of photon energy for table top laser based, synchrotrons and free electron laser sources [79].

At high photon energies, typically around 10 keV, which are often employed in coherent diffraction experiments, the fractional coherence drops significantly to approximately 10% (see Fig. 2.9(a)).

Furthermore, temporal resolution of synchrotrons is restricted to the order of tens of picoseconds, which hinders its capability to investigate phenomena occurring at femtosecond timescales, such as molecular or spin dynamics. Fig. 2.10 compares the temporal and spatial length-scales for various fundamental processes with the available characterization tools. It is quite evident that synchrotrons do not posses the temporal resolution required to study spin dynamics which is of paramount interest for understanding ultrafast domain dynamics. Additionally, the inability to use temporal averaging for studying ultrafast phenomena necessitates high peak brightness from the source to achieve sufficient signal-to-noise ratios. A

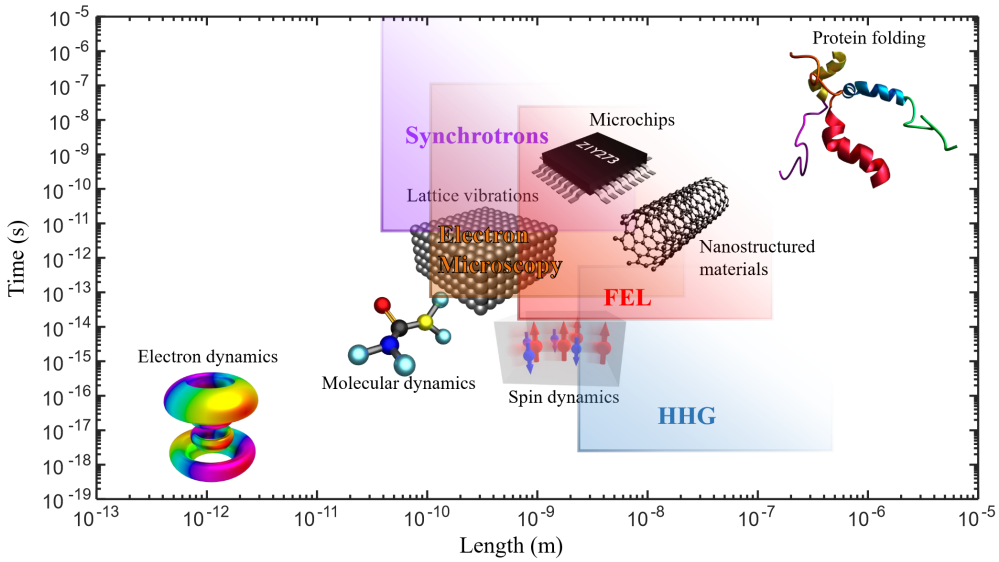

Figure 2.10: Length and timescales of fundamental processes compared to temporal and spatial resolution of various characterization tools [80].

comparison of peak brightness versus photon energy for table-top laser sources, synchrotrons, and XFELs (see Fig. 2.9(b)) highlights that synchrotrons are ten orders of magnitude less bright than XFELs. These shortcomings, encompassing poor coherence, ps temporal resolution, and relatively lower peak brightness, underscore the limitations of synchrotron sources for studying ultrafast phenomenon.

To combat these spatial coherence, temporal resolution and brightness issues, ideas were borrowed from conventional laser systems which led to the development of XFELs. They provide extremely intense, spatially coherent x-ray pulses with pulse-width ranging from 10 fs to 50 fs. These fs pulses contain the same number of photons that one can get a synchrotron facility in 1 second which corresponds to an increase in brightness of ten orders of magnitude [71]. This opens the possibility to study matter at its intrinsic length and time scales, which is angstroms and femtoseconds, respectively as shown in Fig. 2.10.

FELs are based on the principal of Self Amplification of Spontaneous Emission (SASE), a

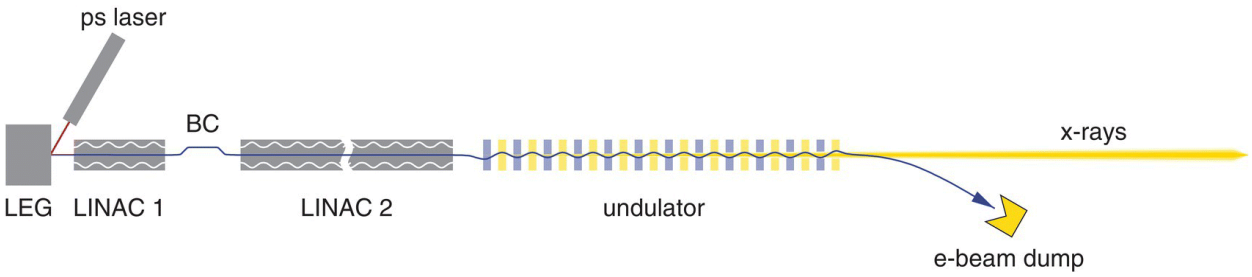

Figure 2.11: Figure shows a schematic of typical XFEL where an electron bunch in the storage ring is accelerated using *insertion devices*. This acceleration leads to generation of x-rays, the mechanism of which is discussed in the text [74].

stochastic and spontaneous process which was first proposed by Rodolfo Bonifacio, Claudio Pellegrini, and Lorenzo Narducci in 1984 [81]. A detailed discussion on SASE is out of the scope for this thesis but readers can find information in Jaeschke [71] chapter 4. A schematic of an typical XFEL is shown in Fig. 2.11. The main components include a low-emittance gun (LEG) which when irradiated with a ps laser, produces electron bunches. This bunch is then accelerated in LINAC and compressed in longitudinal direction using a bunch-compressor magnet chicane (BC) which is proceeded by acceleration through another section of LINAC. After this the bunch enters a long undulator ($\approx$ 100 m long), which generates highly coherent x-ray pulses with fs width. The bunch is then dumped in an e-beam dump made of lead. The x-rays produced are generally employed by one beamline at a time for experiments, in contrast to synchrotrons, where multiple beamlines access x-rays simultaneously. Consequently, the cost of a single measurement at an XFEL is an order of magnitude higher compared to synchrotrons.

In recent years, considerable advancements have been made in tabletop x-ray sources based on HHG, however they are limited to photon energies below 100 eV. A comprehensive discussion of HHG is beyond the scope of this thesis, and interested readers are encouraged to refer to Zusin [80].

2.5 X-ray interaction with material

When x-rays interact with matter, they can undergo several distinct processes. These include inelastic scattering (Compton), elastic scattering (Thomson), Auger electron generation, and fluorescence, as illustrated in Fig. 2.12. In the energy range of synchrotrons and XFELs, represented by the yellow shaded region in Fig. 2.13, the dominant processes are photoelectric absorption (indicated by the red curve also called resonant absorption) and Thomson scattering (indicated by the blue curve) so the discussions in upcoming sections will primarily focus on these two processes. The scattering or absorption cross section, which quantifies the length over which the intensity of x-rays is reduced to 1/e of the incoming intensity, plays a crucial role in understanding these interactions. So the following few sections introduce scattering and absorption cross section for both non-resonant and resonant processes.

2.5.1 Non-resonant X-ray interactions

Non-resonant interactions occur when the x-ray energy is far from any electronic transitions in the material. Non-resonant X-ray interactions play a crucial role in various X-ray techniques like X-ray Diffraction (XRD), X-ray Reflectivity (XRR) to name a few. They provide valuable information about the structure of materials without requiring specific knowledge of the electronic energy levels or excitation processes within the material.

Elastic scattering off-resonance is called *Thomson scattering*. Electric field vector of incident x-rays will cause the electrons to oscillate with π phase shift which causes them to radiate as discussed in previous section. Thomson scattering cross section in soft x-ray regime can be approximated as:

$$\sigma_T = \frac{8\pi}{3} r_0^2 Z^2 \tag{2.6}$$

where Z is the atomic number, r_0 is the Thomson scattering length and is equal to 2.82×10^{-6}

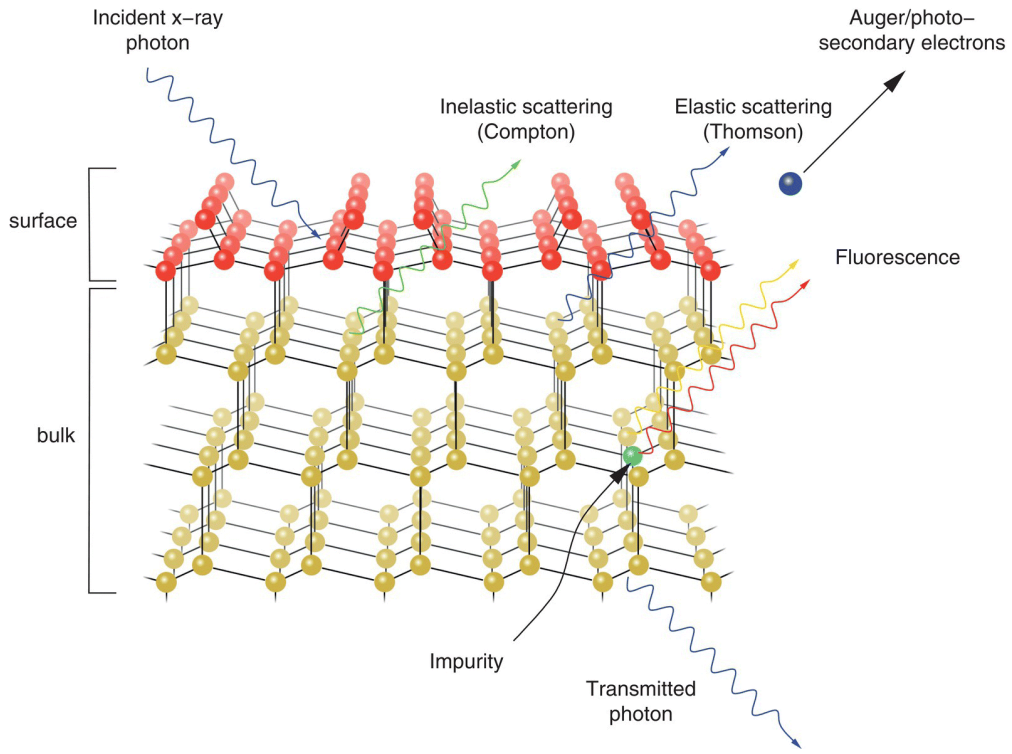

Figure 2.12: Interactions of X-rays with matter [74].

nm. This means that in the soft x-ray regime scattering is independent of photon energy.

The absorption of x-rays in a material is given by Beer-Lambert law which defines the change in intensity of light as it travels through a medium. It is defined as a function of z, which is the depth traveled by the x-rays from the surface.

$$I(z) = I_0 e^{-\mu_x z} \tag{2.7}$$

where I_0 is the incoming intensity and μ_x is the absorption coefficient which is related to the absorption cross section (σ^{abs}) and atomic number density (ρ_a) as follows:

$$\mu_x = \rho_a \sigma^{abs} \tag{2.8}$$

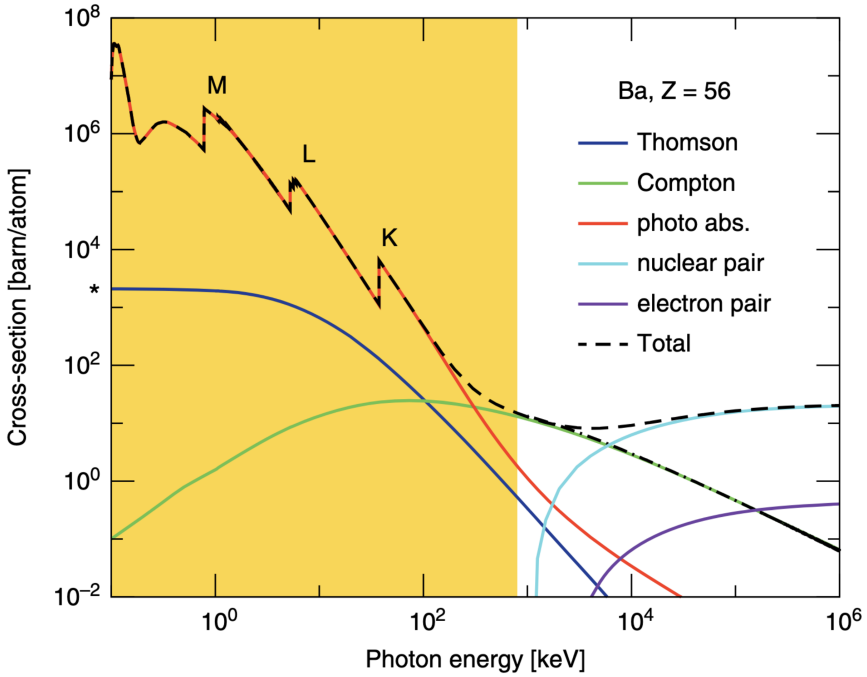

Figure 2.13: Scattering cross section as a function of incoming X-ray energies for various processes barium (Ba). Yellow shaded region indicates the energy range covered by modern synchrotrons and XFELs [74].

Furthermore, x-ray absorption coefficient can be written as follows:

$$\sigma^{abs} = \frac{4\pi}{\lambda \rho_a} \beta \tag{2.9}$$

where β is the imaginary part of complex refractive index which can be written as $n = 1 - \delta + i\beta$ where n is the refractive index δ is the dispersion term and β is the absorption term. This relationship shows that absorption is lower for long wavelength (low energy) x-rays.

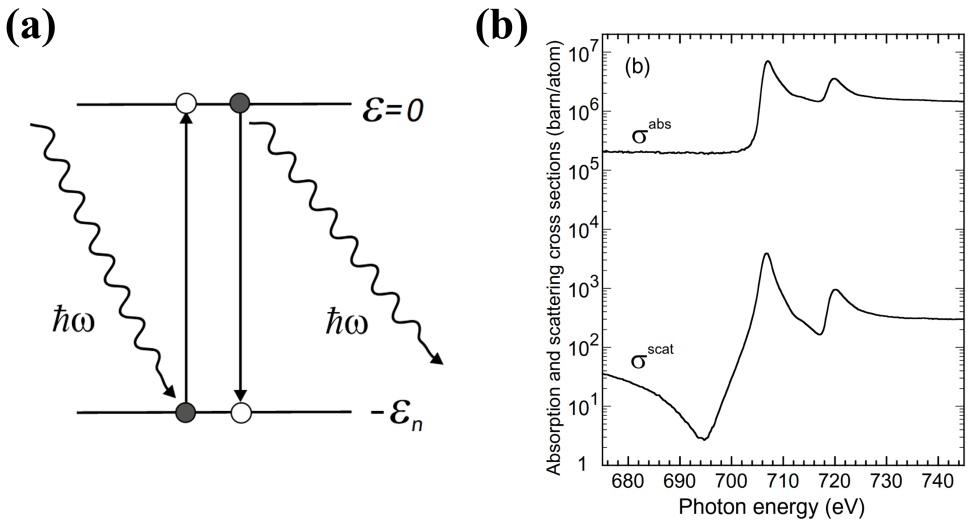

Figure 2.14: **(a)** shows a resonant process in a simple one electron framework. **(b)** shows the absorption and scattering cross section for iron metal around $L_{3,2}$-edge [82].

2.5.2 Resonant X-ray interactions

Resonant interactions occur when the incoming x-ray photons have energy comparable to the electronic transition of a material. Resonant measurements provide element or ordering specificity to scattering or absorption experiments. The incoming photon is absorbed by a core electron exciting it to an empty state near Fermi level and this absorption is the x-ray absorption step (see Fig. 2.14(a)). As the core hole is unstable and has a finite lifetime, the excited electron decays back into the core shell by emission of a photon of the same energy it absorbed. This re-emission is Resonant X-ray scattering as shown in Fig. 2.14(a). Resonant scattering ($\sigma_{\text{scat}}^{\text{res}}$) and absorption (σ_{abs}) cross section can be derived using semi-classical

approach and is approximated as [82]:

$$\sigma_{\text{scat}}^{\text{res}} = \frac{8\pi}{3} r_0^2 \frac{\mathcal{E}_n^2}{\Gamma_n^2} \frac{(\Gamma_n/2)^2}{(\hbar\omega - \mathcal{E}_n)^2 + (\Gamma_n/2)^2} \tag{2.10}$$

$$\sigma_{\text{abs}} = 2\lambda r_0 \frac{\mathcal{E}_n}{\Gamma_n} \frac{(\Gamma_n/2)^2}{(\hbar\omega - \mathcal{E}_n)^2 + (\Gamma_n/2)^2} \tag{2.11}$$

where r_0 is the Thomson scattering length and is equal to 2.82×10^{-6} nm, ω is the angular frequency of the incoming radiation, the resonance width $\Gamma_n = \hbar\Delta_n$ and the resonance position $\mathcal{E} = \hbar\omega_n$. Fig. 2.14(b) shows the absorption and scattering cross section derived using the aforementioned equations for iron near $L_{3,2}$-edge. The key thing to note is the three to four orders of magnitude lower value for σ_{scat} compared to σ_{abs} even at resonance. This is one of the key reasons why resonance scattering measurements require synchrotron or FEL sources as very high photon flux is required for getting good signal to noise ratio.

2.6 X-ray Absorption Spectroscopy

Any technique that directly or indirectly probes the material with varying energy of the probe is called spectroscopy. In XAS the sample is probed using X-ray as a function of wavelength/energy. The sample response can be recorded using multiple methods ranging (a) absorbed intensity in case of transmission geometry or (b) photoelectron yield in case of opaque samples. Fig. 2.15 shows XAS spectra for Fe, Co, Ni and Cu measured near L edges ($2p \rightarrow 3d$ transition). The shape of XAS curve near the edge of an element is defined by it's local environment and density of states (DOS) at Fermi level (DOS in $3d$ level for example shown in Fig. 2.15) [83]. One of the biggest strengths of XAS is the element specific nature of the technique. So, it can be used to isolate the response of a single element present in samples with multiple constituent elements.

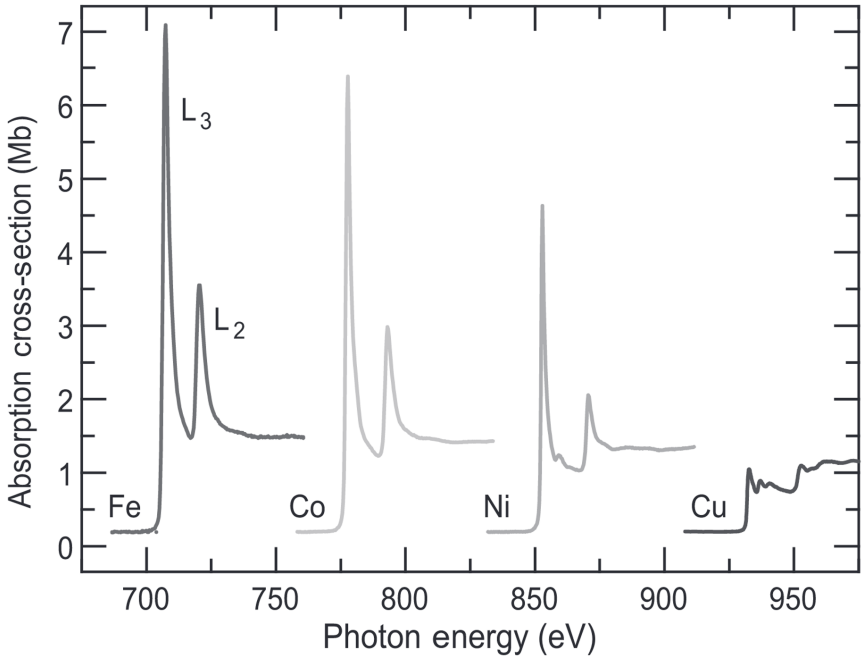

Figure 2.15: XAS spectra at L_2 and L_3 edge for Fe, Co, Ni and Cu [83].

The aforementioned XAS can also be used to probe element specific magnetization using X-rays that are circular or linear polarized. The absorbed intensity for XAS depends on the transition probabilities per unit time from a state $|i\rangle$ to another state $|f\rangle$ which is defined by *Fermi's Golden Rule* [83]:

$$T_{i\to f} = \frac{2\pi}{\hbar} \left|\langle f \left|\mathcal{H}_{\text{int}}\right| i\rangle\right|^2 \rho\left(\varepsilon_f\right). \tag{2.12}$$

where $\mathcal{H}_{\text{int}}$ is the interaction Hamiltonian between the initial and final states and $\rho\left(\varepsilon_f\right)$ is the DOS in final state. The interaction Hamiltonian for X-ray absorption depends on the momentum operator $\boldsymbol{p}$ and vector potential $\boldsymbol{A}$

$$\left|\mathcal{H}_{\text{int}}\right| = \frac{e}{m_e}\boldsymbol{pA}. \tag{2.13}$$

In free space/vacuum, $E = -\partial A/\partial t$, so it is the electric field vector of light that couples with the electron in core shell during transition.

2.6.1 X-ray Magnetic Circular Dichroism

Now if we use circularly polarized light for which electric field vector rotates as a function time and which has an angular momentum, it is preferentially absorbed by a spin up or down. Furthermore, because the transition probabilities depend on the density of states at Fermi level which are different from for majority vs minority spins in magnetic elements due to exchange splitting (see Fig. 2.16(a)), X-rays with the angular momentum vector k parallel to the minority spins (it has more DOS to transition to) is absorbed more. These two effects combined result in dichroic effect aka disparity in the absorption of X-ray being dependent on the chirality of polarization for magnetic systems as shown in Fig. 2.16(b). All this can be summarized in a two step model for XMCD [83]:

1. In step one, the circularly polarized x-rays generate photoelectrons with either spin up or down.

2. In step two, the exchange split valence level in magnetic system serves as a detector for the spin polarized photoelectrons generated in step one.

The intensity of dichroism effect, which is the difference between XAS of two chairality of x-rays, is proportional to the degree of circular polarization (P_{circ}), magnetic moment ($\boldsymbol{m}$) of the element and angle between the X-rays angular momentum ($\boldsymbol{L_{ph}}$) and magnetic moment. This can be summarized in the following equation[83]:

$$I_{XMCD} \propto P_{circ}\, \boldsymbol{m} \cdot \boldsymbol{L_{ph}}. \tag{2.14}$$

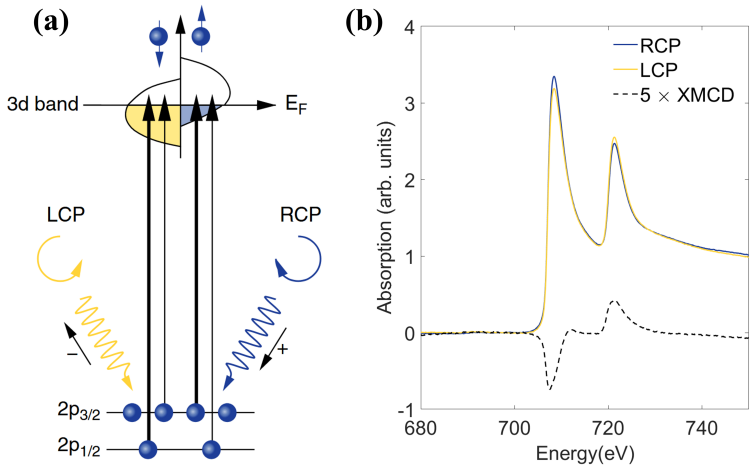

Figure 2.16: **(a)** Absorption of RCP photons mainly excites spin-up electrons, while LCP light mainly excites spin-down electrons, resulting in a dichroic absorption spectrum, shown in **(b)** for the L-edge of iron [74]. The difference between the two polarization is XMCD and is shown in **(b)** in dashed black line.

For maximum XMCD effect, $\boldsymbol{m}$ and $\boldsymbol{L_{ph}}$ should be collinear. In general XMCD can be measured either by changing the polarization of X-ray or the magnetization direction of the sample; both are equivalent. If we assume that the measured sample contains no anisotropic charge or spin densities, for example a polycrystalline sample, one can calculate the average spin and orbital moment per atom using the following three sum rules:

1. The first sum rule is called the *charge sum rule* and it can be used to determine the number of holes (N_h) in valance state per atom given the integrated intensity under an XAS curve (see Fig. 2.17) at both L_3 and L_2 edge using the following relation

$$\langle I_{L_3} + I_{L_2} \rangle = C N_h \tag{2.15}$$

where C is a proportionality constant and I_{L_3} and I_{L_2} are integrated intensities under the XAS curve at L_3 and L_2 edge after subtracting the non-resonant component as

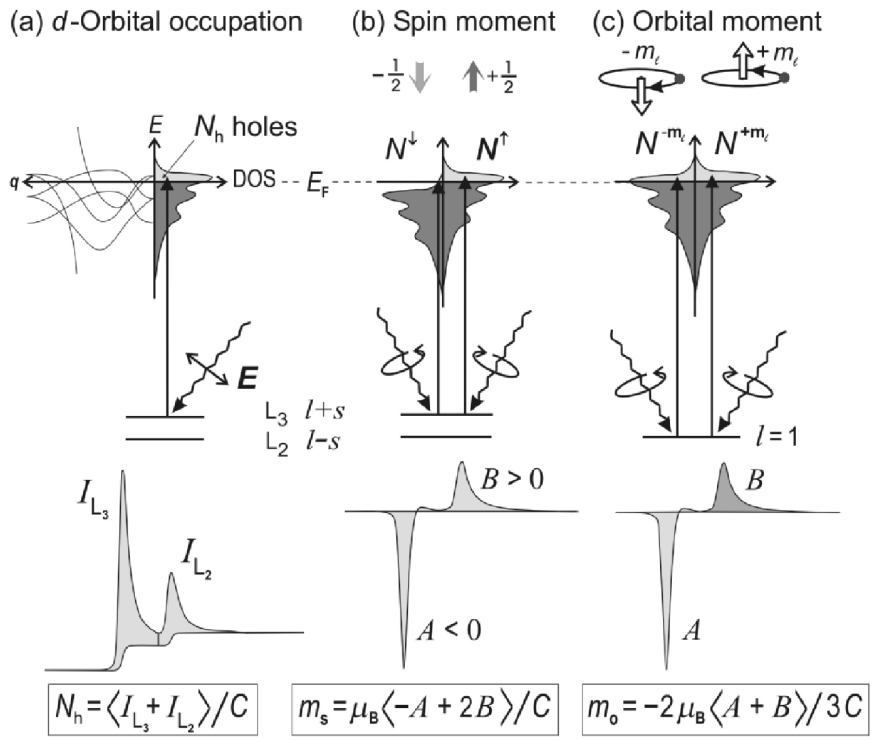

Figure 2.17: Figure shows the three sum rules for XMCD and the corresponding processes involved. **(a)** show the *charge sum rule* which can be used to determined number of holes in valance state. **(b)** show the *spin sum rule* used to determined spin per atom. **(c)** show the *orbital moment sum rule* used to determine orbital moment per atom [83].

shown in Fig. 2.17(a).

2. The second sum rule is called the *spin sum rule* and it links the integrated intensities at L_3 and L_2 edges with the spin moment (m_s) per atom according to following relation:

$$\langle A + 2B \rangle = \frac{C}{\mu_B} m_s \tag{2.16}$$

where A and B are integrated intensities under the XMCD curve at L_3 and L_2 edge as shown in Fig. 2.17(b) and C is the same proportionality factor as the first rule.

3. Third and final rule is called *orbital momentum sum rule* which links the XMCD integrated intensities (A and B) to the orbital angular momentum (m_o) per atom (see Fig. 2.17(c)) using the following relation:

$$-\langle A + B \rangle = \frac{3C}{2\mu_B} m_o \tag{2.17}$$

where C is again the same proportionality constant as previous two sum rules.

Using the aforementioned sum rules, one can calculate the spin and orbital moment for a specific element in a system with multiple constituent elements. XAS and XMCD will be utilized extensively to study the element specific magnetic properties of MPEAs which are presented in Chapter 4.

2.7 Small-Angle X-ray Scattering

While there are techniques which provide nm spatial resolution like Lorentz TEM, Magnetic Force Microscopy (MFM), and X-ray Photoemission Electron Microscopy (X-PEEM) their temporal resolution is limited to millisecond regime. Similarly, XMCD can be used to study the magnetic response of a sample with fs resolution but lacks any spatial information. There are very few techniques which are capable of studying the spatial and temporal response of materials with both nanometer and femtosecond resolution respectively. One such techniques capable of both nm spatial resolution and fs temporal resolution is called Small-angle x-ray scattering (SAXS) which can be measured in both transmission and reflection geometry. SAXS measurements are generally performed at a synchrotron or XFEL and it's magnetic sensitivity comes from measuring at M or L edge of a magnetic constituents in the sample. Fig. 2.18 shows schematic of a typical SAXS measurement in transmission geometry. The peak position (q_0) and peak width (Γ_0) in q dimension observed in SAXS represents the pe-

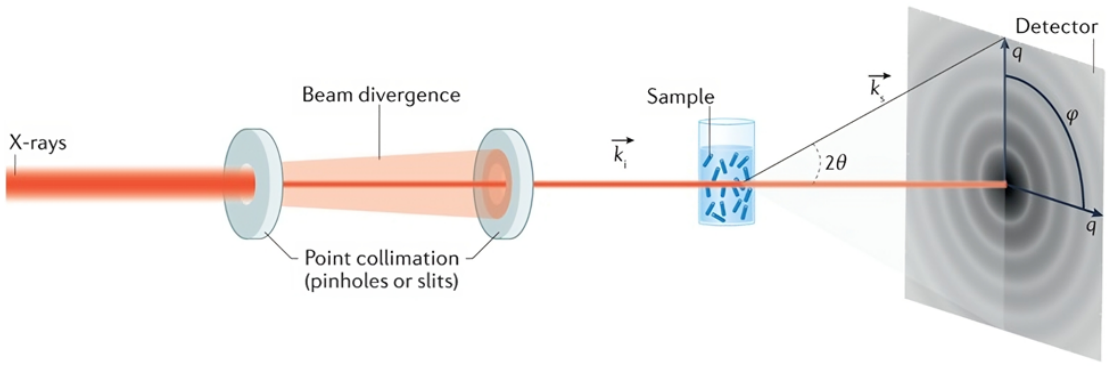

Figure 2.18: Schematic of small angle X-ray scattering in transmission geometry. An X-rays or neutron beam illuminates the sample and depending on the periodicity, correlation length and the symmetry of the sample, we obtain a diffraction pattern analogous to X-ray diffraction [84].

riodicity ($period = 2\pi/q_0$) and correlation length ($correlationlength = 2\pi/\Gamma_0$) respectively. Please note that unlike X-ray diffraction where the diffraction centers are individual atoms, in SAXS the mesoscopic symmetry/ordering of the sample acts like a diffraction grating and it is this effect that gives rise to the diffraction pattern observed on the detector.

Fig. 2.19 present SAXS results for CoO(10Å)[Co(4Å)/Pt(7Å)]$_4$ Co(6Å)CoO(10(Å)$_{10}$ system performed by Hellwig et al. [85]. These multilayered magnetic films experience Perpendicular Magnetic Anisotropy (PMA) which causes the magnetization in Co subsystem to lie perpendicular to the film plane. This PMA combined with high magnetostatic energy for uniformly magnetized state, causes the samples to break down in alternating up and down domains as shown in Fig. 2.19(a-b). The morphology of these magnetic domains depends on the sample's composition, history, and geometry [85]. There are two distinct magnetic domain morphologies, one is labyrinth domain state and the other is the aligned or stripe domain state (see Fig. 2.19(a-b)). Demagnetizing the sample with applied field out of film plane results in labyrinth state whereas demagnetizing with in-plane field causes

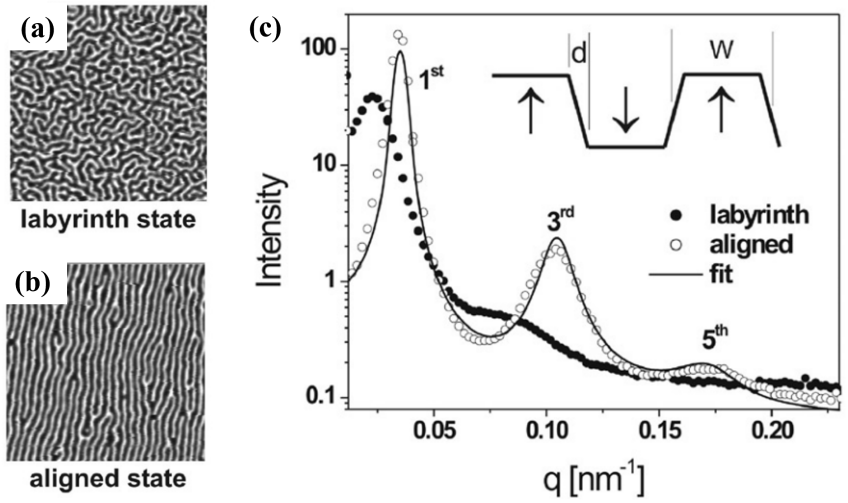

Figure 2.19: Figure shows on of the first resonant magnetic SAXS experiments performed by Hellwig et al. [85] on Co/Pt multilayer samples. The measurements were done in transmission geometry similar to the one shown in Fig. 2.18. **(a)** and **(b)** show the labyrinth and stripe domain morphologies respectively where the images are 5 µm in area. **(c)** shows the SAXS results from both morphologies up to the 5th order in the case of stripe domains (open symbols) and 3rd order for labyrnith domain (closed symbols).

the sample to form aligned or stripe domains. One dimensional SAXS results recorded with an apertured diode detector for both labyrinth (closed symbols) and stripe domains (open symbols) is shown in Fig. 2.19(c). For both morphologies, only odd order diffraction peaks are observed due to the equal width of up and down domains [85]. For labyrinth domains (period $\approx$ 130 nm and correlation length $\approx$ 360 nm) very broad 1st and 3rd order peaks are clearly visible due to the inherent disorder for this morphology. Whereas, for stripe domains (period $\approx$ 90 nm and correlation length $\approx$ 970 nm), sharp peaks are observed up to the 5th order. Solid line in the Fig. 2.19(c) is a fit for stripe domain structure shown in the inset of same figure.

To summarize, SAXS is a powerful technique which can be used to study mesoscopic periodicity present in magnetic or non magnetic samples. Furthermore, when these mea-

surements can be done with fs temporal resolution at an XFEL enabling both nm spatial resolution and fs temporal resolution. This is the primary technique used for results presented in Chapter 5 of this thesis.

2.8 X-ray Diffraction

X-ray diffraction is a photon-in-photon-out technique used to investigate the periodic structures present in materials. When incoming X-ray photons encounter the electron clouds of individual atomic planes in the material, they interfere constructively and destructively to generate a diffraction pattern. The positions of peaks observed on the detector depend on the crystal symmetry of the material. The peak positions in X-ray diffraction can be described using Bragg's law, which is expressed as:

$$n\lambda = 2d\sin\theta \tag{2.18}$$

Here, λ is the wavelength of the X-rays, θ is the angle of incidence, d is the interplanar spacing, and n is an integer. This law is based on the difference in path length of scattered light from different atomic planes (see Fig. 2.20(a)).

A more elegant way of describing when the Bragg condition is met is to use reciprocal space representation, which can be expressed as:

$$\begin{aligned}
\mathbf{a}^* &= 2\pi\frac{\mathbf{b}\times\mathbf{c}}{\mathbf{a}\cdot(\mathbf{b}\times\mathbf{c})} \\
\mathbf{b}^* &= 2\pi\frac{\mathbf{c}\times\mathbf{a}}{\mathbf{b}\cdot(\mathbf{c}\times\mathbf{a})} \\
\mathbf{c}^* &= 2\pi\frac{\mathbf{a}\times\mathbf{b}}{\mathbf{c}\cdot(\mathbf{a}\times\mathbf{b})}
\end{aligned} \tag{2.19}$$

Here, $\mathbf{a}, \mathbf{b}, \mathbf{c}$ are lattice vectors, and the denominator represents the unit cell volume.

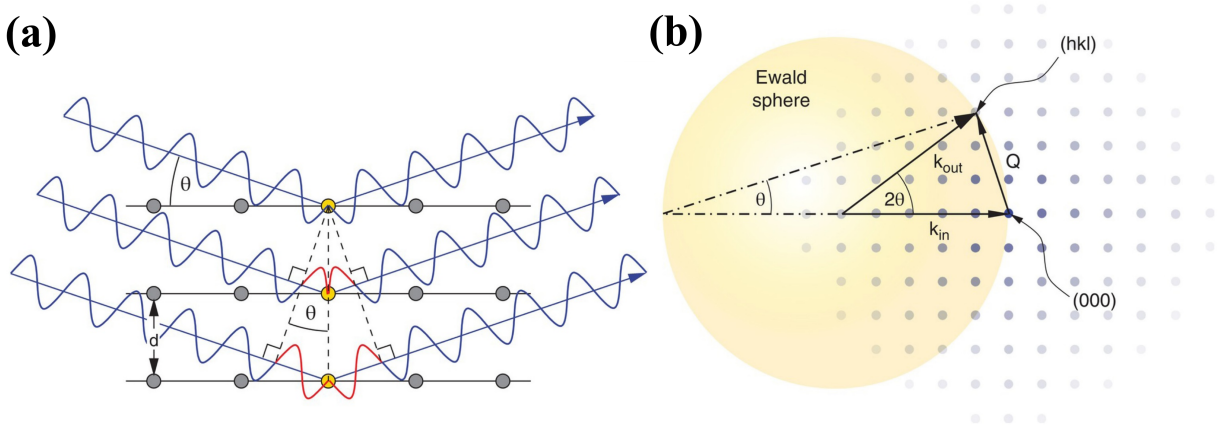

Figure 2.20: Figure **(a)** shows schematic with path difference between the scattered rays from successive atomic planes. **(b)** shows Ewald sphere construction.

The units of the reciprocal lattice vectors $(\mathbf{a}^*, \mathbf{b}^*, \mathbf{c}^*)$ are nm^{-1}. Each reciprocal lattice point corresponds to a set of crystallographic planes (as depicted in Fig. 2.20(b)). All the allowed diffraction peaks for a specific crystal orientation can be found by drawing the incident wavevector ($\mathbf{k_{in}} = 2\pi/\lambda$) at a reciprocal lattice point and enclosing it with a circle of radius $|\mathbf{k}|$ (Fig. 2.20(b)). The lattice points falling on the periphery of this circle represent the allowed diffraction peaks. It is important to note that the Ewald sphere shown in Fig. 1(b) is a two-dimensional representation of a three-dimensional sphere.

While Bragg's law and Ewald sphere construction elucidate the allowed diffractions, they do not fully account for the intensity of the scattered peaks. For a polycrystalline material, the integrated X-ray intensity is expressed as:

$$\mathbf{I}_{hkl} = k_I \frac{p_{hkl}}{v^2}(LPA)\lambda^3 F_{hkl}^2 \exp\left(-2M_t - 2M_s\right) \tag{2.20}$$

Here, k_I represents the instrument scaling factor, p_{hkl} is the multiplicity factor of a specific lattice plane (hkl), v is the volume of the unit cell, LPA encompasses the Lorentz-

polarization and absorption factors, λ denotes the X-ray wavelength, F_{hkl} corresponds to the structure factor, and $\exp(-2M_t - 2M_s)$ accounts for the attenuation factor caused by lattice thermal vibrations called thermal Debye-Waller (M_t) and weak static displacements/Athermal Debye-Waller (M_s) factor [86]. A comprehensive discussion on the aforementioned intensity equation can be found in He [86].

The M_s factor, which is linked to static displacements, is defined as follows:

$$M_s = B_s \left(\frac{\sin\theta}{\lambda} \right)^2 \tag{2.21}$$

where

$$B_s = 8\pi^2 \left\langle \mu_s^2 \right\rangle \tag{2.22}$$

and $\langle \mu_s^2 \rangle$ represents the mean square of the projection of atomic displacements on the lattice plane being probed. The key thing to note here is that it is the presence of this M_s factor that leads to a significant reduction in the scattered intensity for MPEA systems which will be discussed in the upcoming chapter. Consequently, X-ray diffraction measurements of MPEAs present challenges in interpreting the data due to broad peaks and low counts. To address this, proper alignment prior to measurements and a high photon flux are of paramount importance for MPEA XRD measurements.

2.9 Summary

In this chapter I introduced the basics of X-ray generation in synchrotrons and free electron lasers and their working principal as techniques reliant on them will be used throughout this thesis. Furthermore, basics of SAXS, XAS, XMCD, VSM, DC and AC susceptibility were introduced. To study MPEAs, XAS, XMCD, EDS, DC and AC susceptibility, aging

measurements were primarily used. Whereas, ultrafast domain dynamics for CoFe/Ni was studied using SAXS, MFM, and micro-magnetic simulations.

Chapter 3

Multi-principal element growth and characterization

In this chapter I will discuss the growth of MPEA thin films and their basic characterization. Both bulk and thin film samples were studied using EDS, TEM and XRD which will be discussed in this chapter. TEM measurements were performed by our collaborator Dr. Andrew Lange at Lawrence Livermore National Laboratory (LLNL) whereas the XRD and EDS measurements with SEM were performed at CNM2 in UC Davis.

3.1 Thin film growth

The bulk material used in this study was obtained from Element Materials Technology. The manufacturer specified the composition of the bulk material as $Fe_{39.8}Co_{19.92}Mn_{20.52}Cr_{14.77}Si_5$ (at %), using direct current plasma atomic emission spectrometry. To deposit thin films, a 2-inch diameter and 6 mm thick sputtering target was cut from the bulk material. Additionally, a small cylindrical sample with dimensions of 1.11 mm height and 3.16 mm diameter was prepared for bulk vibrating sample magnetometer (VSM) measurements.

Table 3.1: MPEA sample growth parameters table

		Deposition parameters			
Sample ID	Substrate	Power (W)	Substrate Temp (°C)	Ar pressure (mTorr)	Thickness (nm)
65nm Si	Si	100	27	2	65 ± 3
65nm SiN	SiN_x	100	27	2	65 ± 3
500nm Si	Si	100	27	2	500 ± 25
500nm SiN	SiN_x	100	27	2	500 ± 25

The FeCoMnCrSi thin films were grown using an AJA International sputtering system. Prior to the deposition, a 15-minute pre-sputtering process was applied to remove surface contaminants from the target. The measured approximate deposition rate was 0.65 Å/sec at 100 W of gun power and 2 mTorr Ar partial pressure, which corresponded to the removal of approximately 60 nm from the target surface in 15 minutes, almost an order of magnitude larger than the typical oxide layer (approximately 5-10 nm) on materials.

The thin films of MPEA were grown on two different substrates: Si (001) and SiN_x (polycrystalline) 100 nm thick membranes. The SiN_x 100 nm membrane samples were used for x-ray studies in transmission geometry. The substrates were diced to 3.9 × 4.1 mm size to minimize shape anisotropy effects in the samples. Prior to deposition, the samples were cleaned using acetone to remove the backing adhesive from the dicing step, followed by ultrasonic cleaning in isopropyl alcohol (IPA) bath to remove any fine debris. The two substrate types (Si and SiN_x) were co-deposited in the chamber to ensure identical and comparable compositions. The samples were grown at room temperature with a source power of 100 W and Ar partial pressure of 2 mTorr. The samples were not annealed after deposition to prevent recrystallization and phase separation. Table 3.1 provides the growth parameters for all four samples.

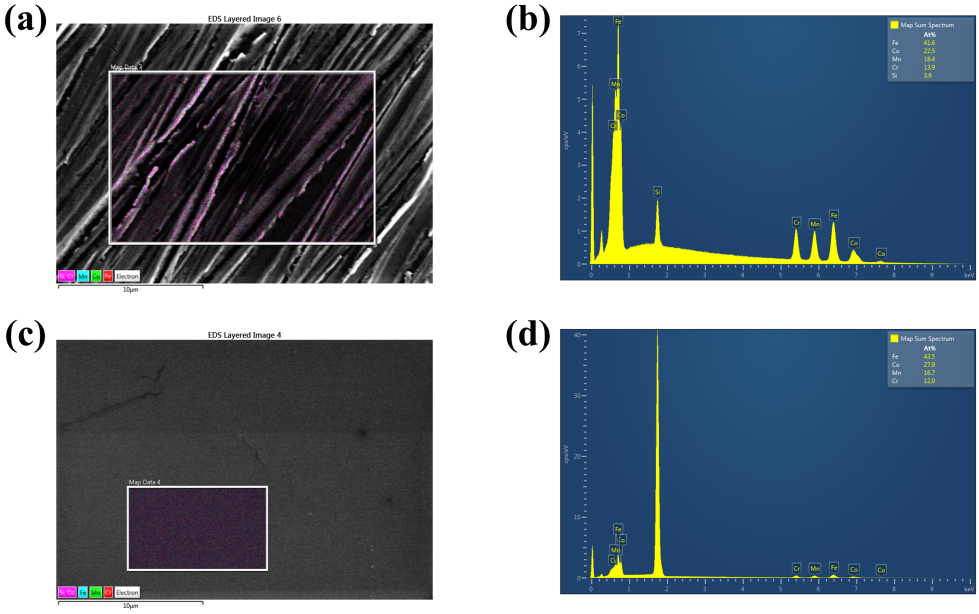

Figure 3.1: **(a)** and **(c)** present the superimposed Stacked Energy-Dispersive X-ray Spectroscopy (EDS) map onto Scanning Electron Micrographs for the elements Fe, Co, Cr, Mn, and Si, corresponding to the bulk and thin film samples, respectively. **(b)** and **(d)** exhibit the EDS spectra displaying the x-ray emission from the bulk and thin film samples, respectively, with the indexed $K\alpha_1$ and $K\alpha_2$ peaks indicated.

3.2 EDS measurements

Bulk sample and sputtered thin films were studied using EDS to ensure chemical homogeneity. Compositions of both bulk and thin film samples were confirmed by constructing 2D compositional maps using FEI Scios equipped with Oxford Instrument EDS system. Fig. 3.1(a) shows a composition map of the elements overlaid on top an SEM image for unpolished bulk sample of FeCoCrMnSi. Fig. 3.1(b) shows indexed EDS spectra from the sample with a rough estimate of the atomic % composition. The composition reported by EDS are qualitative in nature so it is not surprising that the EDS reported composition does not match the composition provided by the manufacturer. Fig. 3.2 shows the elemental maps

Table 3.2: Comparison of the Measured Compositions Using EDS with the Manufacturer's Quoted Bulk Composition, for Both Bulk and Thin Film Samples. It is important to mention that the reported composition for the 65 nm film grown on Si substrate assumes a 5 At.% Si content.

	Element At. %				
Sample ID	Fe	Co	Cr	Mn	Si
Bulk quoted	40	20	15	20	5
Bulk measured	42	22	14	18	4
65 nm film measured	41	26	12	16	5

Fe, Co, Cr, Mn and Si for the bulk unpolished sample with a step size of $\approx$ 500 nm. The elemental maps were measured at the emission lines specified at the top of elemental map. The dark lines observed in the map are scratches from the bulk sample surface. No segregation of elements was observed at the length-scales measured, ruling out phase separation or intermetallic formation. One thing to note here is that the sample could be inhomogeneous at different length scales: it may exhibit inhomogeneity at longer length-scales (e.g., 100s of µm's) or short-range ordering at the atomic scale. Therefore, the presented EDS results should be solely used to draw conclusions regarding intermetallic formation or clustering at the 500 nm to 20 µm length-scale. Fig. 3.1(c) shows a composite map in a small region of interest (white box) superimposed on an SEM image of the sample. Fig. 3.1(d) shows the EDS spectra along with an estimate of elemental composition. Within the margin of error ($\pm$ 5 %) the composition of the film is similar to the target. Measured composition for bulk and 65 nm film are tablulated and compared with the manufacturer quoted composition in Table 3.2. The large uncertainty in the reported composition is due to low acceleration voltage required for measuring thin films in order to ensure interaction of electron beam with the thin film. No compositional segregation was observed in the area of interest which is also evident from the element specific maps shown in Fig. 3.2.

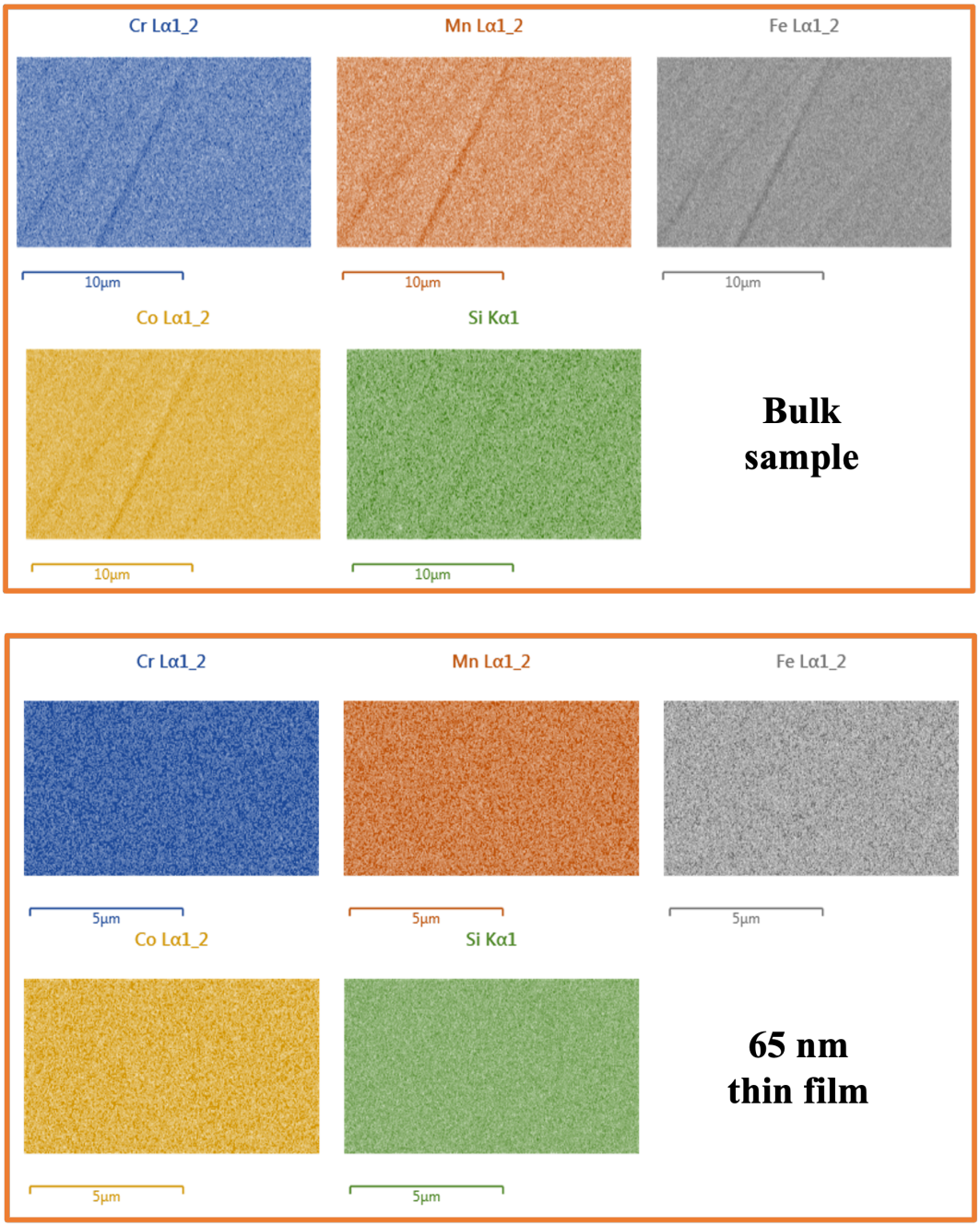

Figure 3.2: Element specific maps for Fe, Co, Cr, Mn and Si for bulk (top panel) and 65 nm thin film (bottom panel) sample of FeCoCrMnSi MPEA system.

3.3 TEM measurements

In order to further confirm the compositional homogeneity of the thin films EDS measurements were performed using TEM by our collaborator D. Andrew Lange at Lawrence Livermore National Laboratory (LLNL) with a resolution of 5 nm. TEM samples were milled out from 65 nm and 500 nm thin films using a focused ion beam. Prior to milling, the samples were coated with a thin layer of carbon followed by a platinum layer. Fig. 3.3 shows the aforementioned TEM maps for both 65 nm and 500 nm sample. No elemental segregation was observed for both 65 nm and 500 nm samples. The figures also show a High-Angle Annular Dark-Field (HAADF) image which shows that the both thin film samples have grain sizes on the order of µm size.

3.4 XRD measurements

It is well known that the unit cell of MPEAs is highly distorted due to the wide atomic size distribution of the constituent elements. This can lead to atoms being displaced from their nominal position in perfect crystal lattice by up to 0.25 Å[87]. This static displacements (M_s see Eq. (2.21)) lead to a huge loss in scattered intensity for MPEA systems. This makes the X-ray diffraction measurements of MPEAs very challenging to interpret due to broad peaks and low counts. To mitigate this, proper alignment prior to measurements and high photon flux are of paramount importance for MPEA XRD measurements. Following alignment and measurement steps were taken to boost SNR for XRD:

- The samples were first aligned to (004) Si substrate peak at $2\theta = 69$ degrees.
- In the second aliment step the samples were aligned to the MPEA peak at $2\theta = 47$ degrees.

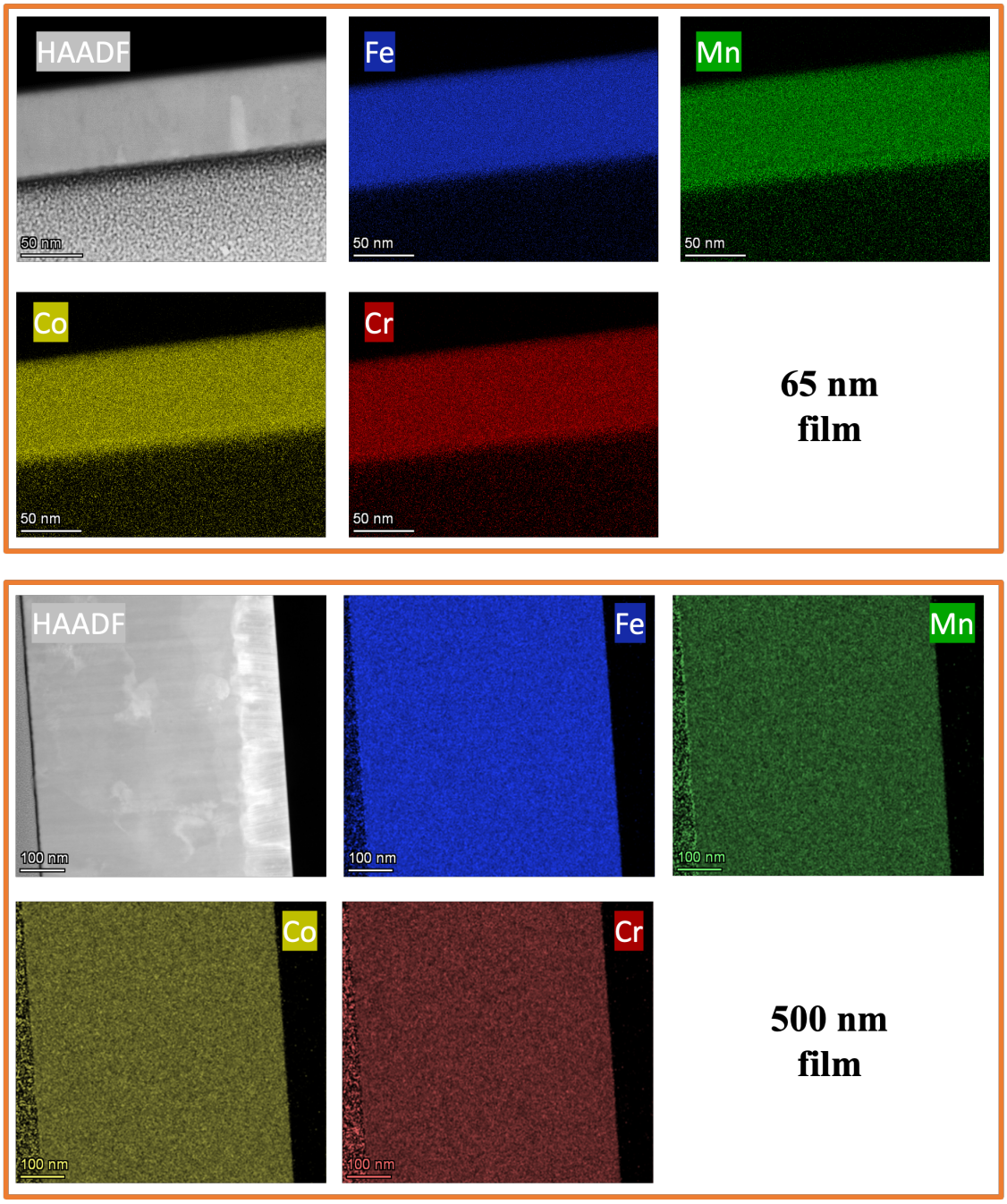

Figure 3.3: Element specific maps for Fe, Co, Cr, Mn and Si for 65 nm (top panel) and 500 nm (bottom panel) thin film sample of FeCoCrMnSi MPEA system.

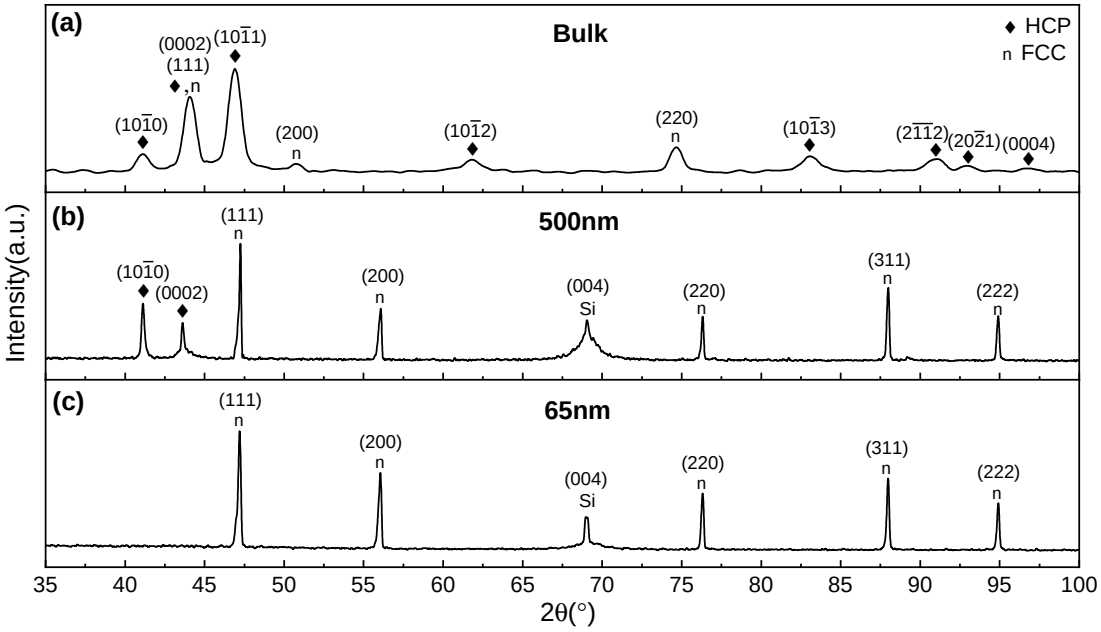

Figure 3.4: Figure shows indexed X-ray diffraction patterns for bulk **(a)**, 65 nm thin film **(b)** and 500 nm thin film **(c)** sample.

- At each 2θ step, diffracted signal was averaged for 1 second.

Crystal structure of bulk and as grown 65 nm and 500 nm thin films was characterized using Panalytical X'Pert PRO MRD with Cu X-ray source (λ = 1.5406 Å). Samples were aligned using X-ray peak observed near 47 degrees in 2θ. Both thin film samples were found to be polycrystalline in nature. Fig. 3.4 shows the X-ray diffraction (XRD) pattern collected for all three samples. For the bulk sample, both FCC and HCP phases were observed. FCC and HCP phases are labeled using square and diamond symbols, respectively. A lattice parameter of a = 3.584 Å ± 0.017 Å was obtained for FCC phase, while for HCP phase, the lattice parameters were calculated to be a 5 2.524 Å ± 0.007 Å and c = 4.123 Å ± 0.012 Å. For 500 nm thin film sample, both FCC and HCP phases were observed similar to the bulk sample, although a smaller amount of HCP was present as indicated by the lack of lower

intensity Bragg peaks. Additionally, the lattice parameter of the FCC phase was lower than that of the bulk phase, a = 3.486 Å ± 0.159 Å, and the lattice parameter of the HCP phase was found to be a = 2.537 Å ± 0.007 Å and c = 4.135 Å ± 0.012 Å. Surprisingly, even though the films are not grown epitaxially, the 65 nm thin film was found to be fully FCC, with a lattice parameter of a = 3.488 Å ± 0.157 Å, similar to the 500 nm thin film. Please note that the Si substrate peak for both 65 nm and 500 nm samples are low in intensity because X-rays were aligned using MPEA peak at ≈ 47 degrees. Furthermore, the error reported here is one σ (standard deviation) calculated from the list of lattice parameters from each indexed X-ray peak.

The XRD measurements shown in Fig. 3.4 clearly show that the relative amount of HCP and FCC phase depends upon the film thickness. For bulk and 500 nm thin film sample, both HCP and FCC phases are observed. The amount of HCP phase was lower for the thin film as indicated by lack of lower intensity HCP Bragg peaks. For 65 nm thin film, no HCP peaks were measured, indicating that only FCC phase is present. The EDS and TEM presented in previous sections indicate that both FCC and HCP phase have same composition. Presence of dual phases with identical composition is in agreement with recent studies by Li et al. [21] on a similar MPEA system, $Fe_{50}Co_{10}Mn_{30}Cr_{10}$. The aforementioned study showed that the partial martensitic transformation of FCC to HCP during quenching can lead to the formation of the dual phase alloy. Furthermore, it also showed that the relative amount of FCC and HCP phases were dependent upon the Mn content, where samples with 30 at.% Mn showed presence of both FCC and HCP phase, and samples with 40 and 45 at.% Mn were fully FCC. In comparison, we observe this variation in the stability of FCC and HCP phases as a function of thin film thickness. The precise mechanisms driving this stabilization of f.c.c phase, whether attributed to thin film confinement, heightened surface area-to-volume ratio, or substrate-induced interfacial effects, warrant further exploration

through both experimental and theoretical studies. Here we note that, the inclusion of silicon in the composition was found to not have an impact on the XRD pattern compared to literature, potentially due to low % Si content [21].

3.5 Conclusions

The characterization outlined in this chapter serves to verify the compositional uniformity of the MPEA system in both bulk and thin film geometries, with thin films demonstrating crystallinity even when grown at room temperature, as confirmed by XRD patterns. The observed crystallinity in thin films could potentially stem from entropy-driven stabilization effects; however, a more detailed investigation is necessary to substantiate this hypothesis. The XRD analysis reveals a notable impact of film thickness: thinner films promote the prevalence of the f.c.c phase over the h.c.p phase. The precise mechanisms driving this stabilization of f.c.c phase, warrants further exploration through both experimental and theoretical studies. In summary, these results showcases thin film growth's ability to tailor structural phases, notably influencing the relative proportions of f.c.c and h.c.p phases between bulk and thin film samples, with the 65 nm thin film exclusively exhibiting the f.c.c phase.

Chapter 4

Magnetic properties of MPEAs

In this chapter, I present a comprehensive overview of the macroscopic magnetic characterization conducted on the *FeCoMnCrSi* MPEA bulk and thin films samples characterized in Chapter 3. We utilized Versalab to study coercivity, temperature dependent magnetization and aging behavior of 65, 500 and bulk samples. Whereas, XMCD and XAS were utilized to study element-specific behavior. All XAS and XMCD measurements were done at bending magnet Beamline 6.3.1, at Advanced Light Source, Lawrence Berkeley National Laboratory. Part of this work was published in Jangid, Ainslie, and Kukreja [88].

4.1 Temperature dependence of Magnetization

As discussed in Section 2.3 ZFC and FC measurements give you information about types of magnetic phases present in a system along with the transition temperatures. Fig. 4.1 shows the zero field cooling (ZFC, green squares) and the field cooling (FC, red circles) response as a function of temperature for bulk, 500 nm and 65 nm thin film samples. The ZFC and FC curves were measured as described in Section 2.3 with an applied field of 25 Oe during heating. A remarkable increase of three orders of magnitude for magnetic moment

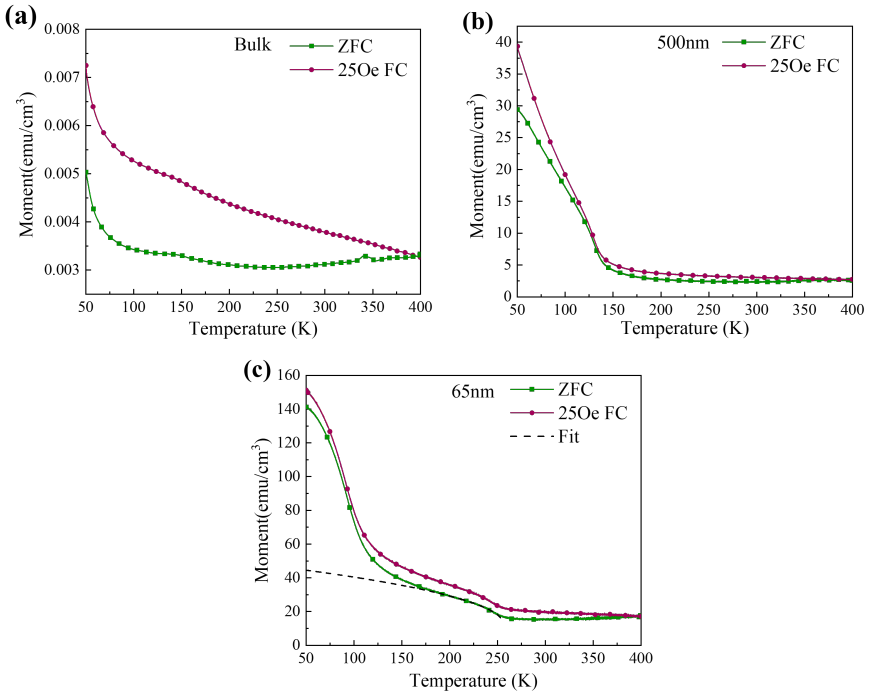

Figure 4.1: ZFC and FC curves for (a) bulk, (b) 500 nm film and (c) 65 nm film. The splitting in ZFC and FC at $T_S \approx 390$ K for all three samples. Further cooling results in a second magnetic transition at T_F of 145 K for bulk and 500 nm thin film, and 260 K for 65 nm thin film. Below T_F, FM or FM-like phase is observed in all three samples as discussed in text [88].

is observed between the bulk (M_{ZFC}= 0.005 emu/cm^3 at 50 K) and the 500 nm thin film (M_{ZFC}= 29.5 emu/cm^3 at 50 K). Further reduction of film thickness from 500 nm to 65 nm results in an additional order of magnitude increase of magnetic moment (M_{ZFC}= 141 emu/cm^3 at 50 K).

Multiple magnetic transitions as a function of temperature were also observed in all three samples as shown in Fig. 4.1. At 400 K, both M_{ZFC} and M_{FC} curves overlap with each other, however at T $\approx$ 390 K, a split between M_{ZFC} and M_{FC} is observed for all three samples. The split in M_{ZFC} and M_{FC} is indicative of magnetic transition of a frustrated system such as spin glass or a cluster glass [89]. This is because when a small field is applied after ZFC,

the moments are frozen in a frustrated state and for M_{ZFC} to reach the same value as M_{FC}, all frozen moments need to relax, which takes many decades in time. This leads to a split in ZFC vs FC curves. The experimental distinction between spin glass and cluster glass will be presented later in Section 4.2, but for now we will denote the transition temperature using T_S. Further cooling of the sample results in a small variation of the magnetization, and both ZFC and FC curves remain relatively flat till a second transition is observed, where both M_{ZFC} and M_{FC} rise rapidly. This increase in magnetic moment is observed in all three samples, albeit the transition temperature is different for each sample. A transition temperature, T_F, of 66 K, 145 K, and 260 K is measured for bulk, 500 nm and 65 nm thin film, respectively.

Following the second transition at T_F= 260 K, the ZFC magnetization for 65 nm thin film behaves as $M_{ZFC} = A(T_C - T)^{\beta}$, which is characteristic of a ferromagnetic (FM) phase. The fit (Fig. 4.1(c)) resulted in a $\beta = 0.57$ which is close to the classical Landau exponent of 0.5 for a ferromagnetic material, indicating that below 260 K the phase is FM or FM-like [15]. For bulk and 500 nm thin film samples, although an accurate fit could not be obtained due to full transition not being captured in the measured temperature range, hysteresis loop measurements discussed below point towards FM or FM-like phase. A third transition is also observed for 65 nm thin film at $T_U \approx 115$ K, the nature of which is not yet clear. Fig. 4.2 shows the magnetic field dependence of FC curves for all the samples. Similar behavior albeit higher magnetic moment is observed as applied field increases (from 25 Oe to 500 Oe). The higher applied magnetic field results in stronger Zeeman interaction thus aligning the spins further, as well as leads to smearing of sharpness of the magnetic transitions.

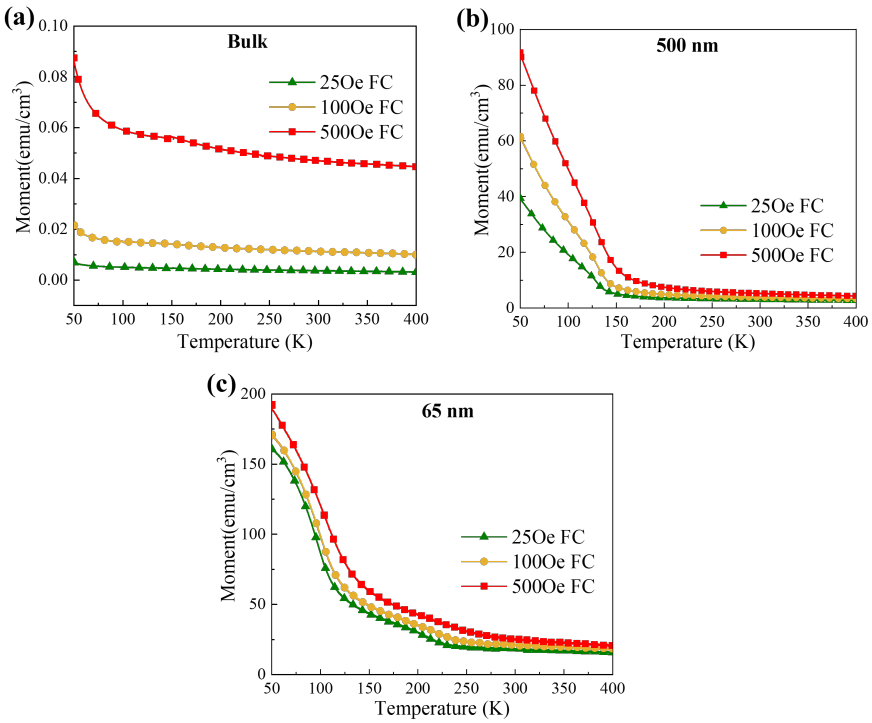

Figure 4.2: Field dependence of FC curves for (a) bulk, (b) 500 nm film and (c) 65 nm film. Magnetic moment is plotted as a function of temperature for an applied field of 25 Oe, 100 Oe and 500 Oe [88].

4.2 Temperature dependent hysteresis loops

Fig. 4.3 shows ZFC hysteresis loops for all the samples. ZFC hysteresis loops are measured after cooling the sample in no field. For bulk and 500 nm thin film, hysteresis loops were measured at (i) above T_S (400 K), (ii) in between T_S and T_F (200 K), and (iii) below T_F (50 K), while for the 65 nm thin film sample, hysteresis loops were measured at (i) above T_S (400 K), (ii) in between T_S and T_F (300 K), (iii) below T_F (200 K), and (iv) below T_U (50 K). For the bulk sample at 400 K, a linear response to the applied magnetic field is obtained. Additionally, even with an applied field of $\pm$30 kOe field, no saturation was observed, as shown in inset of Fig. 4.3(a). This combined with the ZFC and FC measurements (Fig. 4.1

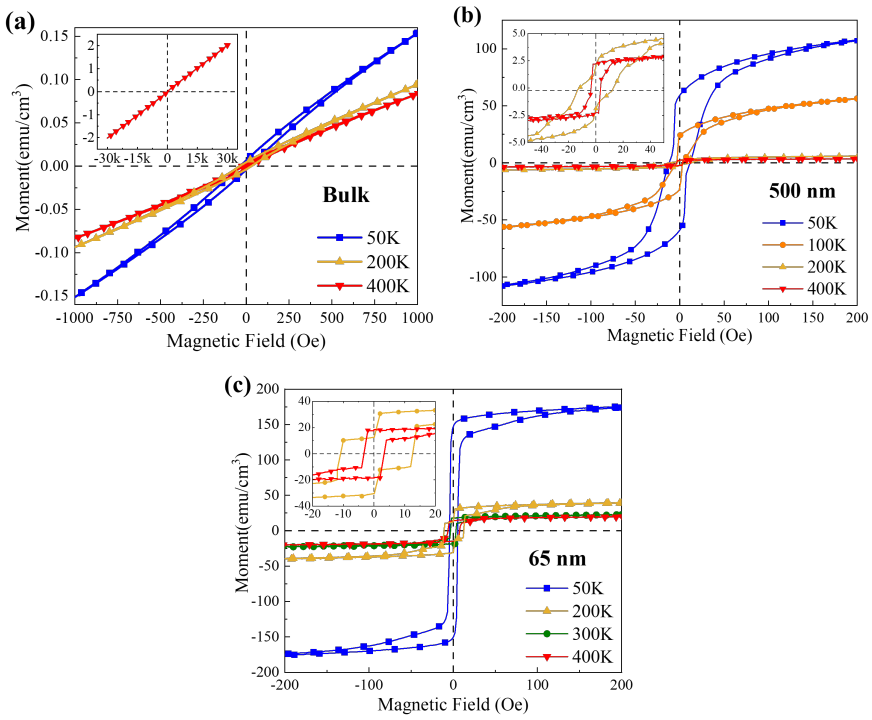

Figure 4.3: ZFC Hysteresis loops for (a) bulk, (b) 500 nm film and (c) 65 nm film. Inset for (a) shows the hysteresis loop for bulk sample at 400 K with an applied field of ±30 kOe. The y-axis represents moment in emu/cm3 and x-axis represents applied magnetic field in kOe. Inset for (b) and (c) show zoomed-in view of hysteresis loops for respective thin film samples. The y-axis denotes moment in emu/cm3 and x-axis denotes field in Oe [88].

and Fig. 4.2) alludes to paramagnetic behavior above T_S. In between T_S and T_F (200 K) as well as below T_F (50 K), hysteresis loops with a coercivity of 20 Oe are observed, indicating magnetic ordering in the sample. Specifically, at 50 K, a wider hysteresis loop with higher magnetic moment point towards FM behavior, in agreement with the ZFC and FC measurements.

For the thin film samples, a small hysteresis is observed at 400 K, as shown in inset of Fig. 4.3 (b) and (c). A coercivity (H_c) of 3 Oe and 5 Oe with a saturation magnetization (M_s) of 4 emu/cm^3 and 19 emu/cm^3 is obtained for 500 nm and 65 nm thin film, respec-

tively. The presence of small hysteresis with very low coercivity slightly above $T_S \approx 390$ K implies magnetic ordering as the transition temperature is approached, potentially due to the existence of small magnetic clusters before the spin glass or cluster glass phase emerges. Below T_S, hysteresis loop with higher coercivity is observed for both thin film samples. A coercivity of $H_c = 12$ Oe and 14 Oe is obtained for 500 nm and 65 nm thin film, respectively, while the saturation magnetization increases to 6.5 emu/cm^3 and 22 emu/cm^3 below T_S. The multiple steps observed in hysteresis loops clearly show the coexistence of two magnetic phases in both of the samples below T_S [90]. While the splitting of FC and ZFC curves in Fig. 4.1, indicates that one of the phases is spin glass or cluster glass, the nature of second magnetic phase is not clear and requires further characterization. Below T_F, no steps are observed in hysteresis loops and the saturation magnetization increases by two orders of magnitude for 500 nm film, while for 65 nm film, steps are still observed in hysteresis loops and the saturation magnetization doubles. For 65 nm thin film sample, below T_U, the steps finally disappear and saturation magnetization increases by an order of magnitude. The higher saturation magnetization and coercivity below T_F indicates the emergence of FM or FM-like phase, which is in agreement with ZFC and FC measurements.

In order to identify spin glass vs cluster glass phase below T_S, ZFC and FC hysteresis loops were measured. In magnetic MPEA systems, chemical clustering of the elements can lead to magnetic clustering and a magnetically disordered state named a cluster glass (or mictomagnetic state) can form. The clusters of different sizes can form and interact with each other, although within each cluster the FM spin alignment dominates. In zero field, these clusters can freeze with random orientations at low temperatures, resulting in low remanence and coercivity. On the other hand, cooling in applied field can collectively align these clusters, which results in larger remanence and shift in hysteresis loop in opposite direction of the field (similar to exchange bias effect) [15, 91]. Thus a cluster glass can be

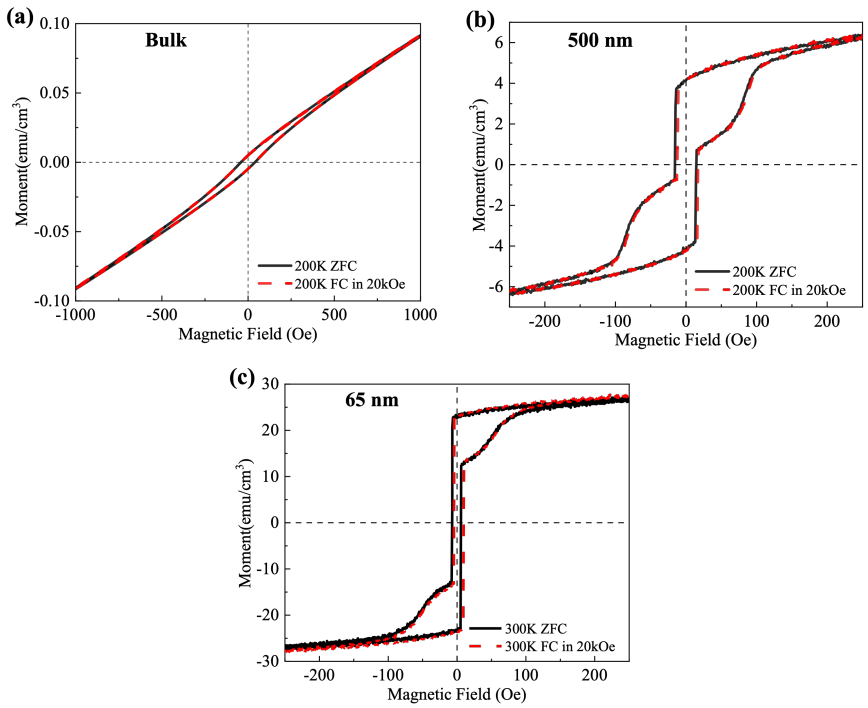

Figure 4.4: Field cooled and zero field cooled DC magnetization response with respect to field for Bulk, 500 nm and 65nm samples [88].

differentiated from spin glass by measuring ZFC and FC hysteresis loops. Fig. 4.4 compares the hysteresis loops measured after field cooling in 20 kOe with ZFC hysteresis loop for all three samples. No significant change in the hysteresis width or shift of the FC loop is observed in comparison to the ZFC loop. This combined with the fact that no chemical inhomogeneity was observed down to spatial length scales of 50 nm indicates that the sample does not show cluster glass behavior and eludes towards spin glass behavior below T_S. Here we note that the spin glass state has been recently observed in other MPEA systems such as equiatomic $CrMnFeCoNi$ and ternary $Cr_{23}Fe_4Ni_{73}$ alloy [14, 92].

4.3 Aging measurements

In order to further characterize the spin glass phase, we measured the aging behavior, i.e. time dependence of the magnetization within the frozen spin glass state. Magnetization of a spin glass evolves as a function of time to any change of external field in the frozen state. This aging behavior due to long-time relaxation effects highlights the dynamic nature of spin glasses [89]. Aging behavior was measured by cooling the sample in zero field to a desired temperature (temperature quench), waiting for a certain amount of time = t_{age}, and then applying a small field as described in detail in Section 2.3.2. Once the field is applied, the magnetization was measured as a function of time (M(t)) for different aging times, t_{age}. Fig. 4.5(a) and (c) shows the evolution of magnetization (normalized by applied field) as a function of time for 65 nm and 500 nm thin film below T_S, respectively. For both samples, M(t) increases, then goes through an inflection point, and is strongly dependent on t_{age}. The dependence on aging time is due to the aging processes occurring in the spin glass as a function of time. These aging processes are reflected in the different time dependencies of M(t) for a particular value of t_{age}. Fig. 4.5(b) and (d) show the relaxation rate $S(t) = (1/H)dM/d\log(t)$. The inflection point of M(t) corresponds to a maximum in $S(t)$, which shifts to longer measurements time, t, with increasing wait time, t_{age}. The presence of peak in $S(t)$ has been associated with the crossover from quasi-equilibrium dynamics (due to relaxation processes) to non-equilibrium dynamics (due to domain wall motion) and is found to be dependent upon the wait time, under the droplet model description of the spin glasses. More details on the droplet model of spin glasses can be found in Mydosh [93], but here we emphasize that the presence of aging behavior shows that magnetic phase occurring below T_S is indeed the spin glass phase.

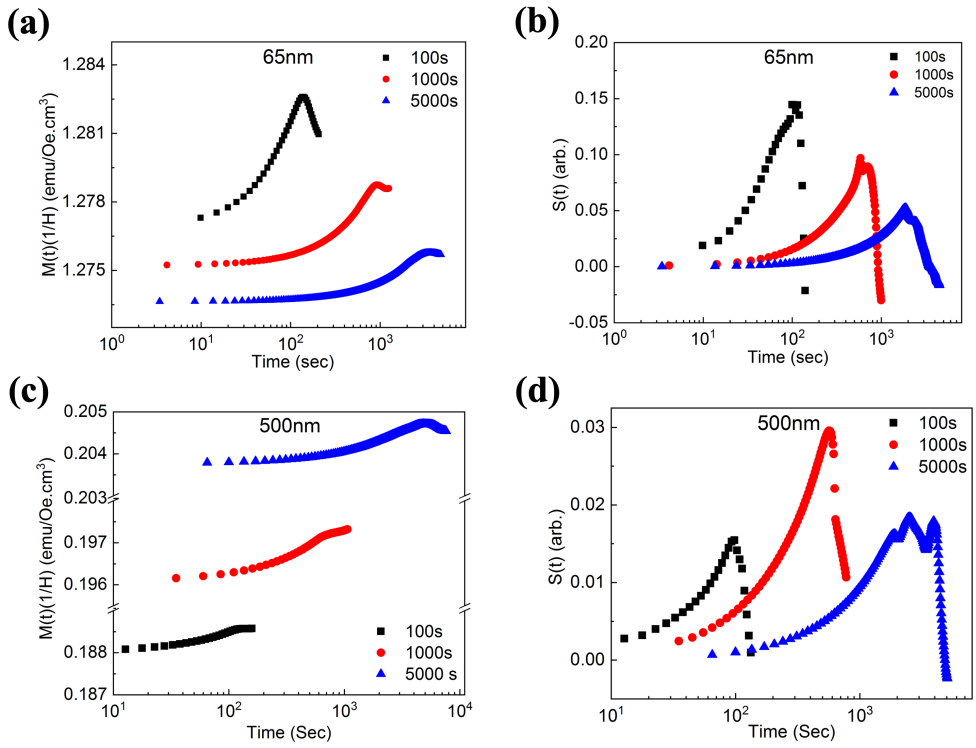

Figure 4.5: ZFC susceptibility $(1/H)M(t)$ and corresponding relaxation rates S(t) at wait times of 100, 1000 and 5000 sec at 300 K for 65nm sample and 200 K for 500nm sample [88].

4.4 Discussion of bulk measurements

Temperature dependence of total magnetic moment in the range of 400 K to 50 K reveal multiple magnetic transitions as shown by Figs. 4.1 and 4.2 for all three samples. For bulk sample, a paramagnetic phase is clearly observed at 400 K, noted by the linear dependence of magnetic moment on field and lack of saturation even at ±30 kOe (inset Fig. 4.3(a)). For the thin film samples, small hysteresis is observed at 400 K with coercivity in range of 3-5 Oe, potentially due to presence of local magnetic ordering within a paramagnetic matrix as the first magnetic transition is approached. At $T_S \approx 390$ K, first magnetic transition is observed with transformation to the spin glass phase as shown by the splitting of ZFC

and FC curves in Fig. 4.1 and aging behavior discussed in Fig. 4.5. Further lowering the temperature of this spin glass state results in a coexistence of two magnetic phases in thin film samples, as shown by the steps in hysteresis loop. The steps in the hysteresis loops can occur due to competing interaction between the spin glass phase and second magnetic phase with different coercivity. Such complex behavior in hysteresis loops has been observed in Ni with 21 at. % Mn due to presence of both spin glass and ferromagnetic ordering [94, 95].

A second magnetic transition associated with a sharp rise of total magnetic moment is observed for all three samples as the temperature is further decreased, as shown in Figs. 4.1 and 4.2. The coercivity and saturation magnetization also increases below T_F for all samples (Fig. 4.3), although the increase observed in thin films is significantly higher than the bulk sample. This behavior is indicative of FM ordering or at least a partial FM ordering of the local magnetic moments in the sample. The temperature of this second transition is dependent on the film thickness, where T_F = 260 K is observed for 65 nm thin flm and T_F = 145 K is observed for 500 nm thin film. For the bulk sample the transition temperature is even lower, with T_F = 66 K. These observations clearly show that the 2D confinement stabilizes the ferromagnetic phase, thus leading to higher transition temperature, coercivity and saturation magnetization. Furthermore, the total magnetic moment at 50 K for ZFC is four orders of magnitude higher for the 65 nm thin film than the bulk sample. Here we note that, this sequence of paramagnetic to spin glass to ferromagnetic phase transition with lowering of temperature is similar to magnetic transitions observed in a recent study on bulk equiatomic *CoCrFeMnNi* MPEA alloy [14]. Although the transition temperatures observed in our studies are comparatively higher, potentially due to larger amount of Fe present in the MPEA as well as due to the stabilization of magnetic ordering in thin films.

4.5 Element specific magnetization studies

In order to study the element specific magnetization, XAS and XMCD measurements were done around to $L_{2,3}$ edges for Fe, Co and Cr elements, which correspond to $2p_{1/2} \rightarrow 3d$ (L_2) and $2p_{3/2} \rightarrow 3d$ (L_3) transitions. All XAS and XMCD measurements were performed at bending magnet Beamline 6.3.1, at Advanced Light Source, Lawrence Berkeley National Laboratory during heating with 60 % circularly polarized x-rays of negative helicity and by switching the applied magnetic field between ±5000 Oe (±0.5 Tesla). Fig. 4.6 shows XAS measurement of 65 nm film done at 12 K for Fe, Co, Cr and Mn in transmission geometry post normalization and non-resonant background subtraction. A sum of two error functions was used to subtract the non resonant background from XAS at $L_{2,3}$ edge . No fine structure was observed around the two edges, indicating the metallic nature of the films. Please note that the XAS results presented in Fig. 4.6 are intensity average of XAS from magnetization parallel ($I^{\uparrow\uparrow}$) and antiparallel ($I^{\uparrow\downarrow}$) to the k of circularly polarized x-rays ($I_{XAS} = \frac{I^{\uparrow\downarrow}+I^{\uparrow\uparrow}}{2}$).

Fig. 4.7(a-c) shows XMCD ($I_{XMCD} = I^{\uparrow\downarrow} - I^{\uparrow\uparrow}$) results for 65 nm thin film measured in transmission geometry at various temperatures. XMCD spectra shows that the dicrhoic effect at $L_{2,3}$ edge for Fe and Co decreases as the temperature is increased and persists even up to 400 K although the signal is small. For Cr, XMCD signal decreases from 12 K to 200 K, above which no XMCD signal was observed. Fig. 4.7(d-e) shows XMCD measured in electron yield geometry as a function of temperature for 500 nm thin film. Electron yield mode was used due to the large thickness of 500 nm film leading to very low transmission of x-rays resulting in poor signal to noise. The XMCD signal for 500 nm shows similar temperature dependent behavior as 65 nm film where the signal decreases with increasing temperature for Fe and Co whereas Cr no XMCD signal was observed above 200 K. Please note that Mn has not been included in the XMCD results as it did not show any long range ferromagnetic ordering in the measured temperature range of 12 to 400 K, resulting in no

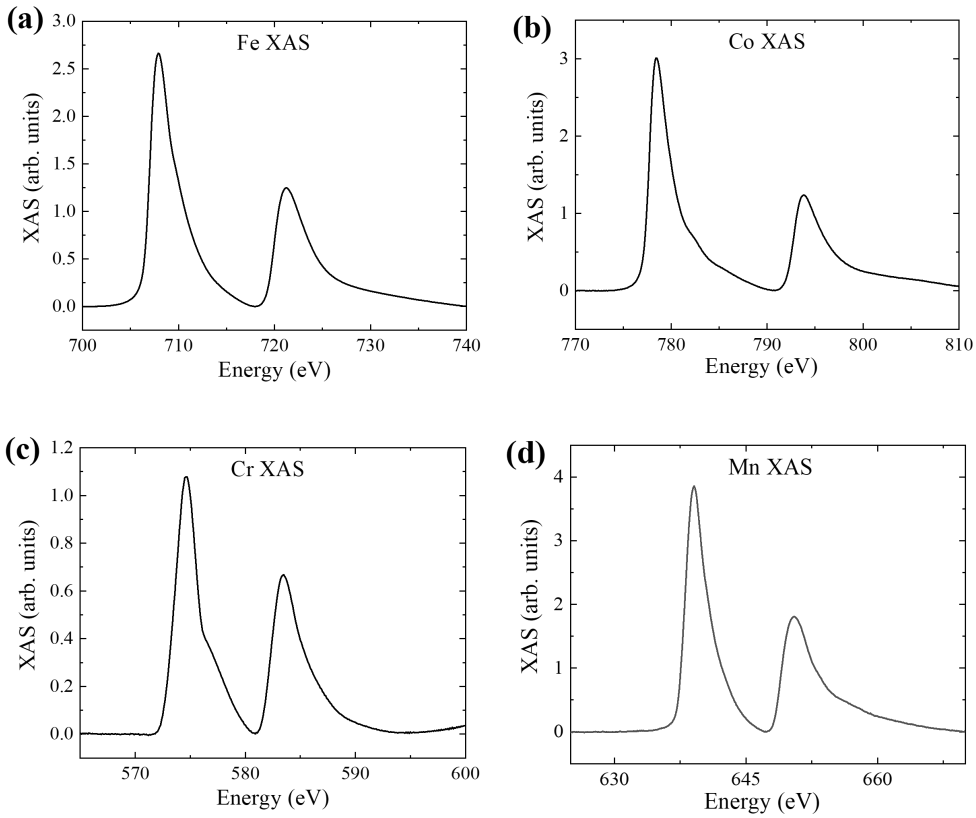

Figure 4.6: Representative XAS for 65 nm thin film after background subtraction measured in transmission geometry at 12 K for Fe, Co, Cr and Mn.

XMCD signal. This could be due to the fact that Mn is antiferromagnetic in nature, which would not be surprising as in pure metallic form it is antiferromagnetic in nature below $\approx$ 100 K as has been reported by Boakye and Adanu [96]. These results indicate that Fe, Co and Cr are ferromagnetic in nature whereas Mn might be antiferromagnetically ordered.

For both 65 nm and 500 nm samples the observed XMCD for Cr was much weaker and had opposite sign when compared to Fe and Co, which indicates that Cr is antiferromagnetically coupled with Fe and Co. Furthermore, the presence of XMCD signal for Fe and Co at 400 K indicates that ferromagnetic ordering temperature for these elements is higher than 400

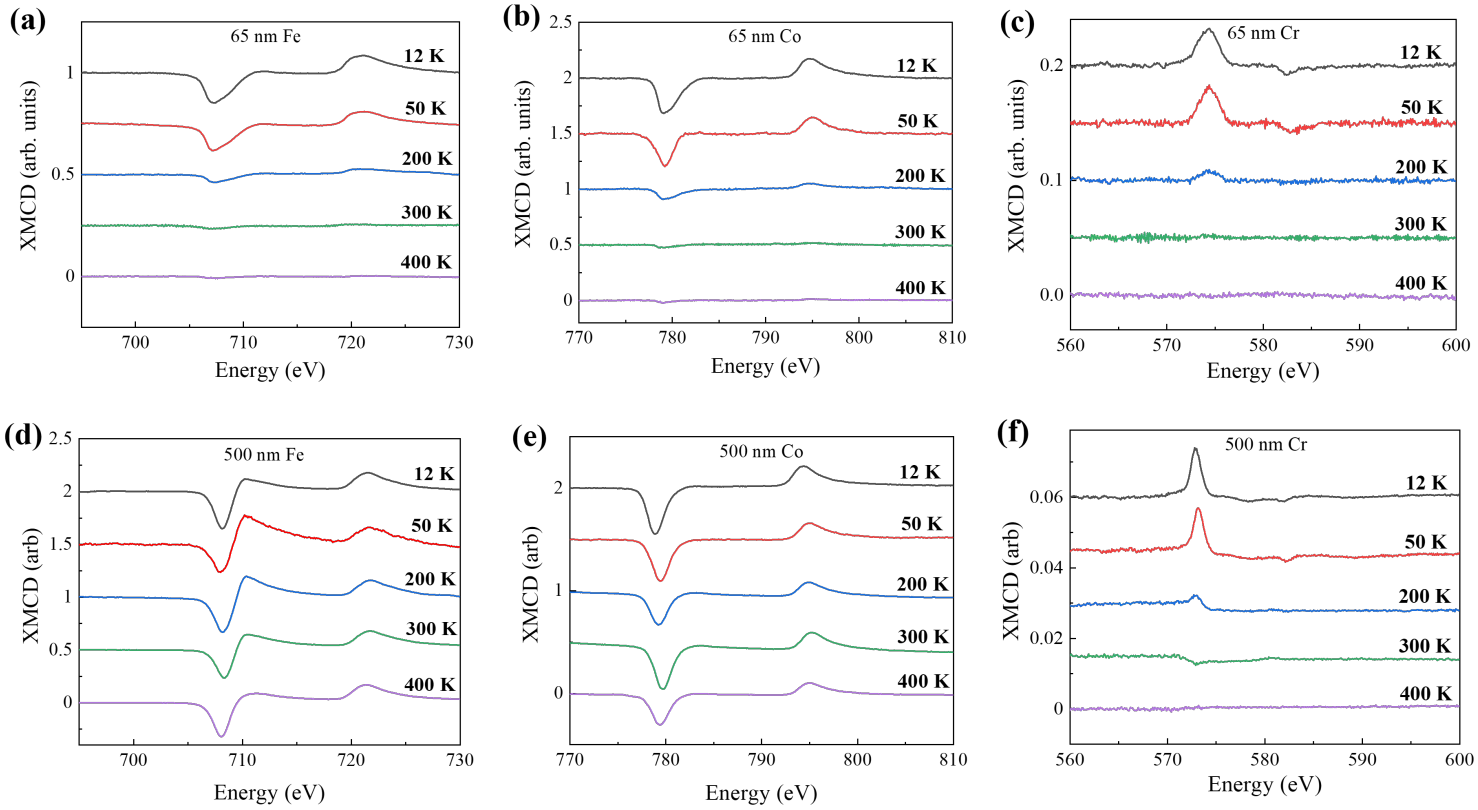

Figure 4.7: XMCD results for 65 and 500 nm thin film measured in transmission geometry at temperature ranging from 12 K to 400 K.

K. On the other hand ferromagnetic ordering temperature for Cr is between 200 K and 300 K above which it is likely in a paramagnetic state.

4.6 Spin and Orbital moment

As discussed in Section 2.6.1 XMCD spectra can be used to calculate the average spin and orbital moment per atom by applying the *sum rules*. Following number of *3d* holes (N_h) were used in calculating the moments: Fe = 3.5, Co = 2.5 and Cr = 5.0 [83]. Furthermore, as the samples are polycrystalline in nature, the XAS intensity was assumed to be orientation-averaged. In order to take into account the grazing incidence geometry of the measurement step, the moment has been scaled by a factor of $1/\cos(\pi/4)$ as the sample was tilted at 45 degrees to get a component of net in plane magnetization parallel to k vector of x-rays. Fig. 4.8 shows the calculated spin and orbital magnetic moment for Fe, Co and Cr for 65 nm (Fig. 4.8(a-c)) and 500 nm (Fig. 4.8(d-f)) thick MPEA film in temperature range of 12 to 400 K. This data is also tabulated in Table 4.1. The error bars reported here are one standard deviation (σ) calculate from eight XMCD scans.

Table 4.1: Tabulated spin moment (m_{spin}) in units of μ_B for Fe, Co, and Cr calculated using XMCD *sum rules* for 65 nm and 500 nm sample in the temperature range of 12 K to 400 K.

Temp (K)	65 nm thin film			500 nm thin film		
	Fe	Co	Cr	Fe	Co	Cr
12	1.36 ± 0.09	0.56 ± 0.06	0.50 ± 0.04	0.36 ± 0.08	0.17 ± 0.13	0.08 ± 0.01
50	1.30 ± 0.10	0.36 ± 0.08	0.47 ± 0.1	0.25 ± 0.03	0.10 ± 0.03	0.08 ± 0.01
200	0.48 ± 0.03	0.21 ± 0.02	0.24 ± 0.06	0.12 ± 0.04	0.15 ± 0.01	0.02 ± 0.01
300	0.27 ± 0.04	0.15 ± 0.04	0.00 ± 0.00	0.06 ± 0.02	0.09 ± 0.08	0.00 ± 0.00
400	0.14 ± 0.01	0.08 ± 0.01	0.00 ± 0.00	0.06 ± 0.03	0.13 ± 0.05	0.00 ± 0.00

The first key observation is an order of magnitude lower value for orbital moment compared to spin for both samples. This is due to metallic bonding and spin-orbit coupling which leads to quenching of orbital magnetic moment. The highest m_{spin} of 1.36±0.09 μ_B

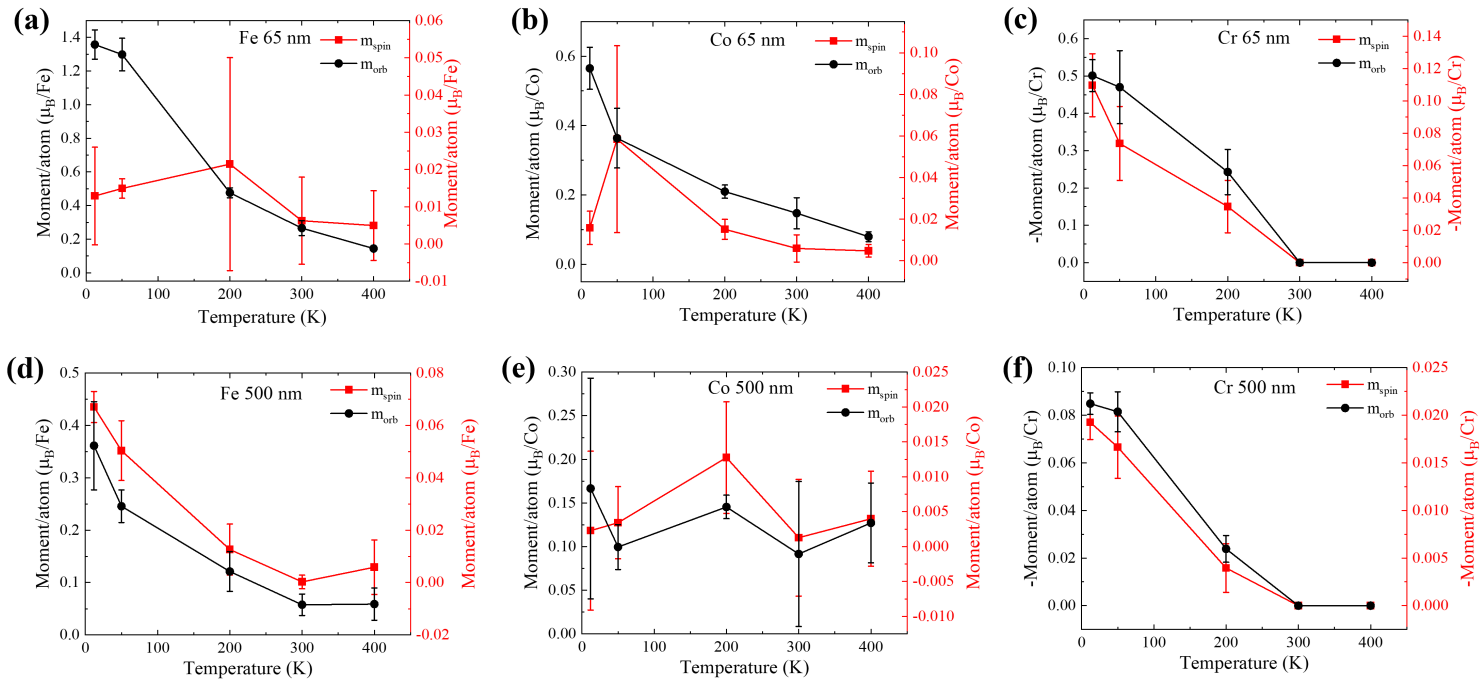

Figure 4.8: Spin (m_{spin} black curve and points) on left axis and orbital (m_{orb} red curve and points) moment on right axis for Fe, Co and Cr for 65 and 500 nm film calculated using XMCD *sum rules*. Please note the one order of magnitude lower value for orbital moment which is caused by spin-orbit coupling.

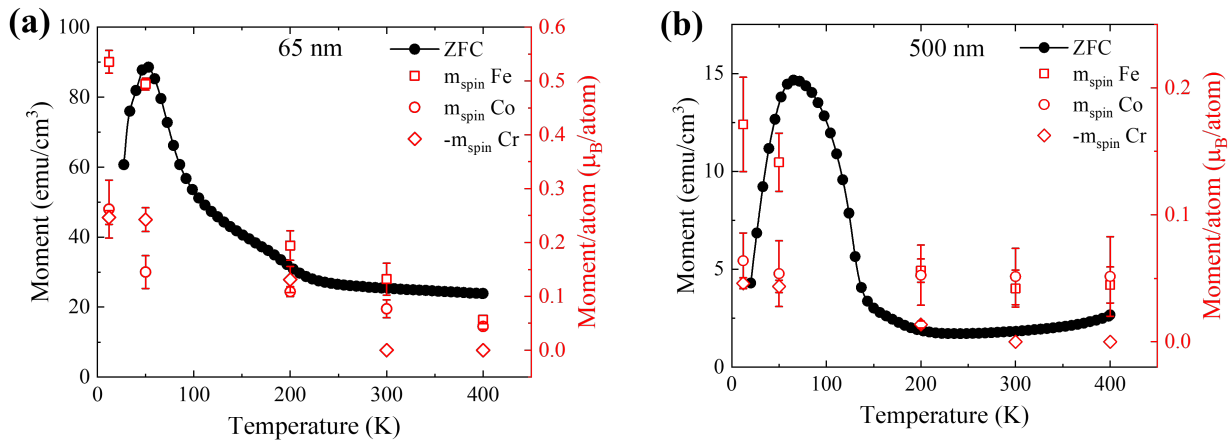

Figure 4.9: ZFC vs m_{spin} for 65 nm **(a)** and 500 nm **(b)** MPEA thin films. Please note that the sign for moment values of Cr has been scaled by a factor of -1.

(for 12 K) was observed for iron in 65 nm film (see Table 4.1). Whereas Co and Cr had approximately three times less moment for 65 nm film. Whereas, 500 nm film, similar to 65 nm film, the Fe moment is the highest of three constituent elements at 0.36±0.08 μ_B for 12 K. This is four times less compared to the moment observed for 65 nm film. Co and Cr show a very small moment of 0.17±0.13 μ_B and 0.08±0.01 μ_B respectively at 12 K for 500 nm film.

4.7 Discussion of element specific magnetic properties

Fig. 4.9 compares the calculated elemental spin moments (m_{spin}) with ZFC curves for both 65 nm and 500 nm films. The comparison hints to Fe being the main contributor for the bulk magnetization of both samples. Furthermore, the transition observed between 200 and 300 K for 65 nm film seems to be caused by paramagnetic to ferromagnetic transition of Cr. Whereas, the large jump in magnetization seen for 65 nm and 500 nm sample around 100 K and 150 K respectively is coincident with large increase in m_{spin} for Fe. The huge disparity

between the moments for 65 nm and 500 nm film (seen in Fig. 4.8) could be due to h.c.p phase having strong magnetic anisotropy compared to f.c.c phase which would cause the moments to be pinned and not respond to the applied external field during XMCD measurements. It can be speculated that because f.c.c phase is the primary phase in 65 nm film, it has higher moment compared to the 500 nm film which comprises of both f.c.c and h.c.p phases with phase boundaries pining the moments leading to a lower moment per atom for the system as a whole. Further studies on MPEA films grown on (111) oriented Si or MgO substrates are required to isolate h.c.p phase response.

Table 4.2: Comparison of spin moment of Fe, Co and Cr for both 65 nm and 500 nm film with values reported in literature for bulk single element [83].

Element	m_{spin} 65 nm	m_{spin} 500 nm	m_{spin} pure element
Fe	1.36 ± 0.09	0.36 ± 0.08	2.2
Co	0.56 ± 0.06	0.17 ± 0.13	1.57
Cr	0.50 ± 0.04	0.08 ± 0.01	0.5

Table 4.2 compares the m_{spin} for Fe, Co and Cr measured at 12 K with literature for magnetic moment for individual elements in their pure bulk form. It is evident that the measured moment values for both MPEA films are significantly lower compared to the values reported for pure Fe, Co and Cr samples. Several potential factors could underlie this phenomenon:

- *Modified Exchange Energy*: The m_{spin} of an element can be influenced by alterations in its density of states (DOS) for majority and minority spins, driven by changes in the exchange energy. Exchange energy, in turn, hinges on the local atomic environment. Given the distinctive atomic neighborhoods in MPEAs compared to pure metals, the exchange interaction is likely to differ, influencing the m_{spin} values.

- *Number of 3d Holes*: It has been reported recently that the number of 3d holes is potentially modified in MPEAs due to the unique neighborhood around the atoms compared to bulk. An increase in the number of 3d holes has been reported for Fe whereas a decrease has been reported for Co in Mn-rich single-phase fcc CrMnFeCoNi based MPEA [87]. Consequently, the assumed number of holes used in the previous section to calculate spin and orbital moment might not be accurate as these number of holes are for pure bulk metals.

Please note that the two aforementioned effects could also be related to each other. Further systematic spectroscopy measurements are required to elucidate the reason for observed lower moment in MPEAs compared to pure bulk metallic samples.

4.8 Conclusion

In summary, we compared the magnetic properties of both bulk and thin films of non equiatomic composition of *FeCoMnCrSi* based MPEA. Our studies show that thin film confinement can be utilized to manipulate the magnetic behavior of MPEAs. The measurement of magnetic behavior showed four orders of magnitude increase in saturation magnetization going from bulk to thin film. In all samples, two magnetic transitions were identified, (i) a paramagnetic to spin glass transition with a transition temperature of 390 K, and (ii) spin glass to ferromagnetic (or ferromagnetic-like) phase transition with a transition temperature of 66 K, 145 K and 250 K for bulk, 500 nm and 65 nm thin film samples, respectively. Furthermore, by controlling the film thickness, we were able to tune the saturation magnetization and coercivity of the ferromagnetic phase. XMCD studies show that Fe and Co are ferromagnetic in nature throughout the measured temperature range of 12 K to 400 K whereas Cr undergoes a paramagnetic to ferromagnetic transition between 200 K to 300 K

for both 65 nm and 500 nm film. Furthermore, Fe and Co are ferromagnetically coupled whereas Cr is antiferromagnetically coupled to Fe and Co. Mn was found to have no long range ferromagnetic ordering in the measured temperature range. The large increase in magnetization observed starting at approximately 125 K and 150 K for 65 nm and 500 nm film coincides with a large increase in magnetic moment of Fe indicating that Fe could be responsible for this transition. These results highlight the complex evolution of magnetism as a function of temperature in MPEA systems. They provide a starting point towards manipulating structural phases and magnetic properties via thin film control in MPEA, which could enable innovative alloy designs for a wider variety of applications including soft magnetic materials, rare-earth-free permanent magnets and magnetocaloric devices.

Chapter 5

Ultrafast response of CoFe/Ni hetrostructures

In this chapter, I present our study of ultrafast modification of mesoscopic magnetic textures. We tested the recent theoretical prediction by Baláž et al. [51] that extremely fast domain wall speeds of $\approx$ 14 km/s in ferromagnets can be achieved via optical pumping due to superdiffusive spin currents [39]. This is a remarkable prediction as it exceeds the generally accepted maximum speed for ferromagnets of $\approx$100 m/s for domain walls. Domain walls, which can be considered as bound magnetic solitons (localized nonlinear excitations with finite energy) [61], undergo Walker-breakdown above these speeds and the soliton-like structure of a domain wall becomes unstable [62, 63]. This would imply that ultrafast spin dynamics not only result in an overall demagnetization but can also affect the long-range spatial structure of magnetic domains over several tens of nanometers.

We conducted optical pump, EUV (extreme ultraviolet) magnetic scattering probe experiments with a mixed-state domain pattern that consists of domains of both labyrinthine and stripe-like character. Scattering from such samples yields two dominant diffraction com-

ponents; an azimuthally uniform and a twin-lobed ring pattern [66]. We employed 2D fits similar to those in [66] to isolate and study the magnetization dynamics of domains of differing character. We measured the pump fluence dependence over an order of magnitude. Given that domain walls typically exhibit both inertia [97, 98] and an activation energy barrier, i.e. pinning [63, 99], the fluence dependence for the ultrafast distortion should be different from that of demagnetization if the ultrafast distortion is the result of domain-wall motion. We employed micromagnetic simulations to test the hypothesis that the preferential motion of curved domain walls in labyrinthine domains are in fact the source of ultrafast distortions. Our results provide experimental evidence for the theoretical proposition that far-from-equilibrium conditions can give rise to extreme domain-wall speeds.

5.1 SAXS measurement geometry

Magnetic resonant small-angle x-ray scattering was measured by tuning the EUV photon energy to the M_3 edge of Ni at 66.2 eV at the FERMI free electron laser. Magnetic multilayered sample with stack layering of (Ta(3 nm)/Cu(5 nm)/[$Co_{90}Fe_{10}$(0.25 nm) /Ni(1.35 nm)] $\times$ 8 /$Co_{90}Fe_{10}$(0.25 nm)/Cu(5 nm)/Ta(3 nm)) were used. Ta seed layer was used for good adhision with substrate, whereas 5 nm of Cu was used as seed for growing CoFe/Ni heterostructure. This perticular composition was chosen for the study due to its ability to support both labyrinthine and stripe domain morphologies. The sample was grown using magnetron sputtering on 100 nm thick polycrystalline Si membranes with a total magnetic thickness of 13 nm and total film thickness of 27 nanometers. Magnetic force microscopy (MFM) studies prior to the experiment showed the presence of linearly oriented labyrinth domains with an average width of 110 nm. 50 fs resolution pump-probe measurements were performed with an 800 nm pump and a linearly polarized EUV probe in transmission mode. The schematic of time-resolved magnetic scattering setup is shown in Fig. 5.1 along with

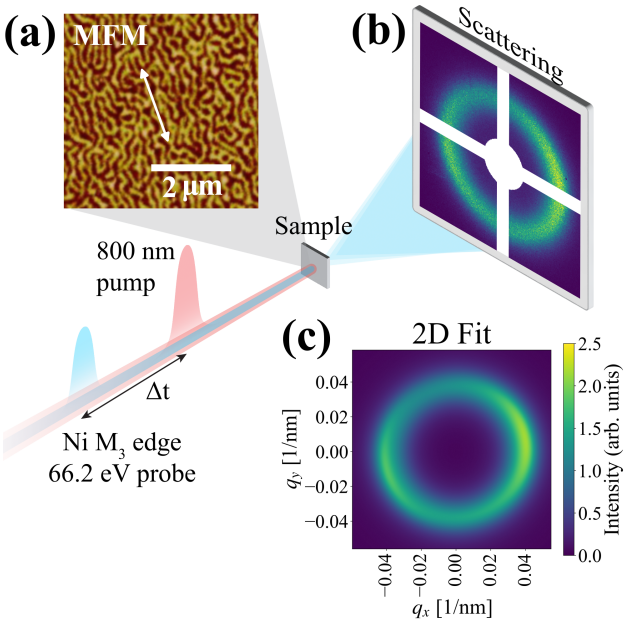

Figure 5.1: **Schematic of the optical pump EUV magnetic scattering probe setup.** Time-resolved studies were performed using 800 nm pump and 66.2 eV (Ni M_3 edge) probe. **(a)** MFM image ($\approx$ 5 µm $\times$ 5 µm FOV) of the sample. The white arrow highlights the direction of the linear texture of the domain pattern. **(b)** Magnetic diffraction pattern from the sample on the CCD. **(c)** 2D fit results as described in the text for the scattering data shown on the CCD.

the MFM image of the magnetic domains measured prior to the FERMI experiment. As can be seen in scattering on the detector in Fig. 5.1, the diffraction pattern consisted of both isotropic (ring) and anisotropic (lobes) scattering components due to the presence of both labyrinthine and stripe domains. The laser pump fluence was calculated assuming a flat top profile for the energy density and a spot size of 390 µm. EUV fluence was limited to 1 mJ/cm^2 to prevent any pumping effects from it. All images were normalized to the incoming X-ray intensity using the small amount of light that was captured on the detector near $q = 0$.

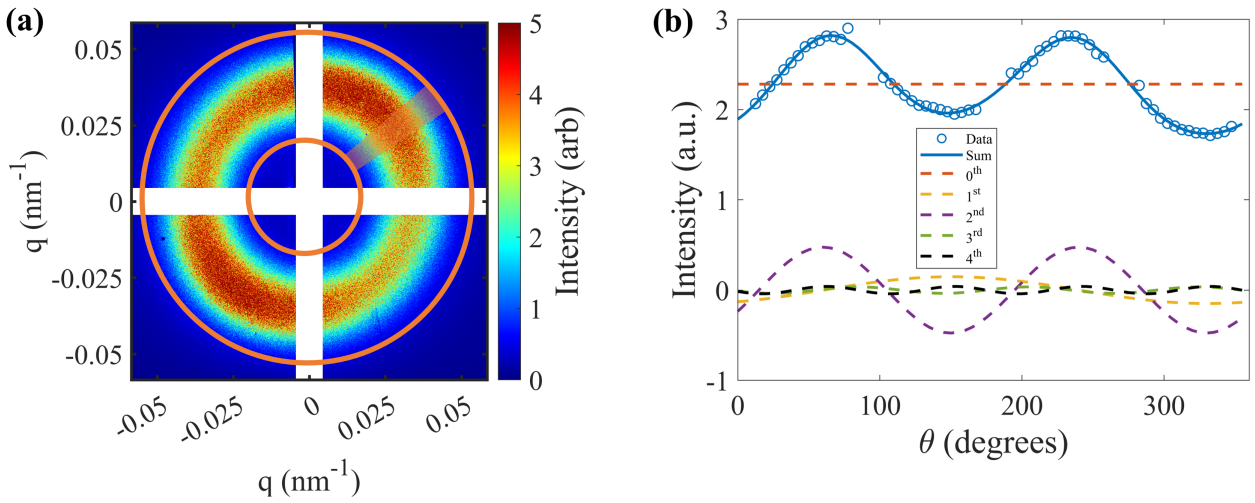

Figure 5.2: **Intensity as a function of azimuthal angle and its Fourier decomposition. (a)** Representative scattering pattern from a mixed state along with a schematic of the wedge used to create an azimuthal profile. **(b)** Azimuthal profile (blue data points) and fit (blue line) along with the individual Fourier series components (0^{th} to 4^{th}).

5.2 FFT analysis and phenomenological model for 2D fits

As discussed in Chapter 1 most of the studies utilized azimuthal integration to extract the peak position and peak profile. In one of our recently published results [66], we show that integrating the scattering image azimuthally can result in artifacts (reduced intensity and shifted radius) if the 2D CCD detector has some dead areas or if a beam block is used. In order to combat this, we developed a phenomenological fit that can model the whole scattered intensity.

In order to establish this phenomenological function used for the 2D fitting, we employed Fast Fourier Transforms (FFTs) of the radially averaged diffraction intensity along the azimuthal dimension. Fig. 5.2(a) shows a scattering image (post background subtraction) along with a schematic of a wedge over which the data was averaged to extract the az-

imuthal profile. The obtained azimuthal profile is plotted in Fig. 5.2(b) (open circles) along with the Fourier series fit components (dashed lines). The FFT obtained from the measured diffraction pattern exhibited five distinct components, identified as the 0^{th} through 4^{th} azimuthal harmonics. 0^{th} (isotropic scattering), 1^{st} (odd harmonic scattering), and 2^{nd} (anisotropic scattering) order were found to be the major components in the azimuthal dimension. The observed 0^{th} and 2^{nd} harmonics indicate that the sample is in a mixed state with both labyrinthine and stripe-like components to the domain pattern (see Fig. 5.1(a)). This is consistent with the recent results reported for the same samples measured at the L_3 edge at the European XFEL by Zhou Hagström et al. [66]. The observed 1^{st} harmonic may originate from birefringence due to the chiral nature of the Bloch-like domain walls. Its origin is discussed in detail in the paragraph below. The observed 3^{rd} and 4^{th} harmonics are higher-order components of the azimuthal dependence of the diffraction pattern with an order of magnitude lower amplitude compared to the 0^{th} and 2^{nd} orders.

Based on the FFTs analysis, five components with each proportional to $\cos(n\theta)$, where $n = 0...4$ were included in the phenomenological model used for fitting the scattered diffraction pattern. Please note that we also performed 2D fits with the analytical approximation of Voigt profile proposed by Liu et al. [100] and found that the within the margin of error, the peaks are Lorentzian in character. So, a symmetric Lorentzian in the radial direction modulated with a Fourier cosine term in the azimuthal dimension was found to give the best fits with the lowest residual. The functional form used to fit the 2D scattering images is given by,

$$f(q,\varphi) = B + f_{iso}(q) + f_{odd}(q,\varphi) + f_{aniso}(q,\varphi) \tag{5.1}$$

where B is the uniform background, q is the wavevector, and φ is the azimuthal angle. $f_{iso}(q)$ represents the isotropic component (0^{th} harmonic) of the scattering which is a result of scattering from the randomly oriented labyrinthine domains. It is a function of wavevector

q and is modeled using a symmetric Lorentzian (see Eq. (5.2)),

$$f_{iso}(q) = I_R \left[\frac{1}{\left[\frac{(q-q_R)}{\Gamma_R}\right]^2 + 1} \right]^2 . \tag{5.2}$$

where q_R is the ring radius and Γ_R is the ring width. $f_{odd}(q,\varphi)$ is the asymmetric scattering component (1^{st} and 3^{rd} harmonics) and is a function of both wavevector (q) and the azimuthal angle (φ). $f_{odd}(q,\varphi)$ is modeled as a symmetric Lorentzian modulated by the appropriate odd-order harmonics (see Eq. (5.3)).

$$\begin{aligned} f_{odd}(q,\varphi) = & \left[\frac{1}{\left[\frac{(q-q_O)}{\Gamma_O}\right]^2 + 1} \right]^2 \times \\ & \left[\left[\frac{I_O}{2} \left(\cos\left(\theta - \varphi_O\right) + 1 \right) \right] + \left[\frac{I_{O_3}}{2} \left(\cos\left(3\left(\theta - \varphi_O\right)\right) + 1 \right) \right] \right] . \end{aligned} \tag{5.3}$$

The anisotropic scattering which originates from the stripe-like domains (2^{nd} and 4^{th} harmonic) is represented by $f_{aniso}(q,\varphi)$. It is also a function of wavevector q and the azimuthal angle φ and is modeled using a symmetric Lorentzian modulated with the even-order cosine harmonics:

$$\begin{aligned} f_{aniso}(q,\varphi) = & \left[\frac{1}{\left[\frac{(q-q_L)}{\Gamma_L}\right]^2 + 1} \right]^2 \times \\ & \left[\left[\frac{I_L}{2} \left(\cos\left(2\left(\theta - \varphi_L\right)\right) + 1 \right) \right] + \left[\frac{I_{L_4}}{2} \left(\cos\left(4\left(\theta - \varphi_L\right)\right) + 1 \right) \right] \right] . \end{aligned} \tag{5.4}$$

The final form of the 2D fit equation was obtained by combining Eqs. (5.1) to (5.4) and all fit parameters for the full 2D fit are tabulated in Table 5.1. Here we would like to note that even though we are have thirteen independent fit parameters (see Table 5.1) as overfitting is not a concern as all the included parameters have physical significance and

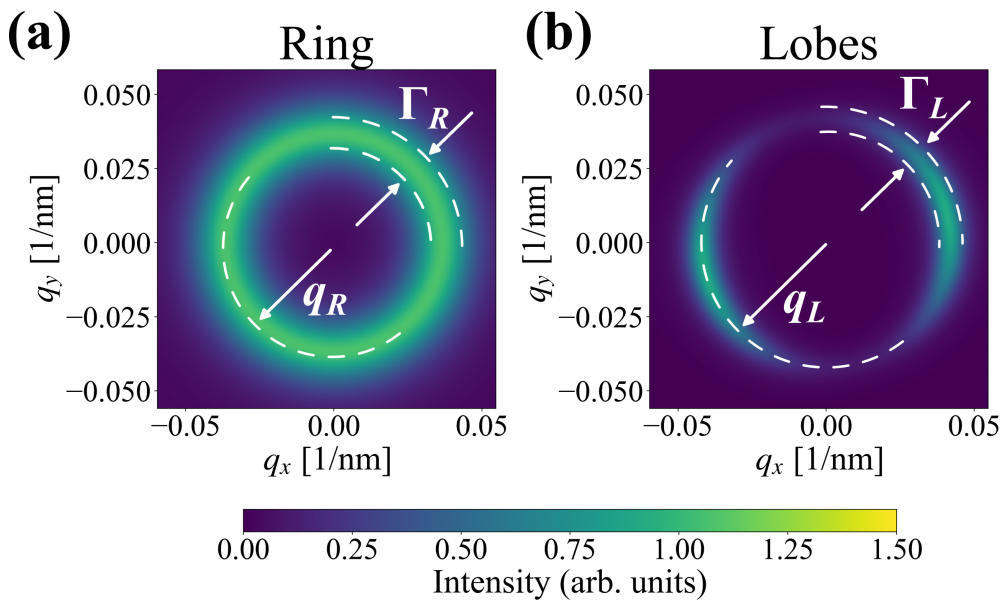

Figure 5.3: **Fit parameters superimposed on isolated fit results.** Isolated isotropic (ring) and anisotropic (lobes) components superimposed with arrows indicating the radius (q_R, q_L) and full-width half maximum (Γ_R, Γ_L) of scattering.

warrant inclusion in the fitting function, as these are the minimum necessary physical and statistical parameters to describe the textured labyrinthine domains and domain walls in this sample. Furthermore, if the fit parameters used were not orthogonal to each other, we would get large cross correlation values in the Jacobian sensitivity matrix from the fits, which was not the case for our fitting results. The values for Jacobian are not reported here in the interest of being succinct, but the all the code for 2D fitting has been made available on my GitHub at this link. Also, a python function with implementation of full fit function can be found at Code A.0.3

As discussed in Section 2.7, the scattering ring radius and width correspond to the domain periodicity and correlation length respectively. Fig. 5.3 shows both scattering radius (q_R, q_L) and full-width half maximum (Γ_R, Γ_L) of scattering superimposed on isolated isotropic (ring) and anisotropic (lobes) components with arrows. Fig. 5.4 shows the results from the

aforementioned 2D fit procedure along with the residual. Fig. 5.4(d-f) shows the individual components from the 2D fit. Scattering from the labyrinthine domains has the highest amplitude with twice the intensity and smaller radius (q_R) compared to the other components. This difference in the wavevectors for labyrinth domains compared to other components gives rise to an elliptical appearance of the scattering pattern in Fig. 5.4(a). The 2^{nd} order was the second largest component, with roughly half the intensity of the 0^{th} order component. The functional form of our 2D fit function is similar to the phenomenological model used by Zhou Hagström et al. [66]. The primary difference is due to FFT being applied to obtain the azimuthal dependence of the diffraction pattern intensity. Thus, we fitted intensity and not amplitude. As such, all reported values for amplitude A are the magnitude $|A|$, derived from the intensity I via $A = \sqrt{I}$. Note that the intensity scale for the residuals is 2.5 times smaller than the raw data and the fit. The small amplitude of the residual indicates that our model is an adequate approximation of the data for the purposes of time-resolved analysis

Table 5.1: Tabulated parameters used in 2D fits. Please note that amplitude A is derived from the intensity I via $A = \sqrt{I}$.

	Ring	Odd		Lobes	
Azimuthal Harmonic $\rightarrow$	0^{th}	1^{st}	3^{rd}	2^{nd}	4^{th}
Amplitude	A_R	A_O	A_{O_3}	A_L	A_{L_4}
Peak position	q_R	q_O	q_O	q_L	q_L
Peak width	Γ_R	Γ_O	Γ_O	Γ_L	Γ_L
Lobe angle		φ_O	φ_O	φ_L	φ_L

As mentioned above, the FFT analysis also yielded two *odd-order* components. From the standpoint of diffraction alone, such odd-order diffraction features are forbidden. One plausible explanation for these anomalous components is the combination of the transverse magneto-optic effect in transmission combined with far-field diffraction from domain walls.

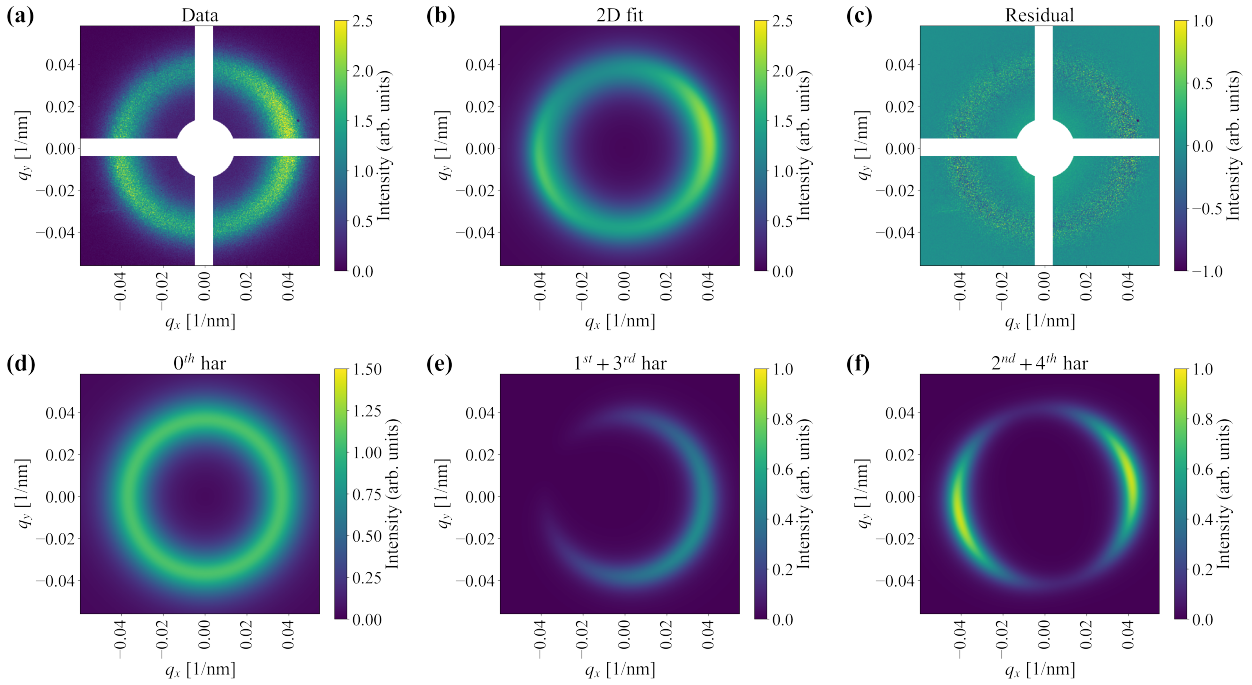

Figure 5.4: **2D fit results and fit components.** Shows 2D fit results for a representative scattering pattern using the phenomenological model. **(a)** raw experimental scattering data, **(b)** fit results, and **(c)** residual. Note that the intensity scale for residual is 2.5 times smaller than the raw data and the fit. Isolated scattering obtained from the fits for **(d)** labyrinth domains, **(e)** odd harmonic, and **(f)** stripe domains. Note that the intensity scale for odd harmonic and stripe domains is 1.5 × smaller than the scale for labyrinth domains.

A detailed discussion on the origin of odd-order diffraction can be found in Jangid et al. [101]. A similar one-sided lobe structure via diffraction from a perpendicular multi-domain sample was previously observed by Sant et al. [102] in the reflection geometry.

In our case, the observation of such an effect is contingent on a trivial magnetic topology, where the in-plane component of the magnetization does not alternate periodically between adjacent walls, i.e. adjacent walls have opposite chirality. Otherwise, the sense of gyromagnetic rotation of the optical polarization in the walls would alternate sign, thereby destructively interfering when transmitted into the far field. Given the nature of our samples, the requisite Dzyaloshinskii-Moriya interaction (DMI) necessary to imbue non-trivial

topology is not expected.

Odd-order components were not observed when the same samples were utilized at a coherent X-ray source [66]. This is to be expected because of the greatly reduced Faraday rotation of magnetic materials at x-ray wavelengths [103, 104]. Further elucidation of odd-order is required to verify the physical origins of the effect. Our FFT analysis also indicates the presence of a 3^{rd} and 4^{th} order harmonics. However, these higher-order components were >10 times smaller than the 1^{st} and 2^{nd} order harmonics. Subsequent analysis shows that they react very similarly when optically pumped. Given their small amplitudes, as well as the apparent redundancy of their ultrafast response, we focused on the 0^{th} and 2^{nd} harmonics.

5.3 Ultrafast evolution of magnetization and domain morphology

Fig. 5.5(a-c) shows the ultrafast temporal evolution of the isotropic diffraction ring in terms of amplitude A_R, q-space radius q_R, and full width half max Γ_R. An ultrafast distortion of the diffraction ring was observed, manifesting as both a reduction in the ring radius, and a broadening of the ring width. The temporal evolution of the equivalent parameters for odd-order (A_O, q_O, Γ_O) and the anisotropic lobe pattern (A_L, q_L, Γ_L) are presented in Fig. 5.5(d-f) and Fig. 5.5(g-i) respectively. The demagnetization for all three components (A_R, A_O and A_L) occurs within 100-200 fs followed by a slower recovery between 400 fs and 1.4 ps, depending on the fluence as further discussed in next section. The ultrafast responses of q_O, q_L, Γ_O and Γ_L are relatively small compared to the 0^{th} order components (Fig. 5.5(b-c)). The amplitudes of the 3^{rd} and 4^{th} harmonics are 10 times smaller than the 1^{st} and 2^{nd} harmonics as shown in Fig. 5.6. Note that low fluences are not shown in Fig. 5.6

due to inadequate signal-to-noise. Furthermore, I will primarily focus on the results from labyrinthine and stripe domains, as further studies are warranted to establish conclusive insights into the odd-order phenomena.

5.4 Quantifying temporal evolution of demagnetization, peak position and width

The temporal evolution of A, q, and Γ, (shown in Fig. 5.5) were fitted with a double-exponential function convoluted with a Gaussian kernel, as previously utilized by Unikandanunni et al. [105] and Zhou Hagström et al. [66]. This double exponential is defined as follows:

$$f(t) = \left(C + Ae^{-(t-t_0)/\tau_m} - Be^{-(t-t_0)/\tau_R} + \frac{B-A}{\sqrt{t/\tau_{R2}+1}} \right) \circledast G(t) \tag{5.5}$$

where, C defines the pre time zero shift value, A was the scaling factor for the ultrafast exponential demagnetization term, B is the scaling factor for fast recovery, t_0 is the temporal shift incorporated to take into account the time jitters in FEL, τ_m is the quench time constant, τ_R is the short time recovery time constant and τ_{R2} is the slow recovery time constant. For temporal fits of normalized A_R and A_L, C was set to 1 whereas for peak position (q_R, q_L) and peak width (Γ_R, Γ_L), a value of 0 was used. The temporal fit equation was convoluted with a 45 ps Gaussian $(G(t))$ to model the effects of finite width of the probe. Due to the limited time range of measured delay curves, slow recovery time constant $(\tau_{R2} \to \infty)$ was assumed to approach infinity. Quench time $(t_{\min})$ was obtained by calculating the roots of time derivative of Eq. (5.5) and can be written as follows:

$$t_{\min} = t_0 - \frac{\tau_m \tau_R}{\tau_R - \tau_m} \ln\left(\frac{B\tau_m}{A\tau_R}\right) \tag{5.6}$$

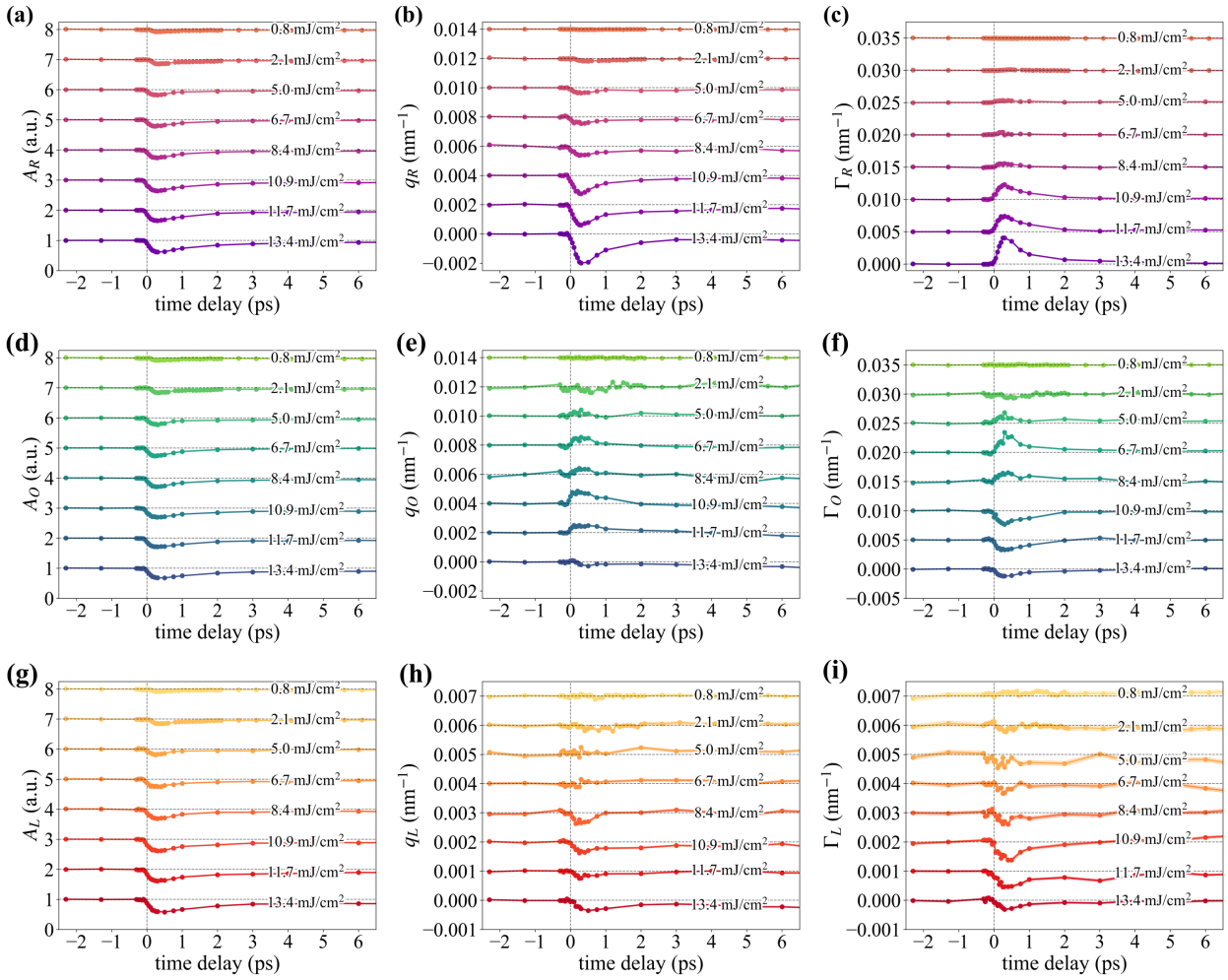

Figure 5.5: **Evolution of labyrinthine, odd-order and stripe as a function of delay time and fluence.** Temporal evolution of amplitude (A), scattering vector/radius (q), and FWHM of scattered peak (Γ) for labyrinthine **(a-c)**, odd-order **(d-f)**, and stripe domains **(g-i)**. These results were obtained using 2D fitting of the phenomenological model on EUV diffraction pattern. Delay curves are plotted for a range of measured fluence values from 0.8 to 13.4 mJ/cm^2. The scattering amplitude **(a, d, g)** which is proportional to magnetization, decays immediately following laser excitation indicating demagnetization which recovers on ps timescales. Only scattering vector/radius **(b, e, h)** and width **(c, f, i)** of for labyrinthine domains show a strong and consistent ultrafast response. Note that the plotted data for A, q and Γ is relative to the before t = 0 value.

In order to calculate the amount of quench, one can plug the value of $t_{\min}$ from Eq. (5.6) back into the temporal fit function given in Eq. (5.5). This amount of quench (A_q) can be

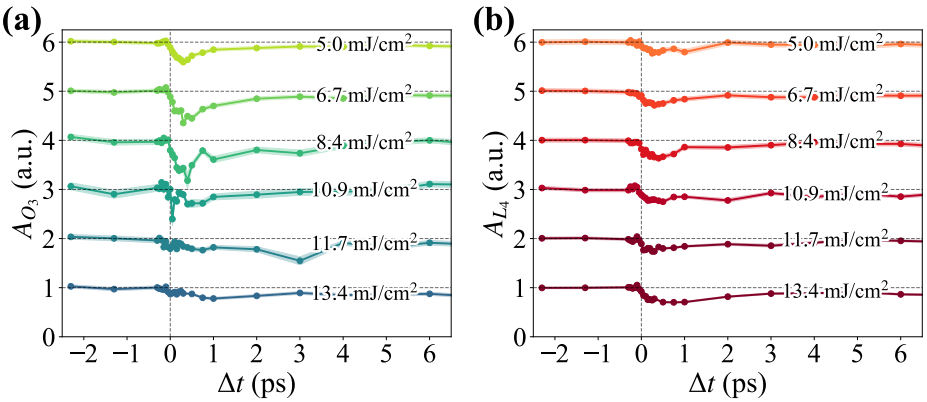

Figure 5.6: **Scattering amplitude of 3^{rd} and 4^{th} harmonics as a function of delay time for various pump fluence.**

expressed as follows:

$$A_q = A\left[1 - \left(\frac{B\tau_m}{A\tau_R}\right)^{\tau_R/(\tau_R-\tau_m)}\right] - B\left[1 - \left(\frac{B\tau_m}{A\tau_R}\right)^{\tau_m/(\tau_R-\tau_m)}\right] \tag{5.7}$$

Fig. 5.7(a) shows both the data and the temporal fit for A_R. The residual ($\approx$ 25 times smaller than the signal) is plotted on the top panel of the same figure. Fig. 5.7(b) and its inset, compares the temporal evolution data for A_R, q_R, and Γ_R, as extracted from the 2D fitting for the maximum pump-fluence of 13.4 mJ/cm^2. There is a visible difference in the apparent quench time and recovery time between A_R and both q_R and Γ_R resulting in differences in τ_m and τ_{rec} extracted using the temporal fitting as will be discussed in the next paragraph. This temporal fit method was used to extract A_R, A_L, Δq_R and $\Delta\Gamma_R$ plotted in Fig. 5.8. Quench time τ_m and recovery time τ_{rec} plotted in Fig. 5.9 were also extracted using these temporal fits.

Fig. 5.8 shows the fluence-dependence for both the ring and lobes including demagnetization ($\Delta A_R/A_R$, $\Delta A_L/A_L$), radial peak shift ($\Delta q_R/q_R$, $\Delta q_L/q_L$) and ring broadening ($\Delta\Gamma_R/\Gamma_R$, $\Delta\Gamma_L/\Gamma_L$) relative to the average fitted pre-pump values for $t < 0$. These results

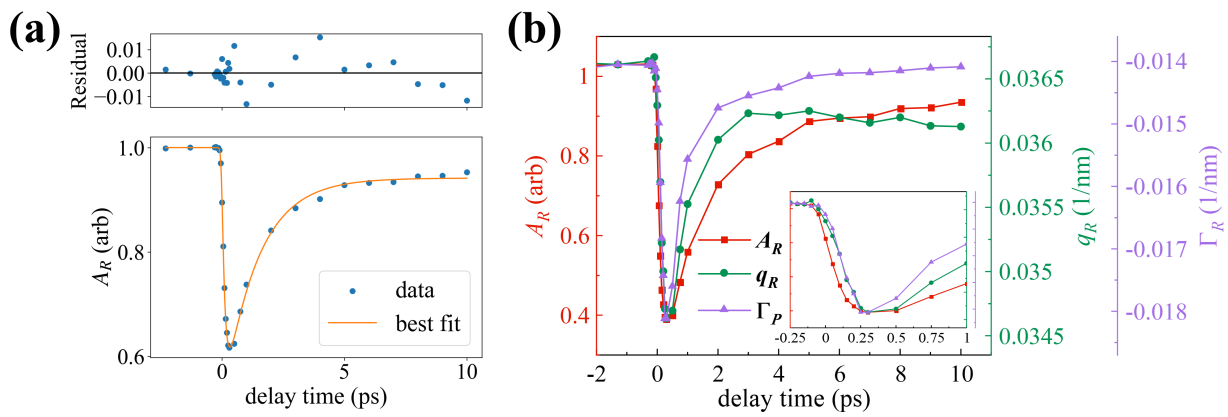

Figure 5.7: **Temporal fit and comparison of temporal evolution of A_R, q_R and Γ_R. (a)** Temporal evolution of scattering amplitude for labyrinth domains along with the fit for 13.4 mJ/cm^2. This fit was obtained using a temporal fit function discussed in SI section Section 5.4. The residual from the fit is also shown above. **(b)** Compares the temporal evolution of the scattering amplitude (A_R) radial ring position (q_R) and the ring width (Γ_R) for labyrinth domains for a fluence of 13.4 mJ/cm^2.

are also tabulated in Table 5.2. Please note that double exponential fits could not be performed reliably for q_L and Γ_L, so the results presented in Table 5.2 are the cuts at maximum quench. The fluence dependencies of both $\Delta A_R/A_R$ and $\Delta A_L/A_L$ are very similar, and are consistent with most previous pump-probe studies [66]. The non-linearity of both $\Delta q_R/q_R$ and $\Delta\Gamma_R/\Gamma_R$ seen in Fig. 5.8(b) and (c) is in stark contrast to the linear fluence-dependence of the amplitude quenching $\Delta A_R/A_R$ and $\Delta A_L/A_L$ shown in Fig. 5.8(a). $\Delta q_R/q_R$ and $\Delta\Gamma_R/\Gamma_R$ exhibit a distinct threshold-like feature. For fluences below 7 mJ/cm^2, a relatively weak linear dependence of both $\Delta q_R/q_R$ and $\Delta\Gamma_R/\Gamma_R$ on fluence is observed. Above 7 mJ/cm^2, a much steeper linear dependence of $\Delta q_R/q_R$ and $\Delta\Gamma_R/\Gamma_R$ on pump fluence is observed, with $\Delta q_R/q_R = 5.3\pm0.8\%$ and $\Delta\Gamma_R/\Gamma_R = 26.7\pm3.8\%$ at the highest fluence. In contrast, $\Delta q_L/q_L$ and $\Delta\Gamma_L/\Gamma_L$ are much smaller and without any apparent linear dependence on fluence, with largest observed shifts of $1.0\pm0.4\%$ and $8.1\pm3.8\%$, respectively. The threshold-like behavior of the ultrafast diffraction ring distortions is the first main experimental result of this study.

Table 5.2: Normalized percent change for amplitude (A_R, A_L), peak position (q_R, q_L) and peak width (Γ_R, Γ_L) for labyrinthine (subscript R) and stripe (subscript L) for various pump fluences. The presented results are the same as plotted in Fig. 5.8 of the manuscript and were obtained using double exponential fits. Please note that double exponential fits could not be performed reliably for q_L and Γ_L, so the results presented here are the cuts at maximum quench.

	Labyrinthine/Ring			Stripe/Lobes		
Fluence (mJ/cm^2)	A_R(%)	q_R(%)	Γ_R(%)	A_L(%)	q_L(%)	Γ_L(%)
0.8	-7.1 ± 4.1	-0.1 ± 0.4	0.2 ± 0.5	-7.6 ± 3.3	0.0 ± 0.3	2.1 ± 1.6
2.1	-14.3 ± 0.9	-0.4 ± 0.3	0.8 ± 0.9	-14.8 ± 1.5	-0.4 ± 0.3	-2.5 ± 1.4
5.0	-17.4 ± 3.1	-1.0 ± 1.0	2.4 ± 0.7	-17.8 ± 3.4	0.4 ± 0.4	-4.0 ± 2.4
5.9	-19.2 ± 6.0	-1.3 ± 1.2	1.1 ± 3.4	-22.8 ± 4.3	0.5 ± 0.7	-2.5 ± 4.7
6.7	-21.1 ± 1.9	-1.3 ± 2.7	2.0 ± 1.8	-24.9 ± 7.9	0.2 ± 0.3	-2.9 ± 2.1
7.5	-23.0 ± 3.1	-1.2 ± 0.8	3.1 ± 0.8	-26.9 ± 8.8	-0.4 ± 0.3	-3.8 ± 2.2
8.4	-25.8 ± 2.4	-1.7 ± 1.6	4.2 ± 4.0	-30.6 ± 8.5	-0.8 ± 0.5	-4.1 ± 3.7
9.2	-27.8 ± 2.3	-2.3 ± 1.3	7.3 ± 2.9	-31.4 ± 5.9	-1.1 ± 0.4	-4.5 ± 3.1
10.0	-32.5 ± 2.3	-2.8 ± 0.7	13.5 ± 3.4	-33.5 ± 11.9	-1.0 ± 0.4	-2.0 ± 4.4
10.9	-35.2 ± 3.5	-3.3 ± 0.9	15.7 ± 3.1	-38.1 ± 6.5	-0.8 ± 0.3	-8.1 ± 3.8
11.7	-34.3 ± 2.9	-3.7 ± 0.9	17.5 ± 2.5	-37.6 ± 3.1	-0.4 ± 0.3	-7.8 ± 3.0
12.6	-35.9 ± 3.2	-4.3 ± 0.8	20.0 ± 3.4	-39.9 ± 8.0	-0.9 ± 0.2	-6.2 ± 2.1
13.4	-38.5 ± 1.8	-5.3 ± 0.8	26.7 ± 3.8	-42.7 ± 6.0	-0.8 ± 0.3	-4.3 ± 1.7

Time constants for the initial ultrafast changes τ_m and slower recovery τ_{rec} for A_R, A_L, q_R and Γ_R are presented in Fig. 5.9. The demagnetization times for both the ring and lobes vary between 100 to 200 fs, indicative of a similar demagnetization process for labyrinths and stripes. Surprisingly, the time constants τ_m for the change in ring radius and ring width vary between 100 to 300 fs, with most data falling between 200 and 300 fs (see Fig. 5.9(a) purple region); significantly slower than the demagnetization times (see Fig. 5.9(a) orange region). In addition, the recovery times τ_{rec} are also different between the demagnetization and ring shape distortions. The demagnetization recovery times vary from $\approx$ 600 fs to $\approx$ 1.2 ps, whereas both the ring radius and width recover much faster, with most data falling between 200 fs and 600 fs, dependent on the fluence. This difference in temporal response for demagnetization and ring distortion is the second key finding of this study.

The threshold fluence for ring distortion ($\Delta q_R/q_R$ and $\Delta\Gamma_R/\Gamma_R$ in Fig. 5.8) suggests that there is an activation energy barrier impeding domain rearrangement as typically observed

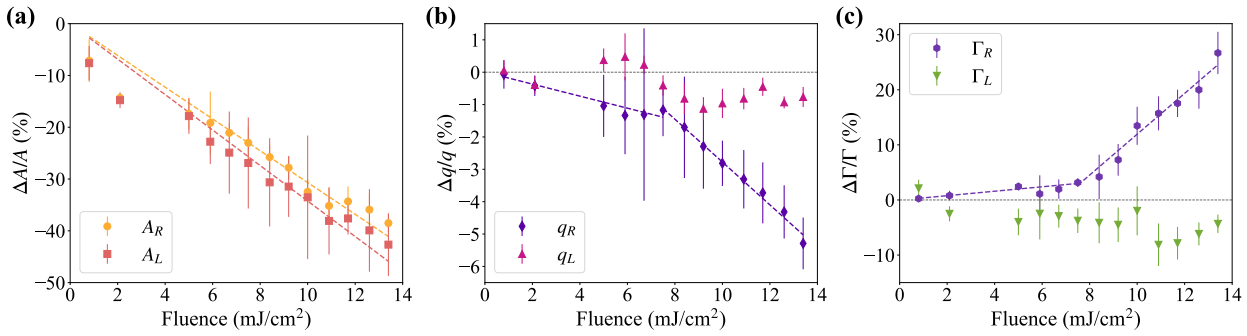

Figure 5.8: **Laser fluence dependence of isotropic and anisotropic scattering resulting from labyrinthine and stripe domains. (a)** Normalized scattered amplitude dependence on fluence for both the isotropic (A_R) and anisotropic scattering (A_L). Fluence depdence of **(b)** ring shift and **(c)** width for both the ring ($\Delta q_0/q_0$ and $\Delta\Gamma_0/\Gamma_0$) and lobes ($\Delta q_2/q_2$ and $\Delta\Gamma_2/\Gamma_2$). The dashed lines indicate the results of linear error-weighted fits of the data. For A_R and A_L, the fits extend over the entire range of pump fluence. For $\Delta q_0/q_0$ and $\Delta\Gamma_0/\Gamma_0$, two fits were performed below and above the threshold fluence of 7.8 mJ/cm^2.

for conventional field-driven wall dynamics [63]. This result is consistent with the hypothesis that domain rearrangement in the presence of pinning sites is the source of ultrafast ring distortions. Furthermore, the relatively slow rate (Fig. 5.9) for the change of $\Delta q_R/q_R$ and $\Delta\Gamma_R/\Gamma_R$ is consistent with domain-wall motion. Domain-walls are bound magnetic solitons that exhibit an effective inertia [97, 98] that impedes the response to any driving torque. Thus, based on the distinct response times for demagnetization and the ring distortions, we can confidently rule out any hypothesis that the distortions in diffraction ring shape are simply derivative results of ultrafast demagnetization process.

Fig. 5.10 compares our results to previously reported ultrafast measurements of magnetic domain pattern evolution. Fig. 5.10(a) plots the normalized peak shift ($\Delta q/q_0$) as a function of magnetization quench ($\Delta M/M_0$) for labyrinth domains by Zhou Hagström et al. [66], Pfau et al. [64], Zusin et al. [65] and this study. Our measurements (blue circles) are in good agreement with the measurements done at the European XFEL on the same sample [66]. Furthermore, our measurements also indicate the presence of a similar threshold present in

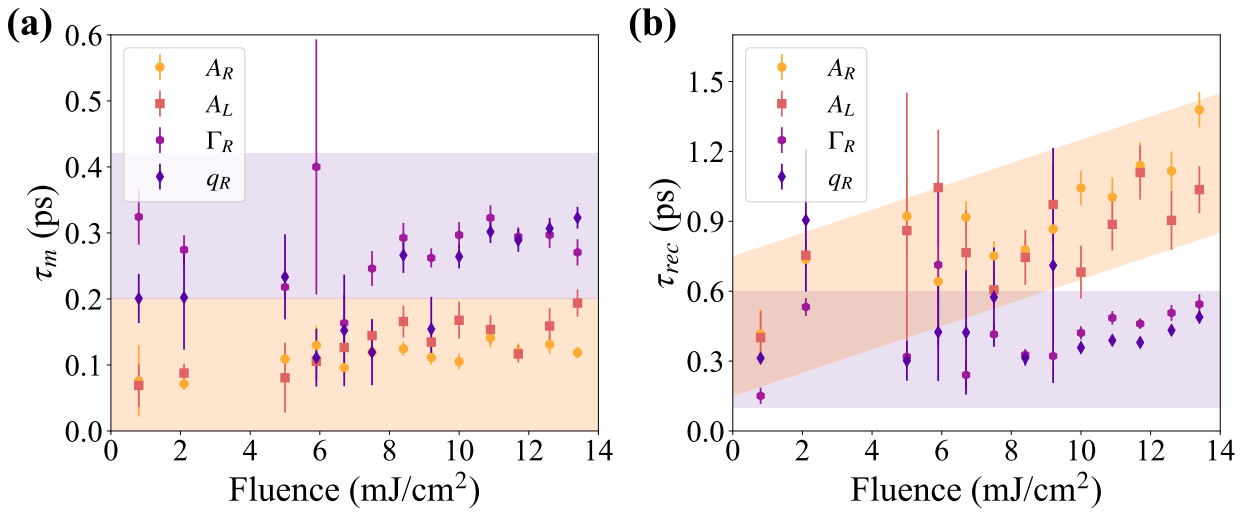

Figure 5.9: **Laser fluence dependence of quench and recovery time. (a)** Quench and **(b)** recovery time constants obtained from the temporal fits (see Section 5.4) for A_R, A_L, q_R and Γ_R. The magnetization quench is two times faster than the change in radial ring position and ring width ($\tau_m \approx 0.3$ ps) irrespective of the fluence value. The recovery time constants (τ_{rec}) for magnetization quench (A_R and A_L) are also distinct from τ_{rec} for ring shift (q_R) and width (Γ_R)

previous studies where no peak shift is observed for low fluence. The comparison of Δq for different studies shows that these effects are ubiquitous for all samples that support labyrinthine domains, although the dependence on fluence, we suspect, is strongly material dependent, such as the multilayer stack design, pinning sites, defect density, and materials used. Fig. 5.10(b) shows Δq for stripe-like domains as a function of pump fluence in Zhou Hagström et al. [66], Vodungbo et al. [67] and Hennes et al. [106], as well as this study. Only marginal or no shifts in q were observed in all four studies which is consistent with minimal to no shift observed for stripe domains.

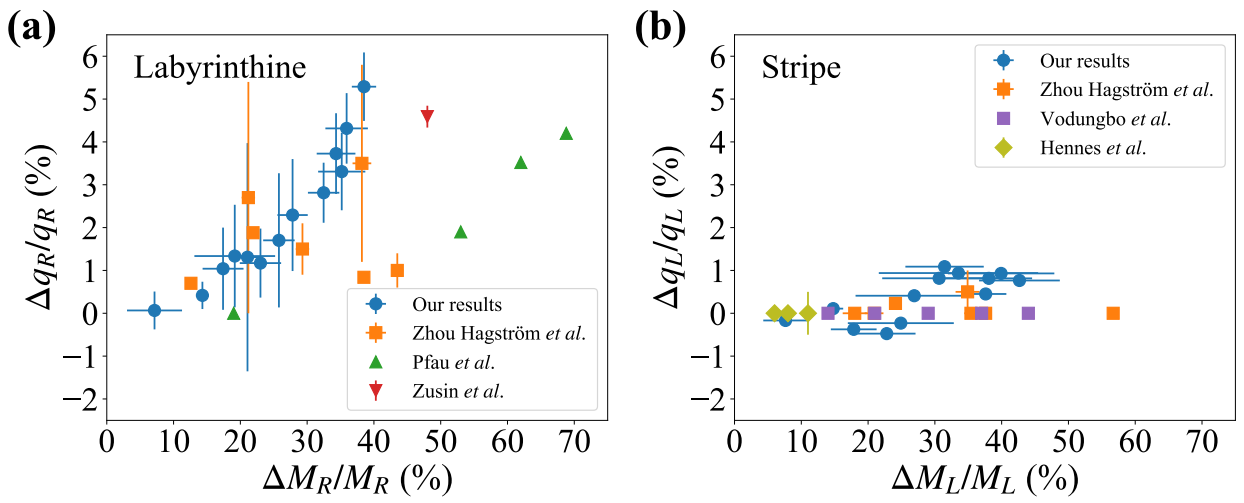

Figure 5.10: **Radial shift vs Magnetization quench.** The figure compares the normalized change in radial peak position as a function of normalized magnetization change from this study with other publications for labyrinth **(a)** and stripe **(b)** domains Pfau et al. [64], Zusin et al. [65], Zhou Hagström et al. [66], Vodungbo et al. [67], and Hennes et al. [106].

5.5 Role of domain wall curvature

Given the substantial differences in the ultrafast distortions of the stripe and labyrinth domain pattern, in agreement with the previous report [66], it is natural to inquire what characteristic features of labyrinth and stripe domains underlie such differences in temporal response. An obvious difference is the abundance of curved domain walls for labyrinths. The possibility of curved wall motion, in contrast to that for straight walls, is consistent with the requirement of symmetry-breaking. Symmetry-breaking was provided in the original prediction of ultrafast wall motion by non-uniform laser illumination of a straight domain wall [51]. In our case, the symmetry-breaking is geometrical, inherent in the wall curvature.

To verify whether the spatial motion of curved domain walls can give rise to the observed contraction of the diffraction ring radius, we performed micromagnetic simulations [107] for the case of a perpendicularly magnetized thin film. MuMax3 [107] was used for the

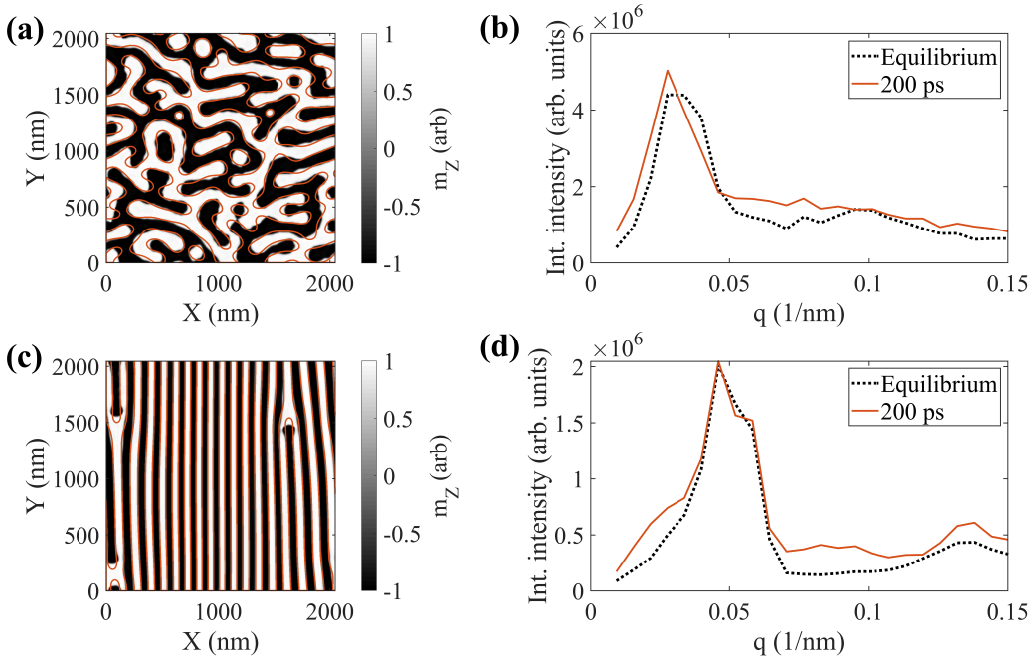

Figure 5.11: **Micromagnetic simulations of domain pattern.** Modified simulated (black and white) and initial domain pattern (red outline) for **(a)** labyrinthine and **(c)** stripe domain pattern. The modified simulated pattern was obtained by reducing the magnetization by 40 % for both labyrinth and stripe domains respectively. A decrease in the curvature of the curved domain wall is observed for both domain patterns. Azimuthally integrated intensity from a 2D fast Fourier transform for **(b)** labyrinthine and **(d)** stripe domain pattern. The dashed black line is for the initial state and the solid red line is for the modified state at 200 ps. A clear shift in the ring radius is observed for labyrinthine domains whereas no shift is observed for stripe domains.

simulations and ran in a GTX QUADRO 5000 GPU. In order to model Δq, we simulated the initial magnetization distribution for a sample with parameters similar to that used in this study. The magnetization was allowed to relax into an equilibrium labyrinthine domain-pattern. The saturation magnetization was then decreased instantaneously by 40% of its original value similar to the experimentally observed magnetization quench (Fig. 5.8) for the highest pump fluence of 13.4 mJ/cm^2. The system was then allowed to evolve according to conventional micromagnetic parameters and relax to a transient intermediate state at 200

ps.

The saturation magnetization (M_s) used in micromagnetic simulations was determined to be 616 kA/m using SQUID magnetometry Shaw, Nembach, and Silva [108]. The first and second-order anisotropy constant were K_1= 739 kJ/m^3 and K_2 = -266 kJ/m^3, respectively, and the exchange constant $A = 20$ pJ/m, using the values determined for similar samples in Zusin et al. [65]. The Gilbert damping constant (α) was set to $\alpha = 0.01$ which is in the order of magnitude for metallic alloys. Because the estimation of domain speed is independent of time in our study, a precise value for damping was not needed. The labyrinthine domain pattern was stabilized from a random initial condition while an experimental data set for a similar magnetic system was used for the initial condition for the stripe domain pattern.

The simulated modified domain pattern at 200 ps for both labyrinthine and stripe domains is presented in Fig. 5.11(a) and (c), respectively. The red outline traces the domain boundaries for the initial equilibrium state. The displacement of the curved domain walls is observed for both labyrinths and stripes, but the effect is more pronounced in the labyrinthine domain pattern due to the abundance of curved walls. For stripes, the most prominent displacements occurred for cap walls where the stripe domains terminate. The curvature dependence of domain wall motion is further illustrated in Fig. 5.12(a), which presents the simulated modified labyrinth domain pattern (black and white domains) and compares it with the initial domain pattern, where only the outline is shown and the color denotes initial wall curvature. The figure clearly shows that domain walls with higher curvature (dark red or blue) undergo noticeable wall motion. Note that while the time scale for the wall displacement is not accurate due to the use of micromagnetic simulations [109], the dependence of wall displacement on wall curvature allows us to examine how such domain rearrangement affects the diffraction pattern in the reciprocal space.

To simulate X-ray scattering, an FFT was applied to both the initial and modified domain

patterns. In the case of the labyrinthine domains, the FFT yielded an isotropic ring in reciprocal space, in qualitative agreement with the experimental results. The azimuthal integral (in reciprocal space) of the ring is shown in Fig. 5.11(b). Both a reduction of the ring radius and a broadening of the ring width occur due to domain rearrangement at 200 ps. The initial ring radius was 0.0329 nm^{-1}, similar to the experimental initial ring radius of 0.0366 nm^{-1}. Whereas the final ring radius was 0.0299 nm^{-1}. The initial ring width was 0.0237 nm^{-1}, significantly broader than the experimental ring width of 0.0130 nm^{-1}. This is attributed to the higher degree of disorder for the micromagnetic simulation.

In spite of the high degree of disorder in the micromagnetic domain pattern, the ring width still broadens as a result of the wall displacements, with a final value of 0.0254 nm^{-1}. The ring broadening relative to the radial decrease is smaller than the experiment. Again, this is because the simulated domain pattern is more disordered than the experimental domains. The FFT for the stripe domains does not yield any discernable shift in radius or width after relaxation for the reduced saturation magnetization. This is attributed to the low density of curved segments of the domain-walls. Note that if the micromagnetics simulations were allowed to run longer there would be increase in the domain periodicity due to lowering of saturation magnetization. However, such homogenous changes in the domain periodicity at ultrafast timescales would lead to extremely fast expansion of the domain widths, which would be unphysical [64].

The explanation why a reduction in the saturation magnetization results in the wall displacement, we mapped a curved domain wall into one dimension by defining a profile dependent on the total moment $\mu(x) = \mu_a \tanh \frac{x}{a} + \mu_{av}$, where μ_a is the asymptotic value of a symmetric domain profile, and $\mu_{av} = \mu(x = 0)$. Under the assumption that ultrafast quenching minimizes the non-local dipole field that stabilizes the texture in equilibrium, we seek a new symmetric distribution for $\mu(x)$. This leads to a net shift of around arctanh $\left(\frac{a\kappa}{2}\right)$,

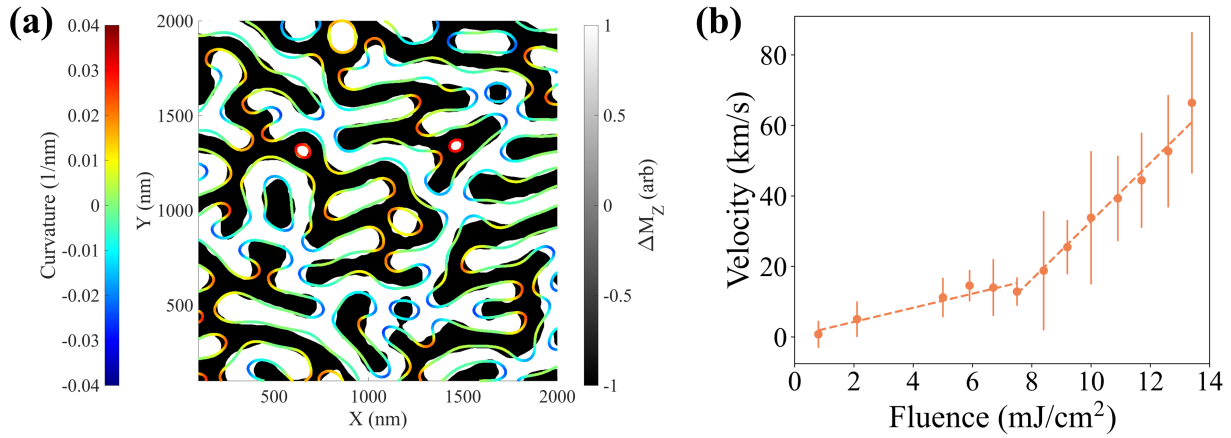

Figure 5.12: **Simulated modification of domain pattern and calculated domain wall speed. (a)** Simulated modified domain pattern (black and white domains) and initial state (colored outline). The modified state was simulated assuming a 40 % reduction in the saturation magnetization as discussed in the text. The color of the outline denotes the initial wall curvature which was estimated using inverse of the radius of local circle fit. The comparison clearly shows that regions with high curvature (dark red and blue) undergo noticeable domain wall motion. **(b)** Fluence dependence of calculated domain wall speed for labyrinth domains estimated using experimentally measured and simulated contraction of diffraction ring radius.

where κ is the domain curvature. This simple argument explains why curved domains are more prone to motion based on exchange energy, but as the model is based on micromagnetics it does not capture ultrafast motion.

5.6 Domain wall speed calculation

Numerous localized regions with shift in domain walls can be identified in the simulated domain pattern images (Fig. 5.12(a)). These localized shifts are predominantly located in regions of significant domain wall curvature with a common characteristic that the shift tends to reduce the wall curvature. Given the inherent randomness of the labyrinthine domain structure, the wall shift will induce local changes in the domain area which affects both

black and white domains. Statistically, these localized displacements of the domain wall area should average to zero, i.e. neither the black or white domains increase in area at the expense of the other. However, the root mean square (rms) of the displacement of the domain area will be nonzero and can be used to estimate the domain wall speeds. We can estimate domain wall speeds of the curved walls by utilizing both the experimentally measured and simulated contraction of diffraction ring radius. This was achieved by quantitatively correlating the reduction of diffraction ring radius ($(\Delta q/q)_{sim}$) from simulations with the modeled change in the wall position by defining parameter $K = (\Delta A_{RMS}/A) \,/\, (\Delta q/q)_{sim}$, where $\Delta A_{RMS}/A$ is fractional areal change due to wall motion.

Utilizing image analysis program written in *MATLAB* (using regionprops function) on the simulated domain pattern, we measured the rms area of the localized displacement to be 2100 nm^2. Using the curvature density of 75.1 µm^{-2} (estimated using regionprops function) we can express the localized displacement as an areal fraction of the average domain size, we obtain $\Delta A_{RMS}/A = 2100 \times 75.1 \times 10^{-6} = 0.16$. The fractional change in the ring radius in Fig. 5.11(b) is $(\Delta q/q)_{sim} = 0.095$. The ratio of the fractional areal changes to fractional radial change which is the aforementioned proportionality constant K was approximated to be 1.65.

For the rest of the analysis, we assume that this is a proportionality constant (K) between the fractional areal change at the curved sites in real space and the fractional radial change of the ring radius in reciprocal space. Note that this proportionality may depend on the details of the labyrinthine geometry. However, any such dependence should be weak because the general randomness inherent in all the meandering labyrinthine structures precludes any coherent scattering effects that might otherwise have a strong effect on the proportionality. Furthermore, we performed five different micromagnetic simulations with a change in saturation magnetization ranging from 10 % to 40 %, all of which showed that K varies in a

narrow range from 1.65 to 1.9. An average value of $K = (1.84 \pm 0.11)$ was used for speed calculations.

The domain wall speed was calculated using the following equation,

$$v = K\frac{(\Delta q/q)_{exp}}{\rho_c w \tau_m}. \tag{5.8}$$

Here $(\Delta q/q)_{exp}$ is the experimentally observed fractional change in diffraction ring radius and τ_m is the time constant for the radial shift obtained from temporal fits to the experimental data. K is the proportionality constant as defined above. w is the average domain width and ρ_c is the curvature density obtained from the MFM images. Curvature density (ρ_c) in the MFM image was estimated to be (60.39 ± 6.26) µm^{-2} by fitting curvatures post edge detection in MATLAB (using imfindcircles function). Uncertainty in curvature density was calculated using the disparity between the density for dark (down) and light (up) contrast domains in MFM. An average domain width ($w = \pi/q_0$) was calculated using the values of q_R for $t < 0$ from the 2D fit of the magnetic scattering. Using the time constant for the radial shifts ($\tau_m \approx 0.30 \pm 0.08$) ps at the maximum pump fluence of 13.4 mJ/cm^2, and estimated rms curve wall displacement of $\approx 20 \pm 3$ nm, the effective maximum speed of the wall displacement was calculated to be (66 ± 20) km/s.

The full pump fluence dependence of domain wall speed is shown in Fig. 5.12(b). Errors in each parameter used to calculate speed (Eq. (5.8)) was propagated to get the error bars shown in speed vs fluence plot (Fig. 5.12(b)). The large uncertainties seen in the plot are due to large error in determining the quench time (τ_m). It was recently shown that wall speeds approaching the maximum magnon group speed are physically allowed for a ferrimagnet under equilibrium conditions [110]. In our case, the maximum group speed for Ni is ≈ 70 km/s [111]. Thus, we also find that wall speeds approaching the maximum magnon speed are also possible for curved domain walls in a ferromagnet, but under extreme far-from-

equilibrium conditions. These extreme domain wall speeds are surprising since domain walls in ferromagnets near equilibrium are unstable when driven above the Walker limit [62, 63]. It should be also noted that the wall motion could be a combination of both wall motion and broadening, and our observations do not rule out domain wall broadening previously observed [64, 65]. The observation of extreme wall speed under far-from-equilibrium conditions is the third and most significant result of this study.

5.7 Discussion

While our results qualitatively agree with previous studies, the extracted time-constants τ_m and τ_{rec} from our 2D fits for labyrinthine domains are significantly faster than those previously reported in Zusin et al. [65]. This earlier study reported $\tau_m \approx 1$ ps, and a subsequent recovery time $\tau_{rec} \approx 10$ ps. While the magnitude of the distortions in Zusin et al. [65] is approximately the same as reported here, with $\Delta M \approx 40\%$ and $\Delta q \approx 5\%$, the difference in quench and recovery timescales is substantial. There are several significant differences in these two experiments that can account for these differences in response time: (1) Sample structure and thickness: In Zusin et al. [65], the sample is a 40-nm magnetic multilayer deposited on a 100 nm Si_3N_4 membrane. In contrast, the sample for this study is a 13 nm magnetic multilayer grown on a 100 nm Si membrane. Given an optical penetration length of only 7 nm for a Ni thin film [112], we expect that the vertical profile of magnetic quenching for our film is more substantial than that in Zusin et al. [65], which was shown by modeling to only reach approximately 10 nm into the depth of the 40-nm sample. In addition, it is plausible that the mechanics of domain wall movement induced by ultrafast pumping would be quantitatively different due to micromagnetic differences between samples of such varying thicknesses. (2) Pump fluence: Zusin et al. [65] reports a damage-threshold-limited measurement for a single pump fluence of 23 mJ/cm^2. The maximum pump fluence

for this study, also limited by the threshold for sample damage, is 13.4 mJ/cm^2. (3) Domain pattern: The domain structure reported in Zusin et al. [65] was purely labyrinthine, whereas the sample used in this study is a linearly-textured labyrinth pattern. The admixture of labyrinthine and stripe domains resulted from the exposure to the optical pump beam over the course of $\approx$ 15 minutes, similar to what was observed in Zhou Hagström et al. [66]. (4) Time resolution: The requirement of high dynamic range for the measurements in Zusin et al. [65] limited the time-resolution to 400 fs. This prevented detection of any ultrafast components of the initial magnetization response as shown in Fig. 5.9, which were all on time scales less than 400 fs.

The observation of threshold effect and distinct time constants of ring distortion and demagnetization indicate that the existing theory is still inadequate to predict the scale of the observed phenomena. The faster rate of the distortion recovery suggests more complex physics whereby the relaxation channels for wall dynamics are not identical to those for the demagnetization recovery. It is possible that other mechanisms such as magnon excitation and relaxation need to be included [113–115]. It has already been shown that ultrafast demagnetization results in substantial magnon generation [116–119]. Enhanced demagnetization in domain walls has been attributed to the excitation of both coherent and incoherent magnon-like modes in chiral domain walls [120]. Indeed, the observed temporal response of the wall dynamics is similar to that of critically damped oscillator. This suggests that far-from-equilibrium conditions can give rise to new sources of elastic torque that can affect mesoscopic spin textures in a coherent manner.

The usual theory for domain walls in ferromagnets is micromagnetic, where torques arise from energy terms in the GHz range when constrained to mesoscopic scales (10 to 100 nm). For extreme wall motion to occur, micromagnetic energy terms on the order of meV activated under far-from-equilibrium conditions are required. Dissipative superdiffusive spin

current is a possible source of the requisite THz-scale energy, but our distortion-recovery data (see Fig. 5.9(b)) show that it cannot be the only relevant mechanism; meV-scale elastic terms are required. Most proposed mechanisms for ultrafast demagnetization rely on entropy-producing microscopic single-particle processes. Such processes occur on a length scale between the lattice constant and the exchange length. However, extremely fast spatial translation of domain walls requires a long-range mechanism that extends over tens of nanometers, i.e at the mesoscopic scale [52]. The implication is that far-from-equilibrium spin kinetics in ferromagnets are not solely limited to demagnetization mechanism. There must also be generation of coherent torques at ultrafast time-scales in non-uniform mesoscopic spin textures.

5.8 Conclusion

Our work highlights two critical points for far-from-equilibrium behavior. Firstly, we report a threshold behavior in fluence dependence of ring shift and ring width which gives credence to domain walls being pinned and requiring a threshold fluence to be mobile. Secondly, we report a difference in temporal response of domain morphology and demagnetization indicating that the conventional formulation of magnetic torques is inadequate to account for all experimental observations. Lastly, our results show significant evidence of extreme domain walls speeds in qualitative agreement with theoretical predictions [51]. Our studies open up the possibility of manipulating magnetic textures to achieve far-from-equilibrium mesoscopic effects. Furthermore, the extension of these processes could be important for explaining ultrafast phenomena in other systems such as emerging quantum materials.

Chapter 6

Conclusion and Future Outlook

6.1 Magnetic properties of MPEAs

The first part of my thesis delves into the magnetic characteristics of MPEAs, demonstrating the feasibility of sputtering to grow crystalline MPEA films on Si substrates. The thin films thus produced exhibit an absence of intermetallic formation, confirmed through EDS measurements. XRD reveals a discernible influence of film thickness on crystal structure, where thinner films exhibit a proclivity to stabilize the f.c.c phase over the h.c.p phase. Furthermore, thin films show a remarkable enhancement in magnetization, culminating in a four orders of magnitude increase in saturation magnetization, when comparing bulk to thin film geometry.

Across all samples, two magnetic transitions were observed: (i) a transition from paramagnetic to spin glass phase, occurring at 390 K, and (ii) a spin glass to ferromagnetic (or ferromagnetic-like) phase transition at temperatures of 66 K, 145 K, and 250 K for bulk, 500 nm, and 65 nm thin film samples, respectively. Notably, manipulating the film thickness enabled fine-tuning of the saturation magnetization and coercivity of the ferromagnetic-like phase. XMCD investigations hint to the ferromagnetic nature of Fe and Co throughout the

studied temperature range of 12 K to 400 K, while Cr undergoes a paramagnetic to ferromagnetic transition between 200 K to 300 K for both 65 nm and 500 nm films. Furthermore, Fe and Co exhibited ferromagnetic coupling, whereas Cr displayed antiferromagnetic coupling with Fe and Co and Mn was found to lack long-range ferromagnetic ordering within the temperature range explored.

6.1.1 Future Outlook

The aforementioned results indicate the rich magnetic phases present in MPEA systems. They serves as a foundation for the manipulation of structural phases and magnetic attributes through thin film thickness in MPEAs, potentially opening avenues for innovative alloy designs spanning diverse applications including soft magnetic materials, rare-earth-free permanent magnets, and magnetocaloric devices.

Numerous unexplored avenues lie in understaing the magnetic properties of MPEAs. A more systematic study starting with three component alloys with two ferromagnetic and one antiferromagnetic element like FeCoMn and FeCoCr can be explored. Structure of these alloys should be studied with extended X-ray absorption fine structure (EXAFS) in conjunction with electron diffraction to study the presence of short-range order by constructing element specific pair distribution functions (PDFs). These structural studies when paired with XAS and XMCD would be able to provide a more detailed understanding of magnetic properties of these two three component MPEAs. It would also shed light on Fe-Fe, Co-Co, Mn-Mn, Cr-Cr, Co-Mn, Fe-Mn, Fe-Cr and Co-Cr magnetic interactions and whether that relates to the short-range order proposed in these materials. Post this detailed study on three component MPEAs, one can move to studying four component FeCoCrMn MPEAs to compare and contrast their properties to three component MPEAs.

For the FeCoCrMnSi based composition which has been reported on in this thesis, mag-

netic ordering of Mn could not be ascertained using XMCD due to its potential antiferromagnetic ordering. Epitaxial thin film samples of MPEA are required to study the response of Mn using x-ray magnetic linear dichroism (XMLD). These XMLD measurements would further improve microscopic magnetic understanding of magnetic exchange between the constituent elements for FeCoCrMnSi based MPEA. We were able to grow epitaxial MPEA films on MgO (001) substrates with limited reproducibility. A seed layer might be needed to grow better epitaxial films with improved reproducibility and better adhesion to substrate. Also, MPEAs grown on (111) oriented substrates could stabilize the h.c.p phase and isolate its magnetic response. Another avenue that can be explored for the FeCoCrMnSi based composition is domain imaging using X-PEEM and correlating it with nano-diffraction which would provided spatial information about f.c.c and h.c.p phases. This would allow one to correlated the element resolved domain imaging from X-PEEM with f.c.c and h.c.p phases.

Exploration of other intriguing compositions like FeCoNiMn, FeCoNiAl, and FeCoNiMnAl holds promise too, spurred by recent theoretical insights by Feng, Qi, and Wang [121] indicating that addition of Mn and Al to MPEAs improves the magnetic properties even though Mn is antiferromagnetic and Al is non-magnetic. This Al induced enhancement is similar to enhancement of magnetization in NdFeB based permanent magnets with addition of Boron [122]. While enhancement of magnetism by addition of Mn could be explained by a change from antiferromagnetic to ferromagnetic ordering, the unexpected enhancement due to addition of Al, attributed to modulation of magnetic system's exchange, warrants experimental substantiation to corroborate the theoretical findings by Feng, Qi, and Wang [121].

Ferrimagnetic materials contain two magnetic sublattices aligned antiparallel, giving a modest net magnetization [123]. This blend of ferromagnetic and antiferromagnetic properties provides advantages for manipulating the net magnetization while benefiting from

antiferromagnetic-like dynamics and applications in high-density devices [124]. Unlike ferro- and antiferromagnets, ferrimagnets permit tuning of the gyromagnetic ratio via temperature or composition, greatly expanding their magnetic properties [125]. The presence of oppositely oriented sublattices also enables studying antiferromagnetic dynamics and spin textures at angular momentum compensation points where exchange stiffness vanishes [125]. Insulating ferrimagnets have found use in microwave technologies due to their low losses. Moreover, rare earth-transition metal ferrimagnets have exhibited all-optical switching, highlighting their appeal for both applications and fundamental physics [28, 126].

As discussed in Section 4.7, the appearance of a ferromagnetic-like phase below the transition temperature denoted as T_F coincides with paramagnetic-to-ferromagnetic transition of chromium (Cr) with antiferromagnetic coupling to iron (Fe) and cobalt (Co). This observation suggests that the MPEA examined in this thesis, below the T_F, exhibits ferrimagnetic behavior. While the MPEA examined here shows ferrimagnetic transition temperature of approximately 200 K, it is conceivable that, within the vast compositional landscape of MPEAs, new candidates for ferrimagnetic materials may be found, possibly featuring compensation points close to room temperature. Such MPEAs hold the potential to facilitate high-density magneto-optical recording, provided a comprehensive understanding of their optical pumping dynamics is achieved, rendering this avenue a captivating prospect for further exploration.

6.2 Ultrafast domain dynamics

The second half of my thesis explores ultrafast domain dynamics in CoFe/Ni multilayers. Our results are in strong support of the theory that extremely fast domain-wall motion can occur in response to ultrafast optical pumping, as previously predicted by Baláž et al. [51]. We show that the spatial distortions of labyrinth domains, in contrast to stripe domains, exhibit a threshold dependence on pump fluence, consistent with mechanisms for domain

wall motion in the presence of pinning sites. In addition, the time-scales associated with the domain distortions are significantly different from the time-scales of the demagnetization. Together, these new results conclusively refute any speculation that the diffraction ring distortions are a trivial extension of ultrafast demagnetization. The prominence of ring distortions for labyrinthine domains, and the correlation of such ring distortions with the motion of curved walls in micromagnetic simulations, is consistent with the hypothesis that curved walls, in particular, are mobile under conditions of ultrafast optical pumping. We show feasible domain wall speeds up to 66 km/s in textured ferromagnets.

Given the homogeneous nature of any ultrafast spin currents that result from uniform optical pumping, domain-wall curvature provides a necessary source of symmetry-breaking required to move walls via spin torque. The unique rates for both ring distortion and ultrafast recovery suggests a more complex mechanism for wall motion than what superdiffusive spin current theory provides. We suggest that THz magnon generation, which is a well documented component of ultrafast demagnetization, and the participation of THz magnons as an additional component of spin current, might explain the unexpected rates for the distortions. Taken in aggregate, these results are supportive of the hypothesis for optically driven ultrafast domain wall motion. Our studies open the possibility of manipulating the ground state to achieve far-from-equilibrium effects at mesoscopic length scales. The implications of such far-from-equilibrium spin kinetics likely extend to understanding and harnessing ultrafast phenomena in quantum materials.

6.2.1 Future Outlook

There still are many unexplored avenues in ultrafast domain dynamics. Further experimental studies are required to find the upper limit of domain speed in CoFe/Ni multilayers using samples grown on more thermally conductive substrates allowing for exploration of higher

pump fluence by increasing the damage threshold. This study would provide further evidence that the domain wall speeds are limited by magnon group velocity.

As discussed in Section 5.2, the FFT analysis used to develop the phenomenological model also yielded two *odd-order* components namely the 1^{st} and 3^{rd} azimuthal harmonics. These odd harmonics are forbidden when thought of from the standpoint of diffraction alone. We speculate that these anomalous components are the combination of the transverse magneto-optic effect in transmission combined with far-field diffraction from domain walls [101]. However, a detailed domain chairality study exploring samples with pure Bloch and Néel domain walls is required to confirm the proposed origin of the forbidden odd harmonics.

Heisenberg exchange, which defines how spins align or anti-align with respect to each other to create ferromagnetic or antiferromagnetic magnetic ordering is defined using the following Hamiltonian [69]:

$$\mathcal{H} = -2\mathcal{J}\left(\hat{\boldsymbol{S}}_1 \cdot \hat{\boldsymbol{S}}_2\right) \tag{6.1}$$

where $\mathcal{J}$ is the exchange constant and $\hat{\boldsymbol{S}}_1$ and $\hat{\boldsymbol{S}}_2$ are spin operators. The key thing to note here is Heisenberg exchange mandates parallel or anti-parallel alignment of spins as the Hamiltonian has a dot product. But Heisenberg exchange fails to explain the weak ferromagnetic moment observed for some antiferromagnetic materials like MnF_2, $MnCO_3$ and αFe_2O_3 [69]. This weak ferromagnetism in antiferromagnets was explained using Dzyaloshinskii–Moriya interaction (DMI) [127, 128] which is represented using the following Hamiltonian:

$$\mathcal{H} = -\mathcal{D} \cdot \left(\hat{\boldsymbol{S}}_1 \times \hat{\boldsymbol{S}}_2\right) \tag{6.2}$$

where $\mathcal{D}$ is a vector defining the high-symmetry axis, $\hat{\boldsymbol{S}}_1$ and $\hat{\boldsymbol{S}}_2$ are spin operators. Due to the cross product in DMI Hamiltonian, materials with DMI tent to favor canting of magnetic moments. It is crucial for generation of topologically protected magnetic symmetries like

skyrmions, bubble domains and chairal domain walls [129]. In thin films and multilayers, DMI can be induced by depositing magnetic material in contact with a material with strong spin-orbit coupling like Pt or Pd. This would give rise to novel magnetic textures especially bubble domains and chairal domain walls, the response of which has not been studied under far-from equilibrium optical excitation and could be one of the potential avenues that can be explored.

The samples studied in this thesis supported labyrinthine and stripe domain morphologies which are not suitable for practical storage devices application. Studies on magnetic racetrack like geometries supporting single domain wall are required to make strides towards practical application of ultrafast domain dynamics in optical control of storage devices. Currently, there are no experimental studies with asymmetric pumping of a sample supporting single domain wall. Direct imaging of domain wall motion can be achieved using MOKE measurement setup similar to the one used by Caretta et al. [110] and pumping the wall with off-center Gaussian beam profile optical pump. Using this experimental setup one can also study spin coherence length by measuring the domain displacement as a function of relative distances between the pump and domain wall. This direct imaging study would provide credence to superdiffusive spin transport hypothesis and provide visual evidence of optically driven domain walls bringing optical control one step closer to application.

Bibliography

[1] Cyril Stanley Smith. *A History of Metallography: The Development of Ideas on the Structure of Metals before 1890*. 1st MIT Press pbk. ed. Cambridge, Mass: MIT Press, 1988. 297 pp. ISBN: 978-0-585-35936-6.

[2] *Mineral Commodity Summaries 2023*. Report 2023. Reston, VA, 2023, p. 210. DOI: 10.3133/mcs2023. URL: http://pubs.er.usgs.gov/publication/mcs2023.

[3] Bradley S. Van Gosen et al. *Rare-Earth Elements*. Report 1802O. Reston, VA, 2017, p. 44. DOI: 10.3133/pp1802O. URL: http://pubs.er.usgs.gov/publication/pp1802O.

[4] Hobart M. King. *REE - Rare Earth Elements and Their Uses*. geology.com. URL: https://geology.com/articles/rare-earth-elements/ (visited on 04/13/2023).

[5] *Global EV Data Explorer – Data Tools*. IEA. URL: https://www.iea.org/data-and-statistics/data-tools/global-ev-data-explorer (visited on 04/13/2023).

[6] *Distribution of Rare Earth Element Consumption Worldwide in 2021, by End Use*. Statista. URL: https://www.statista.com/statistics/604190/distribution-of-rare-earth-element-consumption-worldwide-by-end-use/ (visited on 04/13/2023).

[7] B. Cantor et al. "Microstructural Development in Equiatomic Multicomponent Alloys". In: *Materials Science and Engineering: A* 375–377 (July 2004), pp. 213–218.

ISSN: 09215093. DOI: 10.1016/j.msea.2003.10.257. URL: https://linkinghub.elsevier.com/retrieve/pii/S0921509303009936 (visited on 04/09/2023).

[8] Jien Wei Yeh et al. "Nanostructured High-Entropy Alloys with Multiple Principal Elements: Novel Alloy Design Concepts and Outcomes". In: *Advanced Engineering Materials* 6.5 (2004), pp. 299–303+274. DOI: 10.1002/adem.200300567. pmid: 19533682.

[9] Easo P George, Dierk Raabe, and Robert O Ritchie. "High-Entropy Alloys". In: *Nature Reviews Materials* 4.8 (2019), pp. 515–534. ISSN: 2058-8437. DOI: 10.1038/s41578-019-0121-4. URL: https://doi.org/10.1038/s41578-019-0121-4.

[10] D. B. Miracle and O. N. Senkov. "A Critical Review of High Entropy Alloys and Related Concepts". In: *Acta Materialia* 122 (2017), pp. 448–511. DOI: 10.1016/j.actamat.2016.08.081. pmid: 1000090641. URL: http://dx.doi.org/10.1016/j.actamat.2016.08.081.

[11] K.B. Zhang et al. "Annealing on the Structure and Properties Evolution of the CoCrFeNiCuAl High-Entropy Alloy". In: *Journal of Alloys and Compounds* 502.2 (July 2010), pp. 295–299. ISSN: 09258388. DOI: 10.1016/j.jallcom.2009.11.104. URL: https://linkinghub.elsevier.com/retrieve/pii/S0925838809024104.

[12] Michael C. Gao et al. "High-Entropy Functional Materials". In: *Journal of Materials Research* 33.19 (2018), pp. 3138–3155. ISSN: 0884-2914. DOI: 10.1557/jmr.2018.323. URL: https://www.cambridge.org/core/product/identifier/S0884291418003230/type/journal_article.

[13] Ming-Hung Tsai. "Physical Properties of High Entropy Alloys". In: *Entropy* 15.12 (Dec. 3, 2013), pp. 5338–5345. ISSN: 1099-4300. DOI: 10.3390/e15125338. URL: http://www.mdpi.com/1099-4300/15/12/5338.

[14] Oldřich Schneeweiss et al. “Magnetic Properties of the CrMnFeCoNi High-Entropy Alloy”. In: *Physical Review B* 96.1 (2017), p. 014437. ISSN: 24699969. DOI: 10.1103/PhysRevB.96.014437.

[15] S. Vrtnik et al. “Magnetism of CoCrFeNiZrxeutectic High-Entropy Alloys”. In: *Intermetallics* 93 (October 2017 2018), pp. 122–133. ISSN: 09669795. DOI: 10.1016/j.intermet.2017.11.017.

[16] G. Gong and A. Gupta. “Magnetoresistance and Magnetic Properties of Epitaxial Magnetite Thin Films”. In: *Physical Review B - Condensed Matter and Materials Physics* 56.9 (1997), pp. 5096–5099. ISSN: 1550235X. DOI: 10.1103/PhysRevB.56.5096.

[17] X. H. Liu et al. “Verwey Transition in Fe3O4thin Films: Influence of Oxygen Stoichiometry and Substrate-Induced Microstructure”. In: *Physical Review B - Condensed Matter and Materials Physics* 90.12 (2014), p. 125142. ISSN: 1550235X. DOI: 10.1103/PhysRevB.90.125142.

[18] X. H. Liu, W. Liu, and Z. D. Zhang. “Extremely Low Coercivity in Fe3O4 Thin Film Grown on Mg2TiO4 (001)”. In: *RSC Advances* 7.69 (2017), pp. 43648–43654. ISSN: 20462069. DOI: 10.1039/c7ra08916c.

[19] Robert O. Ritchie. “The Conflicts between Strength and Toughness”. In: *Nature Materials* 10.11 (Nov. 2011), pp. 817–822. ISSN: 1476-1122, 1476-4660. DOI: 10.1038/nmat3115. URL: https://www.nature.com/articles/nmat3115 (visited on 04/17/2023).

[20] Yujie Wei et al. “Evading the Strength–Ductility Trade-off Dilemma in Steel through Gradient Hierarchical Nanotwins”. In: *Nature Communications* 5.1 (Apr. 1, 2014), p. 3580. ISSN: 2041-1723. DOI: 10.1038/ncomms4580. URL: https://www.nature.com/articles/ncomms4580 (visited on 04/17/2023).

[21] Zhiming Li et al. “Metastable High-Entropy Dual-Phase Alloys Overcome the Strength–Ductility Trade-Off”. In: *Nature* 534.7606 (June 9, 2016), pp. 227–230. ISSN: 0028-0836, 1476-4687. DOI: 10.1038/nature17981. pmid: 27279217. URL: https://www.nature.com/articles/nature17981.

[22] John Jumper et al. “Highly Accurate Protein Structure Prediction with AlphaFold”. In: *Nature* 596.7873 (Aug. 26, 2021), pp. 583–589. ISSN: 0028-0836, 1476-4687. DOI: 10.1038/s41586-021-03819-2. URL: https://www.nature.com/articles/s41586-021-03819-2 (visited on 06/05/2023).

[23] M. N. Baibich et al. “Giant Magnetoresistance of (001)Fe/(001)Cr Magnetic Superlattices”. In: *Physical Review Letters* 61.21 (Nov. 21, 1988), pp. 2472–2475. ISSN: 0031-9007. DOI: 10.1103/PhysRevLett.61.2472. URL: https://link.aps.org/doi/10.1103/PhysRevLett.61.2472 (visited on 07/29/2023).

[24] Spencer Jeppson and Roopali Kukreja. “Capturing Ultrafast Magnetization Phenomenon Using Femtosecond x Rays”. In: *APL Materials* 9.10 (Oct. 1, 2021), p. 100702. ISSN: 2166-532X. DOI: 10.1063/5.0054006. URL: https://doi.org/10.1063/5.0054006.

[25] E. Beaurepaire et al. “Ultrafast Spin Dynamics in Ferromagnetic Nickel”. In: *Physical Review Letters* 76.22 (May 27, 1996), pp. 4250–4253. ISSN: 0031-9007, 1079-7114. DOI: 10.1103/PhysRevLett.76.4250. pmid: 10061239. URL: https://link.aps.org/doi/10.1103/PhysRevLett.76.4250.

[26] *Hard Drives Methods And Materials | Ismail-Beigi Research Group*. URL: https://volga.eng.yale.edu/teaching-resources/hard-drives/methods-and-materials (visited on 06/04/2023).

[27] J.R. Szedon and T.L. Chu. “Tunnel Inspection and Trapping of Electrons in Aluminum-Silicon Nitride-Silicon Dioxide-Silicon (MNOS) Capacitors”. In: *IEEE Transactions*

on Electron Devices 14.9 (Sept. 1967), pp. 631–631. ISSN: 0018-9383. DOI: 10.1109/T-ED.1967.16053. URL: http://ieeexplore.ieee.org/document/1474776/ (visited on 06/04/2023).

[28] C. D. Stanciu et al. "All-Optical Magnetic Recording with Circularly Polarized Light". In: *Physical Review Letters* 99.4 (July 25, 2007), p. 047601. ISSN: 0031-9007, 1079-7114. DOI: 10.1103/PhysRevLett.99.047601. URL: https://link.aps.org/doi/10.1103/PhysRevLett.99.047601 (visited on 06/05/2023).

[29] K. Vahaplar et al. "All-Optical Magnetization Reversal by Circularly Polarized Laser Pulses: Experiment and Multiscale Modeling". In: *Physical Review B* 85.10 (Mar. 6, 2012), p. 104402. ISSN: 1098-0121, 1550-235X. DOI: 10.1103/PhysRevB.85.104402. URL: https://link.aps.org/doi/10.1103/PhysRevB.85.104402 (visited on 06/12/2023).

[30] S. Mangin et al. "Engineered Materials for All-Optical Helicity-Dependent Magnetic Switching". In: *Nature Materials* 13.3 (Mar. 2014), pp. 286–292. ISSN: 1476-1122, 1476-4660. DOI: 10.1038/nmat3864. URL: https://www.nature.com/articles/nmat3864 (visited on 06/05/2023).

[31] M. L. M. Lalieu, R. Lavrijsen, and B. Koopmans. "Integrating All-Optical Switching with Spintronics". In: *Nature Communications* 10.1 (Jan. 10, 2019), p. 110. ISSN: 2041-1723. DOI: 10.1038/s41467-018-08062-4. URL: https://www.nature.com/articles/s41467-018-08062-4 (visited on 06/12/2023).

[32] L. Avilés-Félix et al. "Single-Shot All-Optical Switching of Magnetization in Tb/Co Multilayer-Based Electrodes". In: *Scientific Reports* 10.1 (Mar. 23, 2020), p. 5211. ISSN: 2045-2322. DOI: 10.1038/s41598-020-62104-w. URL: https://www.nature.com/articles/s41598-020-62104-w (visited on 06/12/2023).

[33] C.S. Davies et al. “Pathways for Single-Shot All-Optical Switching of Magnetization in Ferrimagnets”. In: *Physical Review Applied* 13.2 (Feb. 24, 2020), p. 024064. ISSN: 2331-7019. DOI: 10.1103/PhysRevApplied.13.024064. URL: https://link.aps.org/doi/10.1103/PhysRevApplied.13.024064 (visited on 06/12/2023).

[34] C. Banerjee et al. “Single Pulse All-Optical Toggle Switching of Magnetization without Gadolinium in the Ferrimagnet Mn2RuxGa”. In: *Nature Communications* 11.1 (Sept. 7, 2020), p. 4444. ISSN: 2041-1723. DOI: 10.1038/s41467-020-18340-9. URL: https://www.nature.com/articles/s41467-020-18340-9 (visited on 06/12/2023).

[35] C.S. Davies et al. “Helicity-Independent All-Optical Switching of Magnetization in Ferrimagnetic Alloys”. In: *Journal of Magnetism and Magnetic Materials* 563 (Dec. 2022), p. 169851. ISSN: 03048853. DOI: 10.1016/j.jmmm.2022.169851. URL: https://linkinghub.elsevier.com/retrieve/pii/S0304885322007405 (visited on 06/12/2023).

[36] Peiyao Zhang et al. “All-Optical Switching of Magnetization in Atomically Thin CrI3”. In: *Nature Materials* 21.12 (Dec. 2022), pp. 1373–1378. ISSN: 1476-1122, 1476-4660. DOI: 10.1038/s41563-022-01354-7. URL: https://www.nature.com/articles/s41563-022-01354-7 (visited on 06/12/2023).

[37] B. D. Cullity and C. D. Graham. *Introduction to Magnetic Materials*. 2008. ISBN: 978-0-471-47741-9. DOI: 10.1002/9780470386323.

[38] Andrei Kirilyuk, Alexey V Kimel, and Theo Rasing. “Laser-Induced Magnetization Dynamics and Reversal in Ferrimagnetic Alloys”. In: *Reports on Progress in Physics* 76.2 (Feb. 1, 2013), p. 026501. ISSN: 0034-4885, 1361-6633. DOI: 10.1088/0034-4885/76/2/026501. URL: https://iopscience.iop.org/article/10.1088/0034-4885/76/2/026501 (visited on 03/02/2023).

[39] Marco Battiato, Karel Carva, and Peter M Oppeneer. "Superdiffusive Spin Transport as a Mechanism of Ultrafast Demagnetization". In: *Physical Review Letters* 105.2 (2010), p. 27203. URL: https://journals.aps.org/prl/abstract/10.1103/PhysRevLett.105.027203.

[40] Michael Haag, Christian Illg, and Manfred Fähnle. "Role of Electron-Magnon Scatterings in Ultrafast Demagnetization". In: *Physical Review B* 90.1 (July 15, 2014), p. 014417. ISSN: 1098-0121, 1550-235X. DOI: 10.1103/PhysRevB.90.014417. URL: https://link.aps.org/doi/10.1103/PhysRevB.90.014417 (visited on 07/28/2023).

[41] E. Carpene et al. "Dynamics of Electron-Magnon Interaction and Ultrafast Demagnetization in Thin Iron Films". In: *Physical Review B* 78.17 (Nov. 20, 2008), p. 174422. ISSN: 1098-0121, 1550-235X. DOI: 10.1103/PhysRevB.78.174422. URL: https://link.aps.org/doi/10.1103/PhysRevB.78.174422 (visited on 07/28/2023).

[42] B. Koopmans et al. "Explaining the Paradoxical Diversity of Ultrafast Laser-Induced Demagnetization". In: *Nature Materials* 9.3 (Mar. 2010), pp. 259–265. ISSN: 1476-1122, 1476-4660. DOI: 10.1038/nmat2593. URL: https://www.nature.com/articles/nmat2593 (visited on 07/29/2023).

[43] B. Koopmans et al. "Unifying Ultrafast Magnetization Dynamics". In: *Physical Review Letters* 95.26 (Dec. 27, 2005), p. 267207. ISSN: 0031-9007, 1079-7114. DOI: 10.1103/PhysRevLett.95.267207. URL: https://link.aps.org/doi/10.1103/PhysRevLett.95.267207 (visited on 09/04/2023).

[44] Vincent Cardin et al. "Wavelength Scaling of Ultrafast Demagnetization in Co/Pt Multilayers". In: *Physical Review B* 101.5 (Feb. 21, 2020), p. 054430. ISSN: 2469-9950, 2469-9969. DOI: 10.1103/PhysRevB.101.054430. URL: https://link.aps.org/doi/10.1103/PhysRevB.101.054430 (visited on 08/09/2023).

[45] S. R. Tauchert et al. “Polarized Phonons Carry Angular Momentum in Ultrafast Demagnetization”. In: *Nature* 602.7895 (2022), pp. 73–77. ISSN: 14764687. DOI: 10.1038/s41586-021-04306-4. pmid: 35110761.

[46] M. Battiato, K. Carva, and P. M. Oppeneer. “Theory of Laser-Induced Ultrafast Superdiffusive Spin Transport in Layered Heterostructures”. In: *Physical Review B* 86.2 (July 5, 2012), p. 024404. ISSN: 1098-0121, 1550-235X. DOI: 10.1103/PhysRevB.86.024404. URL: https://link.aps.org/doi/10.1103/PhysRevB.86.024404 (visited on 07/30/2023).

[47] Dennis Rudolf et al. “Ultrafast Magnetization Enhancement in Metallic Multilayers Driven by Superdiffusive Spin Current”. In: *Nature Communications* 3.1 (Sept. 4, 2012), p. 1037. ISSN: 2041-1723. DOI: 10.1038/ncomms2029. URL: https://www.nature.com/articles/ncomms2029 (visited on 07/30/2023).

[48] Stefan Mathias et al. “Probing the Timescale of the Exchange Interaction in a Ferromagnetic Alloy”. In: *Proceedings of the National Academy of Sciences* 109.13 (Mar. 27, 2012), pp. 4792–4797. ISSN: 0027-8424, 1091-6490. DOI: 10.1073/pnas.1201371109. URL: https://pnas.org/doi/full/10.1073/pnas.1201371109 (visited on 07/30/2023).

[49] Emrah Turgut et al. “Controlling the Competition between Optically Induced Ultrafast Spin-Flip Scattering and Spin Transport in Magnetic Multilayers”. In: *Physical Review Letters* 110.19 (May 7, 2013), p. 197201. ISSN: 0031-9007, 1079-7114. DOI: 10.1103/PhysRevLett.110.197201. URL: https://link.aps.org/doi/10.1103/PhysRevLett.110.197201 (visited on 07/30/2023).

[50] A. J. Schellekens et al. “Investigating the Contribution of Superdiffusive Transport to Ultrafast Demagnetization of Ferromagnetic Thin Films”. In: *Applied Physics Letters* 102.25 (June 24, 2013), p. 252408. ISSN: 0003-6951, 1077-3118. DOI: 10.1063/

1 . 4812658. URL: https : / / pubs . aip . org / apl / article / 102 / 25 / 252408 / 129268 / Investigating-the-contribution-of-superdiffusive (visited on 08/09/2023).

[51] Pavel Baláž et al. "Domain Wall Dynamics Due to Femtosecond Laser-Induced Superdiffusive Spin Transport". In: *Physical Review B* 101.17 (May 14, 2020), p. 174418. ISSN: 2469-9950. DOI: 10.1103/PhysRevB.101.174418. URL: https://link.aps.org/doi/10.1103/PhysRevB.101.174418.

[52] Laura J. Heyderman et al. "Mesoscopic Magnetic Systems: From Fundamental Properties to Devices". In: *Applied Physics Letters* 119.8 (2021), p. 080401. DOI: 10.1063/5.0064083. URL: https://aip.scitation.org/doi/abs/10.1063/5.0064083.

[53] Stuart S. P. Parkin, Masamitsu Hayashi, and Luc Thomas. "Magnetic Domain-Wall Racetrack Memory". In: *Science* 320.5873 (Apr. 11, 2008), pp. 190–194. ISSN: 0036-8075. DOI: 10.1126/science.1145799. URL: https://www.science.org/doi/10.1126/science.1145799.

[54] Lucas Caretta et al. "Fast Current-Driven Domain Walls and Small Skyrmions in a Compensated Ferrimagnet". In: *Nature Nanotechnology* 13.12 (2018), pp. 1154–1160. ISSN: 1748-3395. DOI: 10.1038/s41565-018-0255-3. URL: https://doi.org/10.1038/s41565-018-0255-3.

[55] A. Manchon et al. "Current-Induced Spin-Orbit Torques in Ferromagnetic and Antiferromagnetic Systems". In: *Reviews of Modern Physics* 91.3 (2019), p. 035004. DOI: 10.1103/RevModPhys.91.035004. URL: https://link.aps.org/doi/10.1103/RevModPhys.91.035004.

[56] Ilya Prigogine. "Time, Structure and Fluctuations". In: *Nobel Lectures, Chemistry 1971-1980*. Ed. by Tore Frängsmyr and Sture Forsén. Singapore: World Scientific

Publishing Co., 1993. URL: https://www.nobelprize.org/prizes/chemistry/1977/prigogine/lecture/.

[57] J Hemminger, G Fleming, and M Ratner. *Directing Matter and Energy: Five Challenges for Science and the Imagination*. 935427. U.S. Department of Energy, Dec. 20, 2007, p. 935427. DOI: 10.2172/935427. URL: http://www.osti.gov/servlets/purl/935427/ (visited on 02/28/2023).

[58] Erlend G. Tveten, Arne Brataas, and Yaroslav Tserkovnyak. "Electron-Magnon Scattering in Magnetic Heterostructures Far out of Equilibrium". In: *Physical Review B* 92.18 (2015), p. 180412. DOI: 10.1103/PhysRevB.92.180412. URL: https://link.aps.org/doi/10.1103/PhysRevB.92.180412.

[59] Frances Hellman et al. "Interface-Induced Phenomena in Magnetism". In: *Reviews of Modern Physics* 89.2 (June 2017), p. 25006. ISSN: 0034-6861, 1539-0756. DOI: 10.1103/RevModPhys.89.025006. URL: http://link.aps.org/doi/10.1103/RevModPhys.89.025006.

[60] Hermann Dürr. "The X-ray View of Ultrafast Magnetism". In: *Synchrotron Light Sources and Free-Electron Lasers: Accelerator Physics, Instrumentation and Science Applications*. Ed. by Eberhard J. Jaeschke et al. Cham: Springer International Publishing, 2020, pp. 2115–2130. ISBN: 978-3-030-23201-6. DOI: 10.1007/978-3-030-23201-6_50. URL: https://doi.org/10.1007/978-3-030-23201-6_50.

[61] A.M. Kosevich, B.A. Ivanov, and A.S. Kovalev. "Magnetic Solitons". In: *Physics Reports* 194.3-4 (Oct. 1990), pp. 117–238. ISSN: 03701573. DOI: 10.1016/0370-1573(90)90130-T. URL: https://linkinghub.elsevier.com/retrieve/pii/037015739090130T (visited on 05/30/2023).

[62] N. L. Schryer and L. R. Walker. "The Motion of 180° Domain Walls in Uniform Dc Magnetic Fields". In: *Journal of Applied Physics* 45.12 (1974), pp. 5406–5421. DOI: 10.1063/1.1663252. URL: https://aip.scitation.org/doi/abs/10.1063/1.1663252.

[63] Jacques Ferré et al. "Universal Magnetic Domain Wall Dynamics in the Presence of Weak Disorder". In: *Comptes Rendus Physique* 14.8 (2013), pp. 651–666. ISSN: 1631-0705. DOI: 10.1016/j.crhy.2013.08.001. URL: https://www.sciencedirect.com/science/article/pii/S1631070513001291.

[64] B. Pfau et al. "Ultrafast Optical Demagnetization Manipulates Nanoscale Spin Structure in Domain Walls". In: *Nature Communications* 3.1 (Jan. 2, 2012), p. 1100. ISSN: 2041-1723. DOI: 10.1038/ncomms2108. URL: http://www.nature.com/articles/ncomms2108.

[65] Dmitriy Zusin et al. "Ultrafast Perturbation of Magnetic Domains by Optical Pumping in a Ferromagnetic Multilayer". In: *Physical Review B* 106.14 (Oct. 19, 2022), p. 144422. ISSN: 2469-9950. DOI: 10.1103/PhysRevB.106.144422. arXiv: 2001.11719. URL: https://doi.org/10.1103/PhysRevB.106.144422.

[66] Nanna Zhou Hagström et al. "Symmetry-Dependent Ultrafast Manipulation of Nanoscale Magnetic Domains". In: *Physical Review B* 106.22 (Dec. 23, 2022), p. 224424. ISSN: 2469-9950, 2469-9969. DOI: 10.1103/PhysRevB.106.224424. URL: https://link.aps.org/doi/10.1103/PhysRevB.106.224424 (visited on 06/04/2023).

[67] Boris Vodungbo et al. "Laser-Induced Ultrafast Demagnetization in the Presence of a Nanoscale Magnetic Domain Network". In: *Nature Communications* 3.1 (Jan. 14, 2012), p. 999. ISSN: 2041-1723. DOI: 10.1038/ncomms2007. URL: http://www.nature.com/articles/ncomms2007.

[68] Joseph I. Goldstein et al. *Scanning Electron Microscopy and X-Ray Microanalysis*. New York, NY: Springer New York, 2018. ISBN: 978-1-4939-6674-5 978-1-4939-6676-9. DOI: 10.1007/978-1-4939-6676-9. URL: https://link.springer.com/10.1007/978-1-4939-6676-9 (visited on 07/23/2023).

[69] J. M. D. Coey. *Magnetism and Magnetic Materials*. Cambridge: Cambridge University Press, 2010. 614 pp. ISBN: 978-0-521-81614-4. DOI: 10.1017/CBO9780511845000. URL: https://www.cambridge.org/core/books/magnetism-and-magnetic-materials/AD3557E2D4538CAA8488A8C1057313BC.

[70] W. C. Röntgen. "Ueber eine neue Art von Strahlen". In: *Annalen der Physik* 300.1 (1898), pp. 1–11. ISSN: 00033804, 15213889. DOI: 10.1002/andp.18983000102. URL: https://onlinelibrary.wiley.com/doi/10.1002/andp.18983000102 (visited on 05/04/2023).

[71] Eberhard Jaeschke. *Synchrotron Light Sources and Free-Electron Lasers: Accelerator Physics, Instrumentation and Science Applications*. New York, NY: Springer Berlin Heidelberg, 2016. ISBN: 978-3-319-14393-4. DOI: 10.1007/978-3-319-14394-1. URL: https://link.springer.com/10.1007/978-3-319-14394-1 (visited on 04/10/2023).

[72] *Philips XRD: X-ray Tube – Kurt Hollocher*. Philips XRD: X-ray Tube. URL: https://muse.union.edu/hollochk/the-x-ray-tube/ (visited on 05/05/2023).

[73] Andreas Maier et al., eds. *Medical Imaging Systems: An Introductory Guide*. Vol. 11111. Lecture Notes in Computer Science. Cham: Springer Open, 2018. 264 pp. ISBN: 978-3-319-96519-2. DOI: 10.1007/978-3-319-96520-8. URL: http://link.springer.com/10.1007/978-3-319-96520-8 (visited on 05/05/2023).

[74] Phil Willmott. *An Introduction to Synchrotron Radiation: Techniques and Applications*. Second edition. Hoboken, New Jersey: Wiley, 2019. 1 p. ISBN: 978-1-119-28039-

2. DOI: 10.1002/9781119280453. URL: https://onlinelibrary.wiley.com/doi/book/10.1002/9781119280453 (visited on 05/07/2023).

[75] H. C. Pollock. "Combination of Betatron and Synchrotron for Electron Acceleration". In: *Physical Review* 69.3-4 (Feb. 1, 1946), pp. 125–125. ISSN: 0031-899X. DOI: 10.1103/PhysRev.69.125. URL: https://link.aps.org/doi/10.1103/PhysRev.69.125 (visited on 05/05/2023).

[76] F. R. Elder et al. "Radiation from Electrons in a Synchrotron". In: *Physical Review* 71.11 (June 1, 1947), pp. 829–830. ISSN: 0031-899X. DOI: 10.1103/PhysRev.71.829.5. URL: https://link.aps.org/doi/10.1103/PhysRev.71.829.5 (visited on 05/05/2023).

[77] *X-Ray Free Electron Lasers: A Revolution in Structural Biology*. New York, NY: Springer Science+Business Media, 2018. ISBN: 978-3-030-00550-4 978-3-030-00551-1. DOI: 10.1007/978-3-030-00551-1. URL: http://link.springer.com/10.1007/978-3-030-00551-1 (visited on 05/11/2023).

[78] Anatoly Shabalin. "Coherent X-ray Diffraction Studies of Mesoscopic Materials". PhD thesis. Hamburg: University of Hamburg, 2015. 135 pp. URL: https://bib-pubdb1.desy.de/record/291304/files/Dissertation_AnatolyShabalin.pdf.

[79] Sébastien Boutet, Petra Fromme, and Mark S. Hunter, eds. *X-Ray Free Electron Lasers: A Revolution in Structural Biology*. Cham: Springer International Publishing, 2018. ISBN: 978-3-030-00550-4 978-3-030-00551-1. DOI: 10.1007/978-3-030-00551-1. URL: http://link.springer.com/10.1007/978-3-030-00551-1 (visited on 07/22/2023).

[80] Dmitriy Zusin. "Ultrafast Dynamics of Magnetic Multilayer Films: Magneto-Optical Spectroscopy and Resonant Scattering in the Extreme Ultraviolet and Soft X-ray Spectral Regions". PhD thesis. Boulder: University of Colorado Boulder, 2018. URL: https://scholar.colorado.edu/concern/graduate_thesis_or_dissertations/k35694421.

[81] R. Bonifacio, C. Pellegrini, and L.M. Narducci. "Collective Instabilities and High-Gain Regime in a Free Electron Laser". In: *Optics Communications* 50.6 (July 1984), pp. 373–378. ISSN: 00304018. DOI: 10.1016/0030-4018(84)90105-6. URL: https://linkinghub.elsevier.com/retrieve/pii/0030401884901056 (visited on 05/20/2023).

[82] Joachim Stöhr. *The Nature of X-Rays and Their Interactions with Matter*. Vol. 288. Springer Tracts in Modern Physics. Cham: Springer International Publishing, 2023. ISBN: 978-3-031-20743-3 978-3-031-20744-0. DOI: 10.1007/978-3-031-20744-0. URL: https://link.springer.com/10.1007/978-3-031-20744-0 (visited on 07/24/2023).

[83] Joachim Stöhr and Hans Christoph Siegmann. *Magnetism: From Fundamentals to Nanoscale Dynamics*. Springer, 2006. ISBN: 978-3-540-30283-4. DOI: 10.1007/978-3-540-30283-4.

[84] Cy M. Jeffries et al. "Small-Angle X-ray and Neutron Scattering". In: *Nature Reviews Methods Primers* 1.1 (Oct. 12, 2021), p. 70. ISSN: 2662-8449. DOI: 10.1038/s43586-021-00064-9. URL: https://www.nature.com/articles/s43586-021-00064-9 (visited on 07/04/2023).

[85] O. Hellwig et al. "X-Ray Studies of Aligned Magnetic Stripe Domains in Perpendicular Multilayers". In: *Physica B: Condensed Matter* 336.1-2 (Aug. 2003), pp. 136–144. ISSN: 09214526. DOI: 10.1016/S0921-4526(03)00282-5. URL: https://linkinghub.elsevier.com/retrieve/pii/S0921452603002825 (visited on 07/02/2023).

[86] Bob B. He. *Two-Dimensional X-ray Diffraction*. 2nd ed. Hoboken, NJ, USA: J. Wiley, 2018. ISBN: 978-1-119-35608-0. DOI: 10.1002/9781119356080. URL: http://doi.wiley.com/10.1002/9781119356080 (visited on 05/27/2023).

[87] Alevtina Smekhova et al. "Local Structure and Magnetic Properties of a Nanocrystalline Mn-rich Cantor Alloy Thin Film down to the Atomic Scale". In: *Nano Research*

16.4 (Apr. 2023), pp. 5626–5639. ISSN: 1998-0124, 1998-0000. DOI: 10.1007/s12274-022-5135-3. URL: https://link.springer.com/10.1007/s12274-022-5135-3 (visited on 05/27/2023).

[88] Rahul Jangid, Kenneth B. Ainslie, and Roopali Kukreja. "Structural and Magnetic Properties of FeCoMnCrSi Multi-Principal Alloy". In: *Journal of Materials Research* 35.8 (2020), pp. 981–989. ISSN: 20445326. DOI: 10.1557/jmr.2019.405.

[89] J. a. Mydosh. *Spin Glasses: An Experimental Introduction*. Washington DC, 1993. ISBN: 0-7484-0038-9. URL: http://books.google.com/books?id=lRpmQgAACAAJ&pgis=1.

[90] Joseph J. Becker. "Surface Effects on Hysteresis Loop Shapes in High-Coercive-Force Crystallized Amorphous Alloys." In: *IEEE Transactions on Magnetics* Mag-18.6 (1982), pp. 1451–1453. ISSN: 00189464. DOI: 10.1109/TMAG.1982.1061969.

[91] Paul A. Beck. "Comments on Mictomagnetism". In: *Journal of The Less-Common Metals* 28.1 (1972), pp. 193–199. ISSN: 00225088. DOI: 10.1016/0022-5088(72)90180-4.

[92] Pampa Pal, A. K. Majumdar, and A. K. Nigam. "Probing Exotic Magnetic Phases and Electrical Transport in Cr-rich -NiFeCr Alloys". In: *Journal of Magnetism and Magnetic Materials* 381 (2015), pp. 297–309. ISSN: 03048853. DOI: 10.1016/j.jmmm.2015.01.006. URL: http://dx.doi.org/10.1016/j.jmmm.2015.01.006.

[93] J. A. Mydosh. "Spin Glasses: Redux: An Updated Experimental/Materials Survey". In: *Reports on Progress in Physics* 78.5 (2015), p. 052501. ISSN: 00344885. DOI: 10.1088/0034-4885/78/5/052501. pmid: 25872613.

[94] K. Binder and A. P. Young. "Spin Glasses: Experimental Facts, Theoretical Concepts, and Open Questions". In: *Reviews of Modern Physics* 58.4 (1986), pp. 801–976. ISSN: 00346861. DOI: 10.1103/RevModPhys.58.801.

[95] Senoussi, S. "Irreversible Effects in Aug81Fe19 and Ni79Mn 21 below the de Almeida-Thouless Temperature". In: *J. Phys. France* 45.2 (1984), pp. 315–322. DOI: 10.1051/jphys:01984004502031500. URL: https://doi.org/10.1051/jphys:01984004502031500.

[96] F. Boakye and K.G. Adanu. "The Néel Temperature of -Mn Thin Films". In: *Thin Solid Films* 279.1-2 (June 1996), pp. 29–33. ISSN: 00406090. DOI: 10.1016/0040-6090(95)08118-6. URL: https://linkinghub.elsevier.com/retrieve/pii/0040609095081186 (visited on 07/10/2023).

[97] C. Kittel. "Note on the Inertia and Damping Constant of Ferromagnetic Domain Boundaries". In: *Physical Review* 80.5 (1950), pp. 918–918. DOI: 10.1103/PhysRev.80.918. URL: https://link.aps.org/doi/10.1103/PhysRev.80.918.

[98] J. Rhensius et al. "Imaging of Domain Wall Inertia in Permalloy Half-Ring Nanowires by Time-Resolved Photoemission Electron Microscopy". In: *Physical Review Letters* 104.6 (2010), p. 067201. DOI: 10.1103/PhysRevLett.104.067201. URL: https://link.aps.org/doi/10.1103/PhysRevLett.104.067201.

[99] N. D. Rizzo, T. J. Silva, and A. B. Kos. "Relaxation Times for Magnetization Reversal in a High Coercivity Magnetic Thin Film". In: *Physical Review Letters* 83.23 (1999), pp. 4876–4879.

[100] Yuyan Liu et al. "Simple Empirical Analytical Approximation to the Voigt Profile". In: *Journal of the Optical Society of America B* 18.5 (May 1, 2001), p. 666. ISSN: 0740-3224, 1520-8540. DOI: 10.1364/JOSAB.18.000666. URL: https://opg.optica.org/abstract.cfm?URI=josab-18-5-666 (visited on 05/01/2023).

[101] Rahul Jangid et al. *Evidence of Extreme Domain Wall Speeds under Ultrafast Optical Excitation*. Apr. 27, 2023. arXiv: 2303.16131 [cond-mat]. URL: http://arxiv.org/abs/2303.16131 (visited on 06/05/2023). preprint.

[102] T. Sant et al. "Measurements of Ultrafast Spin-Profiles and Spin-Diffusion Properties in the Domain Wall Area at a Metal/Ferromagnetic Film Interface". In: *Scientific Reports* 7.1 (Nov. 8, 2017), p. 15064. ISSN: 2045-2322. DOI: 10.1038/s41598-017-15234-7. pmid: 29118451. URL: https://www.nature.com/articles/s41598-017-15234-7.

[103] S. Valencia et al. "Faraday Rotation Spectra at Shallow Core Levels: 3 p Edges of Fe, Co, and Ni". In: *New Journal of Physics* 8.10 (Oct. 25, 2006), pp. 254–254. ISSN: 1367-2630. DOI: 10.1088/1367-2630/8/10/254. URL: https://iopscience.iop.org/article/10.1088/1367-2630/8/10/254.

[104] J. B. Kortright, M. Rice, and R. Carr. "Soft-x-Ray Faraday Rotation at Fe L2,3 Edges". In: *Physical Review B* 51.15 (1995), pp. 10240–10243. DOI: 10.1103/PhysRevB.51.10240. URL: http://dx.doi.org/10.1103/PhysRevB.51.10240.

[105] Vivek Unikandanunni et al. "Anisotropic Ultrafast Spin Dynamics in Epitaxial Cobalt". In: *Applied Physics Letters* 118.23 (2021), p. 232404. ISSN: 0003-6951. DOI: 10.1063/5.0049692. arXiv: 2008.03119.

[106] M. Hennes et al. "Laser-Induced Ultrafast Demagnetization and Perpendicular Magnetic Anisotropy Reduction in a Co 88 Tb 12 Thin Film with Stripe Domains". In: *Physical Review B* 102.17 (Nov. 24, 2020), p. 174437. ISSN: 2469-9950, 2469-9969. DOI: 10.1103/PhysRevB.102.174437. URL: https://link.aps.org/doi/10.1103/PhysRevB.102.174437 (visited on 07/14/2023).

[107] Arne Vansteenkiste et al. “The Design and Verification of MuMax3”. In: *AIP Advances* 4.10, 107133 (2014), p. 107133. DOI: http://dx.doi.org/10.1063/1.4899186. URL: http://scitation.aip.org/content/aip/journal/adva/4/10/10.1063/1.4899186.

[108] Justin M. Shaw, Hans T. Nembach, and T. J. Silva. “Measurement of Orbital Asymmetry and Strain in Co Fe /Ni Multilayers and Alloys: Origins of Perpendicular Anisotropy”. In: *Physical Review B* 87.5 (Feb. 2013), p. 054416. DOI: 10.1103/PhysRevB.87.054416. URL: https://link.aps.org/doi/10.1103/PhysRevB.87.054416.

[109] E. Iacocca et al. “Spin-Current-Mediated Rapid Magnon Localisation and Coalescence after Ultrafast Optical Pumping of Ferrimagnetic Alloys”. In: *Nature Communications* 10.1 (Dec. 15, 2019), p. 1756. ISSN: 2041-1723. DOI: 10.1038/s41467-019-09577-0. URL: http://www.nature.com/articles/s41467-019-09577-0.

[110] Lucas Caretta et al. “Relativistic Kinematics of a Magnetic Soliton”. In: *Science* 370.6523 (Dec. 18, 2020), pp. 1438–1442. ISSN: 0036-8075, 1095-9203. DOI: 10.1126/science.aba5555. URL: https://www.science.org/doi/10.1126/science.aba5555 (visited on 02/27/2023).

[111] H. A. Mook and D Mck Paul. “Neutron-Scattering Measurement of the Spin-Wave Spectra for Nickel”. In: *Physical Review Letters* 54.3 (Jan. 21, 1985), pp. 227–229. ISSN: 0031-9007. DOI: 10.1103/PhysRevLett.54.227. URL: https://link.aps.org/doi/10.1103/PhysRevLett.54.227.

[112] A. Axelevitch, B. Gorenstein, and G. Golan. “Investigation of Optical Transmission in Thin Metal Films”. In: *Physics Procedia* 32 (2012), pp. 1–13. ISSN: 1875-3892. DOI: 10.1016/j.phpro.2012.03.510. URL: https://www.sciencedirect.com/science/article/pii/S1875389212009273.

[113] Y. Zhang et al. “Relaxation Time of Terahertz Magnons Excited at Ferromagnetic Surfaces”. In: *Physical Review Letters* 109 (2012), p. 087203. DOI: 10.1103/PhysRevLett.109.087203. URL: http://link.aps.org/doi/10.1103/PhysRevLett.109.087203%20http://dx.doi.org/10.1103/PhysRevLett.109.087203.

[114] Khalil Zakeri. “Elementary Spin Excitations in Ultrathin Itinerant Magnets”. In: *Physics Reports* 545.2 (2014), pp. 47–93. ISSN: 03701573. DOI: 10.1016/j.physrep.2014.08.001. URL: http://dx.doi.org/10.1016/j.physrep.2014.08.001.

[115] Mohamed F. Elhanoty et al. “Element-Selective Ultrafast Magnetization Dynamics of Hybrid Stoner-Heisenberg Magnets”. In: *Physical Review B* 105.10 (2022), p. L100401. DOI: 10.1103/PhysRevB.105.L100401. URL: https://link.aps.org/doi/10.1103/PhysRevB.105.L100401.

[116] Gyung-Min Choi et al. “Spin Current Generated by Thermally Driven Ultrafast Demagnetization”. In: *Nature Communications* 5.1 (2014), p. 4334. ISSN: 2041-1723. DOI: 10.1038/ncomms5334. URL: https://doi.org/10.1038/ncomms5334.

[117] Emrah Turgut et al. “Stoner versus Heisenberg: Ultrafast Exchange Reduction and Magnon Generation during Laser-Induced Demagnetization”. In: *Physical Review B* 94.22 (2016), p. 220408. URL: http://link.aps.org/doi/10.1103/PhysRevB.94.220408.

[118] R. Knut et al. *Inhomogeneous Magnon Scattering during Ultrafast Demagnetization*. Oct. 25, 2018. arXiv: 1810.10994 [cond-mat]. URL: http://arxiv.org/abs/1810.10994 (visited on 06/04/2023). preprint.

[119] M. Beens, R. A. Duine, and B. Koopmans. “s-d Model for Local and Nonlocal Spin Dynamics in Laser-Excited Magnetic Heterostructures”. In: *Physical Review B* 102.5 (2020), p. 054442. DOI: 10.1103/PhysRevB.102.054442. URL: https://link.aps.org/doi/10.1103/PhysRevB.102.054442.

[120] Cyril Léveillé et al. “Ultrafast Time-Evolution of Chiral Néel Magnetic Domain Walls Probed by Circular Dichroism in x-Ray Resonant Magnetic Scattering”. In: *Nature Communications* 13.1 (Dec. 17, 2022), p. 1412. ISSN: 2041-1723. DOI: 10.1038/s41467-022-28899-0. URL: https://www.nature.com/articles/s41467-022-28899-0.

[121] Wenqiang Feng, Yang Qi, and Shaoqing Wang. “Effects of Mn and Al Addition on Structural and Magnetic Properties of FeCoNi-based High Entropy Alloys”. In: *Materials Research Express* 5.10 (Aug. 24, 2018), p. 106511. ISSN: 2053-1591. DOI: 10.1088/2053-1591/aadaa7. URL: https://iopscience.iop.org/article/10.1088/2053-1591/aadaa7 (visited on 08/15/2023).

[122] R. Skomski. “Permanent Magnets: History, Current Research, and Outlook”. In: *Novel Functional Magnetic Materials*. Ed. by Arcady Zhukov. Vol. 231. Cham: Springer International Publishing, 2016, pp. 359–395. ISBN: 978-3-319-26104-1 978-3-319-26106-5. DOI: 10.1007/978-3-319-26106-5_9. URL: http://link.springer.com/10.1007/978-3-319-26106-5_9 (visited on 08/16/2023).

[123] Louis Néel. “Antiferromagnetism and Ferrimagnetism”. In: *Proceedings of the Physical Society. Section A* 65.11 (Nov. 1, 1952), pp. 869–885. ISSN: 0370-1298. DOI: 10.1088/0370-1298/65/11/301. URL: https://iopscience.iop.org/article/10.1088/0370-1298/65/11/301 (visited on 09/06/2023).

[124] Rui Zhang et al. “Rare-Earth-Free Noncollinear Metallic Ferrimagnets Mn4-xZxN with Compensation at Room Temperature”. In: *Acta Materialia* 234 (Aug. 2022), p. 118021. ISSN: 13596454. DOI: 10.1016/j.actamat.2022.118021. URL: https://linkinghub.elsevier.com/retrieve/pii/S1359645422004025 (visited on 09/06/2023).

[125] Se Kwon Kim et al. “Ferrimagnetic Spintronics”. In: *Nature Materials* 21.1 (Jan. 2022), pp. 24–34. ISSN: 1476-1122, 1476-4660. DOI: 10.1038/s41563-021-01139-4. URL: https://www.nature.com/articles/s41563-021-01139-4 (visited on 09/06/2023).

[126] I. Radu et al. “Transient Ferromagnetic-like State Mediating Ultrafast Reversal of Antiferromagnetically Coupled Spins”. In: *Nature* 472.7342 (2011), pp. 205–208. ISSN: 1476-4687. DOI: 10.1038/nature09901. URL: https://doi.org/10.1038/nature09901.

[127] I. Dzyaloshinsky. “A Thermodynamic Theory of “Weak” Ferromagnetism of Antiferromagnetics”. In: *Journal of Physics and Chemistry of Solids* 4.4 (Jan. 1958), pp. 241–255. ISSN: 00223697. DOI: 10.1016/0022-3697(58)90076-3. URL: https://linkinghub.elsevier.com/retrieve/pii/0022369758900763 (visited on 08/16/2023).

[128] Tôru Moriya. “New Mechanism of Anisotropic Superexchange Interaction”. In: *Physical Review Letters* 4.5 (Mar. 1, 1960), pp. 228–230. ISSN: 0031-9007. DOI: 10.1103/PhysRevLett.4.228. URL: https://link.aps.org/doi/10.1103/PhysRevLett.4.228 (visited on 08/16/2023).

[129] John M. D. Coey and Stuart S. P. Parkin, eds. *Handbook of Magnetism and Magnetic Materials*. Cham: Springer, 2021. ISBN: 978-3-030-63208-3. DOI: 10.1007/978-3-030-63210-6. URL: https://link.springer.com/10.1007/978-3-030-63210-6 (visited on 04/10/2023).

Appendix A

2D Fitting procedure

The 2D fitting utilized in Chapter 5 were performed using *Python*. The key libraries use for the analysis are shown in Code A.0.1. All data processing steps were handled using *NumPy* whereas all the fits were preformed using *SciPy Curve Fit* library. Because all raw data was stored in *HDF5* binary data format, we utilized library named *h5py* to open and import the raw compressed data into *Python*. Final fit results were stored using *pandas* library in *.xlsx* format.

Code A.0.1: Key libraries used for 2D fits

```
1 import numpy as np
2 import matplotlib.pyplot as plt
3 from scipy.optimize import curve_fit
4 import h5py as h5
5 import pandas as pd
```

Due to the large number of fit parameters, we developed a systematic step-by-step process to perform 2D fits. This procedure is as follows:

1. In the first step we utilized a centering algorithm to find a rough center for the scattering. This can also be done by manually guessing rough pixel location for the center of scattering.

2. The second step was to use azimuthally integrated intensity data to estimate the radius and with of scattering using single asymmetric Lorentzian defined as follows:

$$I = \left(B + \frac{A}{\frac{(q-q_0)^2}{\left(\frac{\Gamma}{1+e^{\alpha(q-q_0)}}\right)^2} + 1} \right)^2 \tag{A.1}$$

   where, B is the background, A is the amplitude, q_0 is the peak position, Γ is the half width half maximum and α is the asymmetry parameter. These rough fit parameters were used to generate a 2D version of the aforementioned function assuming. This 2D layer was than multiplied with the scattering image data in order to amplify the scattering features and suppress background/charge scattering.

3. The amplified data from previous step was fit with a isotropic 2D scattering ring (0^{th} harmonic) defined as follows:

$$I = \left(B + \frac{A}{\frac{(q-q_0)^2}{{\Gamma_0}^2} + 1} \right)^2 \tag{A.2}$$

   where, B is the background, A is the amplitude, q_0 is the peak position and Γ_0 is the half width half maximum. Python implementation of this step is shown in Code A.0.2.

Code A.0.2: 2D isotropic ring fit function written in python

```
def Lorentzian2D_fit(xyflat, *args):
        #Lorentzian 2D ring fit model
        #Args:
        #       xyflat (array of size N by 2): x and y meshgrid flattened
        #       args[0] (float): Background
        #       args[1] (float): q_0 or scattering ring position/radius
        #       args[2] (float): Gamma or half width half maximum of scattering
        #       args[3] (float): Amplitude of scattering
        #Returns:
         #       I (array N by 1): flattened intensity array
        u = xyflat[:,0]
        v = xyflat[:,1]
        q = np.sqrt(u**2+v**2)
        return (args[0]+args[3]/((q-args[1])**2/(args[2])**2+1))**2
```

4. Fix parameters for the isotropic ring and fit 2^{nd} and 4^{th} harmonics to fit the lobes or anisotropic scattering using the following equation:

$$I_{R+L}(q,\varphi) = B + I_R \left[\frac{1}{\left[\frac{(q-q_R)}{\Gamma_R}\right]^2+1}\right]^2 + \left[\frac{1}{\left[\frac{(q-q_L)}{\Gamma_L}\right]^2+1}\right]^2 \times \left[\left[\frac{I_L}{2}\left(\cos\left(2\left(\theta-\varphi_L\right)\right)+1\right)\right] + \left[\frac{I_{L_4}}{2}\left(\cos\left(4\left(\theta-\varphi_L\right)\right)+1\right)\right]\right]. \tag{A.3}$$

where, B is the background, I_R, I_L, I_{L_4} are the amplitudes of ring, 2^{nd} and 4^{th} harmonic of lobes, q_R and q_L are the peak position for ring and lobes, Γ_R and Γ_L are the half width half maximum and φ_L is the phase of lobes.

5. Perform a full fit using 0^{th}, 2^{nd} and 4^{th} harmonics refining all corresponding fit parameters.

6. Subtract the 0^{th}, 2^{nd} and 4^{th} harmonic fit results from the raw scattering image which would leave just the odd-order (1^{st} and 3^{rd}) harmonic signal. Fit this residual with $1^{st} + 3^{rd}$ harmonic with the following function:

$$I_O(q,\varphi) = B + \left[\frac{1}{\left[\frac{(q-q_O)}{\Gamma_O}\right]^2 + 1}\right]^2 \times \left[\left[\frac{I_O}{2}\left(\cos\left(\theta - \varphi_O\right)\right)\right] + \left[\frac{I_{O_3}}{2}\left(\cos\left(3\left(\theta - \varphi_O\right)\right)\right)\right]\right]. \tag{A.4}$$

Please note that missing $+1$ in the aforementioned equation compared to Eq. (A.3) in the azimuthal term. The omission of $+1$ is due to the fact that post subtraction of because, post subtraction of 0^{th}, 2^{nd} and 4^{th} harmonics from the raw scattering image, one half of the odd harmonic remaining dips below zero. As intensity can not be negative, this omission of $+1$ was purely for finding appropriate seed values for odd

harmonic fit parameters.

$$
\begin{aligned}
f_{odd}(q,\varphi) = B + I_R &\left[\frac{1}{\left[\frac{(q-q_R)}{\Gamma_R}\right]^2+1}\right]^2 \\
&+\left[\frac{1}{\left[\frac{(q-q_O)}{\Gamma_O}\right]^2+1}\right]^2 \times \left[\left[\frac{I_O}{2}\left(\cos\left(\theta-\varphi_O\right)+1\right)\right]+\left[\frac{I_{O_3}}{2}\left(\cos\left(3\left(\theta-\varphi_O\right)\right)+1\right)\right]\right] \\
&+\left[\frac{1}{\left[\frac{(q-q_L)}{\Gamma_L}\right]^2+1}\right]^2 \times \left[\left[\frac{I_L}{2}\left(\cos\left(2\left(\theta-\varphi_L\right)\right)+1\right)\right]+\left[\frac{I_{L_4}}{2}\left(\cos\left(4\left(\theta-\varphi_L\right)\right)+1\right)\right]\right].
\end{aligned}
\tag{A.5}
$$

7. Use results from the fits performed in previous steps to seed the full fit function shown in Eq. (A.5). The same seed parameters were used to fit all delay images in a *for* loop. Python implementation of the function is shown in Code A.0.3.

Code A.0.3: Full 2D fit function written in python

```
1 def Full_2D_Fit(xyflat, *args):
2         #Funtion used for 2D fitting of scattering images
3         #Args:
4         #        xyflat (np.array): A numpy array with flattened qx and qy
          ↪  values.
5         #        *args (np.array): A numpy array containing initial guess
          ↪  for all 13 fit parameters.
6         #Returns:
7         #        2D_fit (2D np.array): Returns a full 2D fit generated for
          ↪  the given *args.
8         u = xyflat[:,0]
```

```
        v = xyflat[:,1]
        theta = np.arctan2(u,v)
        q = np.sqrt(u**2+v**2)
        ring = args[0]+np.abs(args[3])/((q-args[1])**2/(args[2])**2+1)**2
        first_lobe = 1/((q-args[4])**2/(args[5])**2+1)**2*
        ↪  (np.abs(args[6])/2*(np.cos(theta-args[8])+1))
        third_lobe = 1/((q-args[4])**2/(args[5])**2+1)**2*
        ↪  (np.abs(args[7])/2*(np.cos(3*theta-3*args[8])+1))
        second_lobe = 1/((q-args[9])**2/(args[10])**2+1)**2*
        ↪  (np.abs(args[11])/2*(np.cos(2*theta-2*args[13])+1))
        fourth_lobe = 1/((q-args[9])**2/(args[10])**2+1)**2*
        ↪  (np.abs(args[12])/2*(np.cos(4*theta-4*args[13])+1))
        return ring + first_lobe + third_lobe + second_lobe + fourth_lobe
```

Appendix B

Time constant fitting procedure

Time constant fits presented in Chapter 5 were also performed using *Python*. The key libraries used for the fitting were very similar to 2D fitting which was discussed in Appendix A with an addition of *lmfit* library in order to access multiple minimization algorithms.

Following fitting procedure was used to perform time constant fits:

1. 2D fit results stored in *.xlsx* format were imported into python using *Pandas*.

2. Create the fit model of double exponential without the Gaussian convolution (see Code B.0.1) using *Model* class in *lmfit* library.

3. Perform a single time constant fit on one fluence to get an estimate of initial guess for fit parameters that will be used for time constant fits of rest of the fluences.

4. Perform time constant fits for all fluences with fixed of 0 or 1 for fit parameter C. Value of 1 was used to fit all amplitudes whereas a value of 0 was used to fit peak position and width.

5. Perform the fits again but now with C as a fit parameter. This additional step was added for aiding the convergence of fits.

6. Create a new fit model with addition of Gaussian convolution of width 45 fs. Perform the fits again but now with the new fit model and use the fit parameters from previous steps as initial guess.

Code B.0.1: Double exponential without Gaussian convolution used as first step for time constant fits.

```
def jumpdecay(x, A, B, C, t0, tm, tr):
        #Decay function with no second recovery
        return (C + np.heaviside(x-t0, 1) * \
        (A * np.exp(-(x - t0) / tm) -
        B * np.exp(-(x - t0) / tr) + (B-A)))
```

Code B.0.2: Double exponential with Gaussian convolution used for final time constant fits.

```
def vec_gaussian_convolution(x, y, sigma):
        """
        Convolves y with a gaussian on interval t
        Vectorized so at least 5 times faster
        """
        #conv = np.zeros(x.shape)
        x = np.reshape(x, (-1, 1))
        g = np.exp(-(x - x.T)**2/(2*sigma**2))
        gnorm = np.sum(g, axis=0)
        return g.dot(y) / gnorm

def convolved_no_tr2(x, A, B, C, t0, tm, tr, sigma):
```

```
13          """
14          decay function (no tr2) convolved with Gaussian
15          """
16          y = jumpdecay(x, A, B, C, t0, tm, tr)
17          result = vec_gaussian_convolution(x, y, sigma)
18          return result
```